University of Alberta

Magnetization-Prepared Gradient Echo Pulse Sequences at 4.7 Tesla

by

Anthony G. Tessier 

A thesis submitted to the Faculty of Graduate Studies and Research
in partial fulfillment of the requirements for the degree of

Master of Science

Department of Biomedical Engineering,
Department of Electrical and Computer Engineering

Edmonton, Alberta
Fall 2006

Your file Votre référence
ISBN: 978-0-494-22385-7
Our file Notre référence
ISBN: 978-0-494-22385-7

Abstract

Clinical and research medicine routinely uses magnetic resonance imaging pulse sequences with magnetization preparation. The design and evaluation of magnetization-prepared rapid gradient echo and modified driven equilibrium Fourier transform pulse sequences for brain imaging and angiography at 4.7 Tesla is explored in this thesis. Methods such as local receive-only coils, pulse sequence optimization, and adiabatic pulses are investigated for reduction of high field destructive interference effects. Various magnetization-prepared pulse sequences for structural imaging are designed for the best possible combination of signal, contrast, and uniformity. Rapid gradient echo sequences with and without magnetization preparation are optimized for maximum blood-to-background contrast and signal uniformity, and shown to be feasible for high field magnetic resonance angiography techniques. Magnetization-prepared imaging at 4.7 Tesla can be successfully utilized despite the increased radiofrequency nonuniformity and power deposition compared to lower field strengths.

Table of Contents

List of Tables

List of Figures

List of Abbreviations and Symbols

A = current in Amperes

A_{peak} = peak Amperes

A_{RMS} = root-mean-square Amperes

b = spatial and temporal field contribution due to spin-spin interactions

$\mathbf{B_0}$ = uniform static magnetic field strength

$\mathbf{B_1}$ = RF excitation pulse circularly polarized in the transverse plane

$\mathbf{B_{eff}}$ = effective magnetic field in the rotating frame due to B_0 and B_1

BIR-4 = B_1-Insensitive Rotation with 4 segments

$\mathbf{B_T}$ = transverse magnetization

BW_{rf} = bandwidth of an RF pulse

BW_{sam} = sampling bandwidth

CNR = contrast-to-noise ratio

CSF = cerebrospinal fluid

DEFT = driven equilibrium Fourier Transform

E = energy in Joules

$E_{|\alpha>}$ = parallel orientation (spin = ½) energy

$E_{|\beta>}$ = anti-parallel orientation (spin = -½) energy

E_z = energy difference between anti-parallel and parallel populations in a B_0 field

EMF = electromotive force, the voltage developed in an RF coil by rotating M_{xy}

FID = free induction decay

FLASH = fast low angle shot, a spoiled gradient echo pulse sequence

FOV = field of view

FWHM = full width at half maximum

f = frequency in Hertz

G_r = the gradient strength along the r axis in mT/m or G/cm

ΔG = gradient increment

GM = gray matter

GRE = gradient recalled echo, meaning the same as gradient echo or field echo

^1H = atomic symbol for a proton (hydrogen atom)

h = Planck's constant = 6.63×10^{-34} J s

$\hbar = h/2\pi$

$\mathbf{I}$ = spin angular momentum operator

$\hat{\mathbf{i}}$ = unit vector along the x-axis

$\hat{\mathbf{j}}$ = unit vector along the y-axis

k = Boltzmann's constant = 1.38×10^{-23} J/K

k = spatial frequency in units of rad/m or cycles/m

$\hat{\mathbf{k}}$ = unit vector along the z-axis

k_x, k_y, k_z = spatial frequencies along three orthogonal directions

k_{max} = maximum spatial frequency

$\mathbf{M_o}$ = net equilibrium magnetization of an ensemble of spins

$\mathbf{M_{xy}}$ = net transverse magnetization of an ensemble of spins

$\mathbf{M_z}$ = net longitudinal magnetization of an ensemble of spins

$\mathbf{M_\rho}$ = net magnetization of an ensemble of spins in a rotating reference frame

MDEFT = modified driven equilibrium Fourier Transform

MDEFT-GRE = modified driven equilibrium Fourier Transform gradient echo imaging

MIP = maximum intensity projection

MP = magnetization preparation or magnetization-prepared

MP-RAGE = magnetization prepared rapid gradient echo imaging

MR = magnetic resonance

MRA = magnetic resonance angiography

MP-MRA = magnetization prepared magnetic resonance angiography

MRI = magnetic resonance imaging

MTF = modulation transfer function

N_- = the anti-parallel population in a B_o field

N_+ = the parallel population in a B_o field

N_{AV} = number of averages

N_F = number of frequency encoded points

N_P = number of phase encoded points

PRESS = point resolved spectroscopy

PSF = Point Spread Function

r = the distance along the axis from the magnet isocentre

RAGE = rapid gradient echo imaging

r_o = initial position

RF = radiofrequency

RO = readout (frequency encoding data acquisition)

S = spin angular momentum

S(t) = signal received by a nearby RF coil due to the precession of net M_{xy}

SNR = signal to noise ratio

T_1 = spin-lattice, or longitudinal, relaxation time

T_2 = spin-spin, or transverse, relaxation time

T = temperature in Kelvin

TOF = time of flight MR angiography

t = time in seconds

t_{acq} = acquisition time

TE = echo time

TEM = Transverse Electromagnetic

TORO = Transmit-Only Receive-Only

TR = repetition time

TTL = transistor-transistor logic

Δt = time between adjacent points during acquisition

V = potential difference (voltage) in Volts

v = velocity in metres/second

WM = white matter

Δx, Δy, Δz = voxel dimensions

Φ = change in precessional frequency due to static field inhomogeneities

Ω = change in precessional frequency due to spin-spin interactions

β = spatial field contribution due to static field inhomogeneities

ϕ = phase angle produced by an angular frequency maintained over time

γ = magnetogyric/gyromagnetic ratio; for hydrogen nuclei, $\gamma = 2.675 \times 10^8$ rad/(T s)

$\gamma = \gamma/2\pi$

λ = wavelength in metres

μ = nuclear magnetic moment

ν_o = the frequency of precession of a spin in Hertz

θ = flip angle of an RF pulse

ρ = spin density

τ = time constant

ω_o = the frequency of precession of a spin in radians per second

ω_1 = angular frequency of rf pulse B_1

ω_{eff} = angular frequency of magnetization around the cone of precession defined by $\mathbf{B_{eff}}$

1 Introduction

In this work, magnetization-prepared (MP) imaging and angiography pulse sequences are implemented, tested, and evaluated using a 4.7 Tesla magnetic resonance imaging (MRI) scanner. MP gradient echo pulse sequences for morphological (structural) imaging of the human brain with optimum uniformity and white matter (WM) to grey matter (GM) contrast are designed and compared. Gradient echo pulse sequences with and without magnetization preparation are also explored for angiography. Image intensity variations due to high field destructive radiofrequency (RF) interference effects are compensated for using pulse sequence design methods in conjunction with a local receive-only phased array coil.

1.1 Introduction

Improvement of the visualization of blood vessels and brain structures is an area of active research in the field of MRI. Higher resolution imaging should afford more accurate diagnoses, and could provide further insight into the causes of diseases. In this work, pulses sequences are explored that have possible applications from basal nuclei movement disorders such as Parkinson's disease to blood vessel diseases such as atherosclerosis.

Research into the reduction of high field destructive RF interference effects was conducted. This is of utmost importance when working at high field, because image inhomogeneities caused by these effects can complicate analysis. Besides pulse sequence techniques, local receive head and neck coils were constructed to reduce these effects; they improve SNR in local regions of interest, and compensate for spatial signal variance to an extent.

A primary goal of this work was to acquire high quality images and angiography of the human brain using magnetization-prepared (MP) gradient echo pulse sequences on a 4.7 T magnet. The advantages of the 4.7 T magnetic field strength were exploited, such as higher inherent SNR and longer T_1 times. Some "disadvantages" of 4.7 T were also examined, such as the variance of signal across the brain and power deposition.

One of the primary objectives of this project was to perform high resolution angiography at the high field strength of 4.7 T. Ideally, the images should have high blood vessel visibility. In addition, background tissue signal should be suppressed to provide better blood contrast. The blood and background signals should be close to the same level across the brain. A technique using no magnetization preparation was developed and compared to standard MP angiography.

Another primary objective was high resolution imaging: to acquire the best images possible at 4.7 T, with the chosen pulse sequences. High tissue SNR is desired, as well as good white matter to grey matter signal difference (contrast). With 4.7 T imaging, it is difficult to maintain the signal intensity of individual tissues at a constant level across the brain. This, in turn, means that the contrast will also be spatially variant. Pulse sequences using magnetization preparation were tailored to provide maximum insensitivity to RF interference effects.

1.2 The Physics of Magnetic Resonance - Quantum Mechanical Basis

1.2.1 Intrinsic Magnetic Moments in Matter

Atoms with an odd number of neutrons and/or an odd number of protons are capable of experiencing the phenomenon known as magnetic resonance (MR). Spin angular momentum, also known simply as "spin", is a quantum mechanical vector quantity expressed as:

$$\mathbf{S} = \mathbf{I}\hbar \qquad (1.1)$$

where **I** is termed the quantum mechanical spin operator, and $\hbar = h/2\pi$, where h is Planck's constant. A magnetic dipole moment is related to **S** as follows[1]:

$$\mu = \gamma\mathbf{S} = \gamma\mathbf{I}\hbar \qquad (1.2)$$

where γ is a constant called the magnetogyric ratio, and is different for each nuclear species. The term "spin" is also used historically to describe any elementary particles or nuclei with $\mu > 0$.

Nuclei with higher γ have a stronger magnetic moment. The species with the highest magnetogyric ratio is hydrogen in the form of a single proton (^1H). It has $\gamma = 2.675 \times 10^8$ rad/(T s). It is also present in great abundance in the human body, for example in the form of water (H_2O). For these reasons, ^1H is the most sensitive species to MR.

Only nuclei that have nonzero net magnetic moments can be detected by MR techniques. The nuclei of hydrogen atoms are one example. Magnetic moments in matter arise from the circulating currents of the nucleons, and these currents are internal to the nuclei. In the case where the internal circulating currents cancel, no net magnetic moment results, $\mu = 0$, and MR is not possible.

The values of **I** are important in describing the quantum behaviour of spins and their relationship with energy. The z component of **I**, I_z, can take on a total of (2s+1) values, where s is called the spin quantum number. Each possible value of I_z is characterized by the magnetic quantum number, m:

$$m \in [-s, -s+1, \ldots, s] \qquad (1.3)$$

For the ^1H nucleus comprising a single proton, the spin quantum number $s = ½$, and so the possible values of I_z are described by $m = \pm ½$.

1.2.2 The Effect of Uniform, Static Magnetic Fields on Magnetic Moments of ^1H

Consider a system of ^1H in a resting state. Each of the individual magnetic moments is oriented randomly, and as such there is no resultant magnetization. When a static, uniform magnetic field, $\mathbf{B_0}$, is applied, the individual magnetic moments will align according to an anti-parallel/parallel ratio[2] described by classical Boltzmann statistics:

$$N_-/N_+ = e^{-\frac{E_Z}{kT}} \qquad (1.4)$$

where N_- is the anti-parallel population, N_+ is the parallel population, E_z is the population energy difference, k is Boltzmann's constant, and T is the temperature in K. The parallel state has lower energy, and as such is the dominant population. Thus, the net magnetization is aligned parallel to the uniform magnetic field $\mathbf{B_o}$, and this is usually specified as the Cartesian z direction.

Calculation of the population ratio as given by equation *(1.4)* would give a result that is close to unity. That is, the number of spins aligned parallel to the field is not significantly greater than the number aligned anti-parallel.

Physically, spins are actually aligned at an angle to the static magnetic field, yet their individual magnetic moments, μ, sum up to give a net magnetization, $\mathbf{M_o}$, aligned parallel or anti-parallel to $\mathbf{B_o}$, with a net transverse component of zero. The magnitude of the net magnetization M_o in a static magnetic field $\mathbf{B_o}$ has been determined as follows:

$$M_o = \rho\gamma^2\hbar^2 I(I+1)B_o/3kT \qquad (1.5)$$

where ρ is the number of spins per unit volume, also known as the spin density. The net magnetization is substantial enough to be measured, due to the large magnetic fields used, and the high γ and large quantity of ^1H in living things. Also evident from this equation is that sensitivity is inversely proportional to temperature. This is because thermal motion acts in opposition to the alignment of spins parallel to the static field.

1.2.3 Energy of ^{1}H in a Uniform, Static Magnetic Field

The interaction energy of a magnetic moment in a magnetic field **B** is given by:

$$E = -\mu \cdot \mathbf{B} = -\mu_z B = -\gamma I_z \hbar B \qquad (1.6)$$

Species with s = ½, such as ^{1}H, are quantized into two populations corresponding to the parallel and the anti-parallel orientations (called the $|\alpha\rangle$ and $|\beta\rangle$ states, respectively) when exposed to a static magnetic field[3], $\mathbf{B_o}$. Each population has its own discrete energy level. Two energy levels are possible for the ^{1}H nucleus:

$$\text{Anti-parallel orientation } (m = -½): E_{|\beta\rangle} = \gamma \hbar B_o/2 \qquad (1.7)$$

$$\text{Parallel orientation } (m = ½): E_{|\alpha\rangle} = -\gamma \hbar B_o/2 \qquad (1.8)$$

Thus the energy level difference is:

$$E_z = E_{|\beta\rangle} - E_{|\alpha\rangle} = \gamma \hbar B_o \qquad (1.9)$$

1.2.4 The Larmor Equation

The spin angular momentum of individual nuclei causes them to precess about the static magnetic field. The precession occurs because the static field $\mathbf{B_o}$ exerts a torque on each obliquely angled magnetic moment:

$$\text{Torque} = \mu \times \mathbf{B_o} \qquad (1.10)$$

Consider the quantization of ^1H into two discrete energy states. If a proton in the lower energy state absorbs a photon having the same energy as the energy difference between the two states, a transition between states occurs. A well-known equation describes the relation between the energy of a photon and its frequency:

$$E = h\nu_o \qquad (1.11)$$

where Planck's constant is a scaling factor for frequency, ν_o, in Hz, and energy, E, is in units of J. Equating the energy level difference in equation *(1.9)*, we see that:

$$E = \gamma h B_o/2\pi = h\nu_o \qquad (1.12)$$

$$\nu_o = \gamma B_o/2\pi \qquad (1.13)$$

which leads to the Larmor equation[4]:

$$\omega_o = \gamma B_o \qquad (1.14)$$

where ω_o is the frequency of precession of the spin about B_o in radians per second, also known as the Larmor frequency.

1.3 The Physics of Magnetic Resonance - Classical Model

1.3.1 The Effect of a Static Magnetic Field upon Transverse Magnetization

Consider a collection of spins with resultant $\mathbf{M} = \Sigma\mu$. With this summation of individual magnetic moments over a volume, a classical vector model can reasonably represent the quantum mechanical behavior of the spins.

Suppose the net equilibrium magnetization $\mathbf{M_0}$ is altered in some manner such that transverse components, $\mathbf{M_{xy}}$, are brought about. As in the case of a single magnetic moment, the static field $\mathbf{B_0}$ exerts a torque on the net $\mathbf{M_{xy}}$, and this is equal to the rate of change of angular momentum:

$$\frac{d}{dt}\mathbf{I}\hbar = \mathbf{M_{xy}} \times \mathbf{B_0} \qquad (1.15)$$

$$\frac{d}{dt}\mathbf{M_{xy}} = \gamma\mathbf{M_{xy}} \times \mathbf{B_0} = \gamma M_y B_0 \hat{\mathbf{i}} - \gamma M_x B_0 \hat{\mathbf{j}} \qquad (1.16)$$

This can be represented with complex notation, where the real component and imaginary component signify components along the x and y axis, respectively:

$$\frac{d}{dt} M_{xy} = \frac{d}{dt} M_x + i\frac{d}{dt} M_y = \gamma M_y B_0 - i\gamma M_x B_0 = -i\gamma M_{xy} B_0 \qquad (1.17)$$

The solution to this differential equation with initial condition $\mathbf{M_{xy}} = \mathbf{M_0} = M_0\hat{\mathbf{i}}$ at $t = 0$ is:

$$M_{xy}(t) = M_0 e^{-i\gamma B_0 t} = M_0(\cos(\omega_0 t) - i\sin(\omega_0 t)) \qquad (1.18)$$

which illustrates that the transverse magnetization will rotate in the negative sense about the z-axis with phase given by $\omega_o t$.

A rotating $\mathbf{M_{xy}}$ will induce an EMF, due to the change in magnetic flux over time[5], in a circumscribing receiver coil tuned to a resonant frequency of ω_o. Signal detected in this manner is referred to as a free induction decay (FID).

1.3.2 Spin Excitation by a Time-varying Radiofrequency Pulse

Spin excitation is the term for the process by which the net equilibrium magnetization $\mathbf{M_o}$ is altered such that net transverse magnetization components, $\mathbf{M_{xy}}$, are brought about. This occurs when a rotating, time varying magnetic field, $\mathbf{B_1}$, termed an excitation radiofrequency (RF) pulse, is applied in combination with and perpendicular to $\mathbf{B_o}$:

$$\mathbf{B} = \mathbf{B_o} + \mathbf{B_1}(t) = B_1 \cos\omega t\hat{\imath} + B_1 \sin\omega t\hat{\jmath} + B_o\hat{\mathbf{k}} \qquad (1.19)$$

such that the necessary torque is generated upon the net magnetization $\mathbf{M}$:

$$\frac{d}{dt}\mathbf{M} = \gamma \mathbf{M} \times \mathbf{B} \qquad (1.20)$$

This cross product leads to three differential equations $\frac{d}{dt}M_x(t)$, $\frac{d}{dt}M_y(t)$, and $\frac{d}{dt}M_z(t)$, describing rotational motion for each axis.

1.3.3 Magnetization Vector Analysis with a Rotating Reference Frame

Spin excitation is most easily understood through the use of a reference frame, denoted by the subscript ρ, which rotates about the z-axis at an angular frequency ω_o relative to the stationary laboratory frame. If $\mathbf{B_1}$ rotates at $\omega_1 = \omega_o$, then it will be static relative to the rotating frame. From geometric examination, one can perceive the components of a magnetization vector in the rotating frame ($M_{z\rho} = M_z$ because the frame rotates about z):

$$M_{x\rho} = M_x \cos\omega t + M_y \sin\omega t \qquad (1.21)$$

$$M_{y\rho} = -M_x \sin\omega t + M_y \cos\omega t \qquad (1.22)$$

Taking the time derivative of these equations, and inserting the differential equations for the laboratory frame $\frac{d}{dt}M_x(t)$, $\frac{d}{dt}M_y(t)$, and $\frac{d}{dt}M_z(t)$, gives the solution for the rotating frame magnetization components, $\frac{d}{dt}M_{x\rho}(t)$, $\frac{d}{dt}M_{y\rho}(t)$, and $\frac{d}{dt}M_{z\rho}(t)$, summarized by:

$$\frac{d}{dt}\mathbf{M}_\rho = \gamma \mathbf{M}_\rho \times \mathbf{B}_{eff} \qquad (1.23)$$

$$\mathbf{B}_{eff} = B_1 \hat{\mathbf{i}}_\rho + (B_o + \omega/\gamma)\hat{\mathbf{k}}_\rho \qquad (1.24)$$

From these equations one sees that magnetization precesses at a frequency γB_{eff} in the rotating frame on a conical surface, the centre of which is defined by a static effective field $\mathbf{B_{eff}}$.

If $\mathbf{B_1}$ rotates in a negative sense, that is, $\omega < 0$, and $|\omega| = \omega_o$, then from the equation above we see that $\mathbf{B_{eff}} = B_1\hat{\mathbf{i}}_\rho$, and the cone of precession becomes a circle parallel with the $y_\rho z_\rho$ plane.

In this case, $|\omega| = \omega_{eff} = \omega_1 = \omega_o$, thus we can calculate the "flip angle" θ, the angle between the equilibrium magnetization position and the final magnetization position, given the time t that the RF pulse is on:

$$\theta = \omega_1 t = \gamma B_1 t \qquad (1.25)$$

If the rotating $\mathbf{B_1}$ field is applied long enough to produce a 90° flip angle, it is termed a "$\pi/2$" or 90° RF pulse. A 90^o pulse is also called a saturation pulse. Saturation means the magnetization level is zero, and as such, no signal will be received if acquisition occurs immediately following the pulse. For acquisition of data, also called readout, pulse flip angles will usually be much smaller than 90^o. A "π" or "inversion" pulse produces a flip angle of 180°. In this state, the amplitude of the magnetization is identical to its equilibrium value, but its direction is inverted.

1.3.4 B_1 Inhomogeneity and Adiabatic Pulses

MRI using high static magnetic fields tends to suffer from $\mathbf{B_1}$ field spatial variance. It turns out that hard and soft pulses are quite sensitive to the inhomogeneity of $\mathbf{B_1}$ magnitude. A hard pulse, which would normally excite a sample uniformly, will impart a flip angle proportional to $\mathbf{B_1}$ strength. Thus, $\mathbf{B_1}$ inhomogeneity causes flip angle variations. The same effect occurs for soft pulses such as the sinc pulse. This problem is compounded with the fact that soft pulse profiles already have an inherently uneven excitation profile. One solution to this problem is to use a specialized RF excitation pulse, called an adiabatic pulse. All forms of adiabatic pulses are highly invariant with respect to $\mathbf{B_1}$ homogeneity.

In the rotating frame, a magnetization vector will precess around the effective $\mathbf{B_1}$ field, which is given by:

$$\mathbf{B_{eff}} = B_1\hat{\mathbf{i}}_\rho + \Delta\omega\,\hat{\mathbf{k}}_\rho \qquad (1.26)$$

for a pulse with frequency different than the Larmor frequency by an amount $\Delta\omega$. For most simple pulses, a constant frequency offset $\Delta\omega = B_o + \omega/\gamma$ is selected. Adiabatic pulses, however, make use of a varying $\Delta\omega$ to change $\mathbf{B_{eff}}$ over time and thus manipulate the magnetization $\mathbf{M}_\rho$. A fundamental condition of adiabaticity[6] is that the rate of change of $\mathbf{B_{eff}}$ is slow enough such that the magnetization $\mathbf{M}_\rho$ is able to follow it:

$$\left|\dot{\theta}\right| = |\gamma B_{eff}| \qquad (1.27)$$

where $\left|\dot{\theta}\right|$ is the absolute value of the rate of change over time of the flip angle. If this condition is satisfied during the pulse, then the $\mathbf{B_{eff}}$ field is rotated slowly, slow enough that $\mathbf{M}_\rho$ follows suit. In this manner, an adiabatic pulse is able to rotate the magnetization of a group of spins to various arbitrary flip angles, depending on the properties of the particular pulse involved.

Many different forms of adiabatic pulses have been discovered[7]. Hyperbolic secant adiabatic pulses are especially useful for inversion, with amplitude and frequency modulation as follows:

$$B_1(t) = B_1^0\,\mathrm{sech}(\beta t) \qquad (1.28)$$

$$\Delta\omega(t) = -\mu\beta\tanh(\beta t) \qquad (1.29)$$

Another type of adiabatic pulse that was considered for use was the Frequency Offset Corrected Inversion (FOCI) pulse[8]. Because these tend to have a greater deviation from their target flip angle than other forms of adiabatic pulses[9], FOCI pulses were not used. BIR-4[10] adiabatic pulses were chosen instead. They provide B_1-insensitivity combined with arbitrary flip angles[11]. They are not, however, capable of slice selection, and the power requirement is quite large. In addition, specialized phase cycling is required to remove unwanted transverse magnetization if the pulses are to be used for applications in which the transverse magnetization is important. In this work, the transverse magnetization following the BIR-4 pulses was unneeded, and thus, spoiled by gradient pulses.

1.3.5 Quadrature Detection of the MR Signal

With initial condition $\mathbf{M_{xy}} = \mathbf{M_o} = M_o\hat{\mathbf{i}}$, that is, with the excited magnetization initially pointing along the stationary laboratory frame x axis, a spin will precess in the negative sense about the z axis at a constant frequency ω_o. Given this knowledge, a detector which only sees the signal along the x or y axis will produce either a cosine or sine wave output:

$$M_x(t) = M_o\cos(\omega_o t) \qquad (1.30)$$

$$M_y(t) = -M_o\sin(\omega_o t) \qquad (1.31)$$

However, it is apparent from these equations that receiving signal along only one axis does not provide sufficient information about the angle of the transverse magnetization to determine its exact location in the xy plane. The solution is to acquire both orthogonal magnetization components, which will become the real and imaginary component inputs into a Fourier Transform during image reconstruction. This is called quadrature detection. Note that the Larmor frequency ω_o is removed during the data acquisition, and thus the recorded phase is relative to one of the axes of the rotating frame, often y_ρ.

1.3.6 Spin Relaxation

The net magnetization vector has two components that can be considered separately: longitudinal, $\mathbf{M_z}$, and transverse, $\mathbf{M_{xy}}$, which over time relax to their thermal equilibrium state. Each component recovers at its own rate, subsequent to RF excitation of a spin. As $\mathbf{M_{xy}}$ decays to zero, the longitudinal component $\mathbf{M_z}$ will recover to a magnitude equal to the equilibrium magnetization $\mathbf{M_0}$, and a direction aligned parallel to $\mathbf{B_0}$. For example, following a 90° pulse, $\mathbf{M_z} = 0$ and $\mathbf{M_{xy}} = \mathbf{M_0}$. Another example is the effect of a 180° pulse: $\mathbf{M_z} = -\mathbf{M_0}$ and $\mathbf{M_{xy}} = 0$. After full relaxation, $\mathbf{M_z} = \mathbf{M_0}$ and $\mathbf{M_{xy}} = 0$ in both cases. A first order approximation describing longitudinal relaxation is[12]:

$$\frac{d}{dt}M_z(t) = k(M_o - M_z(t)) = -\frac{(M_o - M_z(t))}{T_1} \qquad (1.32)$$

where $T_1 = -1/k$ is termed the spin-lattice, or longitudinal, relaxation time. Usage of the term spin-lattice is attributed to the fact that this relaxation occurs due to quantum mechanical actions between the lattice of molecules and their enveloped spins. The solution of the differential equation yields, for the initial condition $M_z(0) = 0$ (90° pulse):

$$M_z(t) = M_o(1 - e^{-\frac{t}{T_1}}) \qquad (1.33)$$

and for the initial condition $M_z(0) = -M_o$ (180° pulse):

$$M_z(t) = M_o(1 - 2e^{-\frac{t}{T_1}}) \qquad (1.34)$$

Transverse magnetization does not rotate around the $\mathbf{B_0}$ axis without ever decreasing in magnitude. This is because of the proximity of nearby spins acting in tandem with $\mathbf{B_0}$ to perturb the field around individual magnetic moments. The effect of the combination of $\mathbf{B_0}$ and the fields of nearby spins leads to temporal and spatial variation in the precessional frequencies of spins. This leads to an irreversible dephasing over time, called transverse relaxation. A first order approximation describing transverse relaxation is:

$$\frac{d}{dt}M_{xy}(t) = k'[0 - M_{xy}(t)] = -\frac{M_{xy}(t)}{T_2} \qquad (1.35)$$

where $T_2 = -1/k$ is termed the spin-spin, or transverse, relaxation time. Spatial variations due to a non-ideal (nonuniform) $\mathbf{B_0}$ also contribute to the dephasing, and are described by T_2'. The combination of both types of dephasing causes the overall dephasing, described by T_2^*, to occur at a faster rate:

$$\frac{1}{T_2^*} = \frac{1}{T_2} + \frac{1}{T_2'} \rightarrow R_2^* = \frac{1}{T_2^*}, R_2 = \frac{1}{T_2} \qquad (1.36)$$

The difference here is that the static field dephasing can be reversed, for example by a technique known as a spin-echo pulse sequence. The effect of the reversal is to rephase the magnetization, a process called echo formation, such that the decayed signal can be substantially recovered.

The T_1, T_2, and T_2^* recovery times for 4.7 T are listed in *Table 1.1*. They are dependent upon tissue characteristics as well the field strength $\mathbf{B_0}$. They give rise to contrast mechanisms by which different tissues can be distinguished.

Table 1.1 The recovery times T_1 and T_2^* may vary and depend upon the tissue type as well as the static magnetic field strength B_o. T_1 values tend to increase with B_o, while T_2^* values decrease.

4.7 T Values	T_1 (ms)	T_2^* (ms)
Grey Matter	1500	25
White Matter	1050	25
Cerebrospinal Fluid	4600	25
Blood	1900	

1.4 Magnetic Resonance Imaging (MRI)

1.4.1 Gradients

All the spins in a static field $\mathbf{B_0}$ in the absence of any other applied fields resonate at the frequency ω_0. In order to encode spatial information in the MR signal, static linear magnetic field gradients, simply known as gradients, may be applied[13]. Current-carrying wires wrapped around the magnet bore produce the gradients. The effect of the gradients is to vary the resonant frequency linearly as a function of distance from the centre of the magnet (termed the "isocentre"). The X, Y, and Z gradients all linearly increase or decrease $\mathbf{B_0}$ strength depending on the distance from the isocentre of the magnet, with the gradient direction being along the X, Y, and Z axes, respectively. Under the effect of a gradient:

$$\omega = \gamma(B_o + G_r r) \qquad (1.37)$$

where G_r is the gradient strength along the r axis in mT/m or G/cm, and r is the distance along the axis from the magnet isocentre.

In practice, gradient coils have certain non-ideal characteristics. For example, at some position from the isocentre, the gradient-distance relationship may become non-linear. Maximum gradient strength, and the time to ramp the gradient up to this strength -- called the rise or ramp time -- is finite. The ratio of these values is termed the "slew rate":

$$\text{slew rate} = \text{max gradient strength} / \text{rise time} \qquad (1.38)$$

Table 1.2 The maximum possible gradient strength and ramp times for the University of Alberta's in-vivo MR centre. The 3.0 T slew rate can be improved by inserting additional gradient hardware into the volume coil, called a "gradient insert". Note that specification of the value of the ramp time in software does not actually produce the same ramp time as displayed by an oscilloscope measurement of the gradient amplifier hardware. This may be partially due to the fact that the eddy current compensation hardware alters the gradient ramping.

	Maximum Gradient (mT/m)	**Software-specified Ramp Time (μs)**	**Measured Ramp Time (μs)**
1.5 T	40	200	
3.0 T	20 (without insert)	500 (without insert)	~600
4.7 T	35	300	~350

Maximum gradient strength and ramp times for the magnets at the University of Alberta MR facility are listed in *Table 1.2*. The gradient duty cycle specifies the time that the gradients can be on at maximum power before gradient coil damage takes place. For the 4.7 T system at the University of Alberta MR facility, the maximum gradient current is 430 A_{peak}, with a recommended maximum 200 A_{RMS}, and it puts out 750 V, so:

$$\text{maximum 4.7 T gradient duty cycle} = 200\ A_{RMS} / 430\ A_{peak} = 46.5\% \qquad (1.39)$$

For a large margin of safety, a maximum of 25% has been used in practice. Also of considerable importance in some applications is the time it takes for a gradient to actually begin to rise, after a rise command has been issued. The rise and fall of gradient currents may induce currents, called eddy currents, in the magnet cryostat (nearby conducting metal). These eddy currents may be problematic to imaging, and as such, a method called active shielding is employed, which involves addition of an outer coil that acts in opposition to the inner gradient coil, removing magnetic interactions with the cryostat at the expense of weaker gradients.

1.4.2 Slice Selection

It is advantageous in certain situations to excite only the spins in a spatially thin slice of an object; this is called slice selection. The method by which this is done is to apply an RF pulse simultaneously with a slice selection gradient perpendicular to the slice of interest. The bandwidth of the RF pulse controls the excited slice thickness, and must be designed to match the frequency bandwidth of the resonant frequencies of only the spins in the slice. The $\mathbf{B_1}$ carrier frequency ω_1, usually equal to ω_o, controls the position of the slice that is excited, along the axis normal to the slice select gradient.

Amplitude modulation of the envelope of the $\mathbf{B_1}$ pulse results in slice profiles that can be predicted using the Fourier Transform. Phase modulation can provide more complex profiles. A sinc excitation pulse in the time domain ideally results in a rectangular box slice profile in the frequency domain; a rectangular RF pulse results in a sinc-shaped slice profile. In reality, the sinc is truncated, resulting in an imperfect rectangular box. For amplitude-modulated pulses, the bandwidth of the RF pulse BW_{rf} is inversely related to the pulse width:

$$BW_{rf} \propto 1/(\text{pulse width}) \qquad (1.40)$$

In the case that the $\mathbf{B_1}$ envelope is amplitude modulated, the resulting flip angle is the area of the time-varying $\mathbf{B_1}$ envelope:

$$\theta = \omega_1 t = \int \gamma B_1(t) dt \qquad (1.41)$$

If the goal of the slice selection gradient is to create transverse magnetization in the rotating frame $x_\rho y_\rho$ plane, then a rephasing lobe is also required. The slice select gradient introduces a phase accumulation in the net transverse magnetization, which must be rephased. The rephasing lobe should be opposite polarity to and half the area of the slice select gradient. An ideal 180° would generate no net $\mathbf{M_{xy}}$, and thus it does not require rephasing.

1.4.3 Spatial Encoding

Consider two spins located along an axis. One is at location +r, the other at –r, under the influence of a gradient along the axis, G_r. The spins have effective frequencies of $\omega = \gamma(B_o \pm G_r r)$. Spatial encoding can be performed by applying an RF pulse followed by a gradient pulse with simultaneous data acquisition. The measured EMF will consist of a combination of two (decaying) sinusoidal waves, with periods of $2\pi/\gamma(B_o \pm G_r r)$, which when Fourier Transformed will display peaks at the two effective frequencies of the spins. This process is called frequency encoding. The phase accumulation ϕ for one spin as a function of position r and acquisition time t is:

$$\phi(r, t) = \omega(r)t = \gamma G_r r t \qquad (1.42)$$

In the rotating frame, $\phi = 0°$ along $\hat{\mathbf{j}}_\rho$, and ω_o can be ignored. Given that the spin will have a transverse magnetization magnitude $M_{xy} > 0$ after the RF pulse, the detected signal along one axis is:

$$S(t) = M_{xy}\cos\phi \qquad (1.43)$$

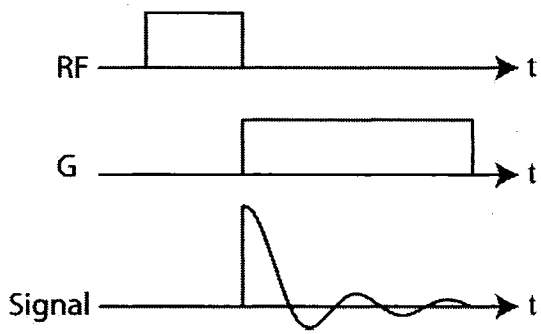

Figure 1.1 Frequency encoding by acquiring while simultaneously applying a gradient. The preceding RF pulse excites the spins, producing some magnetization in the transverse plane. The applied gradient causes a phase accumulation of the magnetization over time. In effect, the spin locations are spatially encoded as frequencies in the electromotive force (EMF) signal induced in the receiver coil. The EMF is not actually cosinusoidal in practice, but has a falloff over time, due to T_2^* decay.

Spatial encoding can alternately be performed by applying an RF pulse followed by a gradient pulse, finally followed by data acquisition. In this case, prior to the application of the gradient G_r, the net transverse magnetization vector for each of the two spins will be stationary along the y_ρ axis. During the gradient, the net transverse magnetization of the spin at the +r position will rotate in the negative sense relative to the rotating frame frequency ω_o, and vice versa for the net magnetization of the spin at the –r position. After the gradient is turned off at some time τ, the two spins will have evolved a phase proportional to the time that the gradient was on. This process is called phase encoding, and the final phase for the two spins at –r and +r is given by:

$$\phi(\pm r) = \omega(r)\tau = \mp \gamma G_r r\tau \qquad (1.44)$$

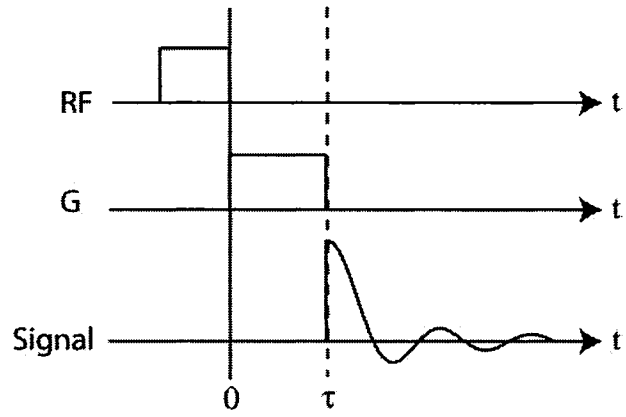

Figure 1.2 The phase encoding process is performed by the application of a gradient followed by acquisition of signal. The applied RF pulse excites the spins such that some transeverse magnetization is created. The gradient causes a phase accumulation to occur, proportional to the time that it is on, τ. The subsequent signal that is acquired will have some phase as set by the preceding gradient pulse.

1.4.4 Fourier Transform MRI

The MR signal consists of a measurement of the EMF generated by the net transverse magnetization of the excited nuclei in an object. From the signal, an MRI image is generated which comprises a map of the magnitude of the net $\mathbf{M}_{xy}$ at various points insides an object. Two-dimensional (2-D) imaging combines frequency and phase encoding to encode spatial information along two orthogonal directions by creating a spatial dependency of the frequency of the transverse magnetization in one direction, and the phase in the other.

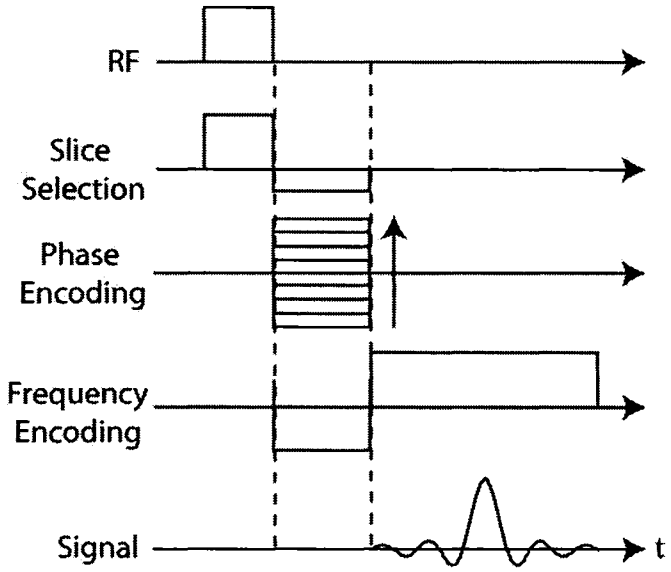

Figure 1.3 Simplified timing diagram for 2-D Fourier transform MRI. An RF excitation pulse is applied to the sample simultaneously with a slice selection gradient. Following this, phase encoding takes place, followed by frequency encoding and acquisition of signal. The whole pulse sequence is repeated for multiple phase encoding steps, and each time, the phase encoding gradient is incremented. If the frequency encoding gradient has a dephasing gradient pulse of half its area prior to it, then an echo signal is generated as shown. Note that the slice selection gradient refocusing pulse can take place simultaneously with phase encoding and the frequency encoding dephasing pulse.

During the pulse sequence, first the phase encoding gradient is switched on, and the magnetization is allowed to accumulate a specific phase before the gradient is switched off. Subsequent to this, the frequency-encoding gradient is applied simultaneously with signal acquisition. In this manner, the phase of the signal acquired during frequency encoding will depend upon a specific spatial position along the orthogonal (phase encoding) axis. This process is repeated for multiple positions along the phase encoding direction, with the phase accumulation caused by the phase encoding gradient modified to give a unique phase for each position along that axis. For example, if there is an object contained within a single position along the phase encoding axis, the frequency content along the axis will consist of a single component. This frequency component is the

frequency of variation in phase along the phase encoding direction, and it describes the location of the object along the axis. Once the net $\mathbf{M_{xy}}$ at each position has been spatially encoded, it can be reconstructed from the acquired signal with an inverse Fourier Transform. Components both real and imaginary, also known as absorptive and dispersive, respectively, are obtained, and these describe the actual phase of the net $\mathbf{M_{xy}}$ at each position. Usually the phase is discarded and only the magnitude, M_{xy}, is shown in the final image.

1.4.5 Signal Equation and k-Space

The location and density of the transverse magnetization at each position inside an object can be derived from the acquired EMF signal. We have considered a single precessing spin at some position r along an axis, under the influence of a gradient along this axis, G_r. Frequency encoding occurs, and the resulting phase accumulation and signal have been described ($\phi(r, t) = \gamma G_r rt$, $S(t) = M_{xy}\cos\phi$). Next, consider the frequency encoding case in which the coil receives signal from multiple spins collinear along an axis, while a gradient G_r is applied along this axis. The detected signal along the axis is:

$$S(t) = \sum_n M_{xy,n}\cos\phi_n \qquad (1.45)$$

where $M_{xy,n}$ is the magnitude of the net transverse magnetization for spin n.

Now imagine that there is a one-dimensional, uniform object consisting of a distribution of spins running from position $-r_{max}$ to $+r_{max}$ along an axis. Once again, a gradient is applied along this axis, G_r. The maximum phase accumulated from all the spins in this one-dimensional distribution is:

$$\phi_{max} = \omega t = \gamma G_r r_{max} t \qquad (1.46)$$

Performing integration across the distribution of spins, and using the simplification that the object is centred along the axis, we see the time domain signal along one axis is a sinc function:

$$S(t) = \int_{-r_{max}}^{r_{max}} \frac{dr}{2r_{max}} \cos(\gamma G_r r t) = sinc(\gamma G_r r_{max} t) \qquad (1.47)$$

This transformation from a rectangular distribution of spins to a sinc function is indicative of a Fourier Transform relationship.

A coil with quadrature detection capability receives signal S(t) from all the spins in a one-dimensional row, while a gradient is applied, and the result is (considering M_{xy} in the rotating reference frame so that ω_0 can be ignored):

$$S(t) = \int M_{xy}(r) e^{-i\gamma G_r r t} dr \qquad (1.48)$$

The inverse Fourier Transform yields M_{xy} as a function of r:

$$M_{xy}(r) = \gamma G_r \int S(t) e^{+i\gamma G_r r t} dt \qquad (1.49)$$

Given the phase for a point in space exposed to a rectangular-shaped gradient for a time t, $\phi = \omega(r)t = \gamma G r t$, consider a more general case with an arbitrarily-shaped gradient:

$$\phi = \int \omega(r) t = \gamma \int G \, dt \, r = kr \qquad (1.50)$$

Here, the symbol $k = \gamma \int G\ dt$ is used to indicate a spatial frequency with units of rad/m (or cycles/m if $\gamma = \gamma/2\pi$ is used). Thus we see that a $\gamma \times$ (gradient area), k, represents phase accumulation per distance from the gradient centre (r = 0).

Time Domain Signal (t) $\propto$ Spatial Frequency Domain (k-space) ($\gamma Gt = k$)

$\uparrow$

Fourier Transform

$\downarrow$

Frequency Domain ($\omega = \gamma Gr$) $\propto$ Actual Spatial Position (Object Space) (r)

Substitution of k for γGdt in the equation for $M_{xy}(r)$, we obtain ($dk = \gamma Gdt$):

$$M_{xy}(r) = \int S(t) e^{+ikr} dk \qquad (1.51)$$

Now consider a 2-D distribution of spins in a transverse plane, xy. Suppose that the spin distribution has been phase encoded using gradients along the y-axis, and frequency encoded using a gradient along the x-axis. The phase accumulation of the spin distribution at a location in 2-D space at time t is:

$$\phi(x,y,t) = \int \omega(x,y)t = \gamma \int G_x\ dt\, x + \gamma \int G_y\ dt\, y = k_x x + k_y y \qquad (1.52)$$

Considering M_{xy} in the rotating reference frame, we can determine the 2-D signal as:

$$S(t) = \iint M_{xy}(x,y) e^{-i(k_x x + k_y y)} dx dy \qquad (1.53)$$

The inverse Fourier Transform produces the 2-D image of an object[14]:

$$M_{xy}(x,y) = \iint S(t) e^{+i(k_x x + k_y y)} dk_x dk_y \qquad (1.54)$$

1.4.6 Encoding Sampling Constraints

The field of view (FOV) describes the spatial coverage of an image, and encompasses a frequency bandwidth of:

$$\Delta f_{max} = \gamma(B_o + Gr_{max}) - \gamma(B_o + Gr_{min}) = \gamma G(r_{max} - r_{min}) = \gamma G \text{ FOV} \qquad (1.55)$$

where $\gamma = \gamma/2\pi$ and the maximum expected frequency is $f_{max} = \gamma G$ FOV/2. Nyquist sampling rules apply to both the frequency and phase encoding directions, and restrict the sampling frequency for proper signal digitization such that the maximum phase shift between adjacent points is $\Delta\phi_{max} \leq \pi$. This means that the sampling bandwidth must be at least twice f_{max}, $BW_{sam} \geq 2f_{max}$. Thus for frequency encoding sampling:

$$BW_{sam} \geq \gamma G \text{ FOV} \qquad (1.56)$$

For N_F frequency encoding points of width Δx, the FOV in the x-direction is simply $FOV_x = N_F \Delta x$. Similarly, for N_P phase encoding points of width Δy, the FOV in the y-direction is $FOV_y = N_P \Delta y$. Thus, for frequency encoding sampling, with a constant gradient G, and time between points Δt, $\Delta\phi_{max} = 2\pi f_{max}\tau = 2\pi\gamma\Delta t\, G\, FOV/2 \leq \pi$:

$$\Delta t = 1/BW_{sam} \leq 1/(\gamma G \text{ FOV}) = 1/(\gamma G N_F \Delta x) \qquad (1.57)$$

For phase encoding sampling with constant time τ, and a change in gradient strength ΔG for each phase encoding line, $\Delta\phi_{max} = 2\pi f_{max}\tau = 2\pi\gamma\tau\Delta G\ FOV/2 \leq \pi$:

$$\Delta G \leq 1/(\gamma\tau FOV) = 1/(\gamma\tau N_P \Delta y) \qquad (1.58)$$

In practice, to maximize resolution the inequalities are replaced with equal signs. For an RF pulse, it was noted that the bandwidth BW_{rf} controls the slice thickness Δz that is excited. Thus the equation is similar:

$$BW_{rf} = \gamma G\ \Delta z \qquad (1.59)$$

The k-space step along the x and y directions are:

$$\Delta k_{frequency} = \gamma G \Delta t;\ \Delta k_{phase} = \gamma \Delta G \tau \qquad (1.60)$$

$$\Delta t = 1/(\gamma G\ FOV) \rightarrow 1/\Delta t = \gamma G\ FOV \rightarrow 2\pi = \gamma G \Delta t\ FOV \rightarrow \Delta k = 2\pi/FOV \qquad (1.61)$$

Given the case of symmetric sampling and $\Delta k = 2\pi/N_F\Delta x$, $k_{max} = N\Delta k/2$, so:

$$\text{k-Space range} = 2k_{max} = 2\pi/\Delta x \qquad (1.62)$$

where the last two equations can be derived from the phase encoding case as well.

1.4.7 k-Space Trajectories

k-Space is another name for the time domain EMF raw data signal acquired during the frequency encoding stage of MRI. The central, low frequency content of k-space is

responsible for the majority of the contrast in MRI images, while the higher frequencies control the blurring and edges of images.

Modulation of k-Space raw data often occurs, and this can be very undesirable. The Modulation Transfer Function (MTF) describes this modulation. The Fourier Transforms of the MTF, actual object k-Space data, and acquired k-Space raw data give the Point Spread Function (PSF), actual object spatial data, and final image, respectively.

$$\begin{array}{c} \text{k-space MTF} \times \text{Actual Object k-Space Data} = \text{Acquired k-Space raw data} \\ \uparrow \\ \text{Fourier Transform} \\ \downarrow \\ \text{PSF} * \text{Actual Object Spatial Data} = \text{Final Image} \end{array}$$

where * signifies convolution. An ideal MTF is equal to unity, which would give a delta function for the PSF. Cyclic modulation produces multiple PSF peaks, which in turn causes ghosting in the final image. Blur is caused by MTF falloff, which increases the PSF width. A measure of the blur is the full width at half maximum (FWHM) of the PSF.

The path which a pulse sequence follows through k-Space (the k-Space "playout") is determined by the timing and magnitude of the gradients. For a single frequency encoding, the data acquisition portion of which is also called "readout" and abbreviated RO, an initial dephasing lobe is often played out. The purpose of this is to allow sampling of data to occur at some negative spatial frequency k_x, which otherwise would be initially zero. As frequency encoding proceeds, k_x moves across negative k-Space, eventually crosses $k_x = 0$ at the echo time TE, the centre of the echo. The right half of the frequency-encoding gradient fills the right half of the k_x line of k-Space.

The standard gradient echo (also known as gradient recalled echo or field echo) imaging pulse sequence includes multiple frequency encoding steps[15], each of which occurs in

conjunction with and subsequent to a different phase encoding gradient. The phase encoding gradient areas, described by the k_y values, are incremented for each RO. The effect is that the phase encoding allows filling of "vertical" k-Space by changing k_y, while frequency encoding fills "horizontal" k-Space, by changing k_x.

The order that phase encoding gradients are played out is very important. Sequential acquisition, that is, phase encoding gradients implemented linearly, produces a sequential k_y trajectory which plays out from one end of "vertical" k-space to the other, all in one step or "shot". A multi-shot sequence could traverse k-Space similarly, from one end of k_y to the other, but skipping a fixed number of k_y steps for each individual shot. Each subsequent shot would start at a slightly different k_y offset, but still increase sequentially with the same Δk_y. In this manner, sequences can be broken up into shorter time segments, while still filling k-Space appropriately and nearly identically for each shot. "Centric" phase encode ordering comprises a trajectory which always begins at the centre of k-Space, and plays outward. The purpose of centric encoding is to take advantage of the low frequency content of k-Space to provide superior image contrast to sequential orderings.

1.5 Spoiled Fast Low Angle Shot (FLASH)

For both imaging and angiography, a spoiled gradient echo (GRE) sequence with a train of RF pulses can be utilized, sometimes called a spoiled FLASH sequence (fast low angle shot). FLASH will be used in later chapters in order to acquire echoes in combination with magnetization-prepared rapid gradient echo imaging (MP-RAGE).

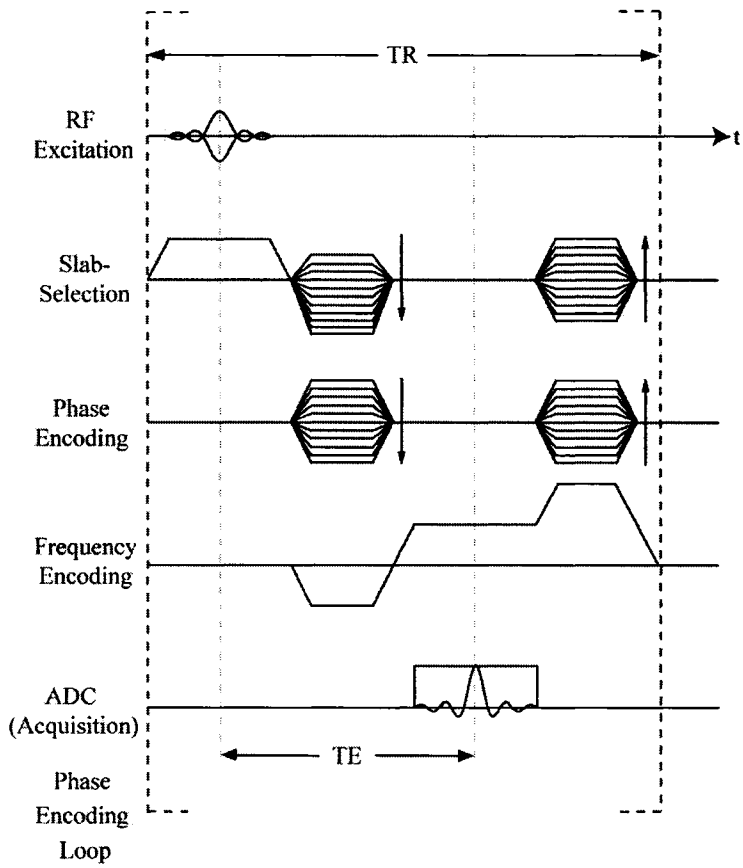

Figure 1.4 Spoiled FLASH is a 2D Fourier Transform MRI pulse sequence that uses low RF flip angles (approximately 20°) with phase and frequency encoding. The echo time TE is the time between the RF and the $k_x = 0$ point during readout. The repetition time TR is the total time for one repetition of the sequence, from the start of the RF pulse, to the end of gradient spoiling. Multiple phase encoding (PE) loops are run to acquire many lines of k-space. Acquisition of the echo is signified by the analog-to-digital converter (ADC) utilization. An additional spoiling gradient follows the end of frequency encoding. In practice, the sequence uses trapezoidal gradients with finite slew rates as shown.

Consider a train of RF excitation pulses α_n, where n varies from 1 to the total number of pulses, n. If complete spoiling occurs, it can be assumed that any remnant transverse magnetization after acquisition of each echo is equal to zero. After α_1, signal at TE is $M_{xy}(TE) = M_z(0)\exp(-TE/T_2^*)\sin\alpha$, and immediately before α_2, $M_z(TR^-) = M_o + (M_z(0)\cos\alpha - M_o)(\exp(-TR/T_1))$. The longitudinal magnetization before a pulse α_n will

be written $M_z(n^-)$. After sufficient pulses in the gradient echo sequence, the magnetization will eventually reach some steady state value, where $M_z(n^-) = M_z(n+1^-) = M_z(\text{steady state})$. At steady state:

$$M_z(n+1^-) = M_o + (M_z(n^-)\cos\alpha - M_o)\,(\exp(-TR/T_1)) \qquad (1.63)$$

$$M_{xy}(TE) = M_z(\text{steady state})\exp(-TE/T_2^*)\sin\alpha \qquad (1.64)$$

Then:

$$M_z(\text{steady state}) = M_o + (M_z(\text{steady state})\cos\alpha - M_o)\,(\exp(-TR/T_1)) \rightarrow$$

$$M_z(\text{steady state}) = M_o\left(\frac{1-\exp(-TR/T_1)}{1-\exp(-TR/T_1)\cos\alpha}\right) \rightarrow$$

$$M_{xy}(TE) = M_o\left(\frac{1-\exp(-TR/T_1)}{1-\exp(-TR/T_1)\cos\alpha}\right)(\sin\alpha)\exp(-TE/T_2^*) \qquad (1.65)$$

Calculating $dM_{xy}/d\alpha = 0$ gives the angle that provides maximum steady state signal, called the Ernst angle:

$$\alpha_{Ernst} = \cos^{-1}(\exp(-TR/T_1)) \qquad (1.66)$$

1.6 Driven Equilibrium Fourier Transform (DEFT)

The chemical environment of a spin has an impact on its resonant frequencies. Spectroscopy is an MR technique that takes advantage of this. It separates signals according to their frequencies, and is able to quantify the abundance of many different chemicals in the body. The driven equilibrium Fourier Transform[16] (DEFT) pulse sequence is one such method. It uses delays, τ, between three RF pulses to drive the magnetization into equilibrium faster than relaxation would alone. As such, it allows for an accelerated repetition of scans. This is advantageous, especially for species with long

T_1 times, because it means more averages can be performed and hence noise can be reduced.

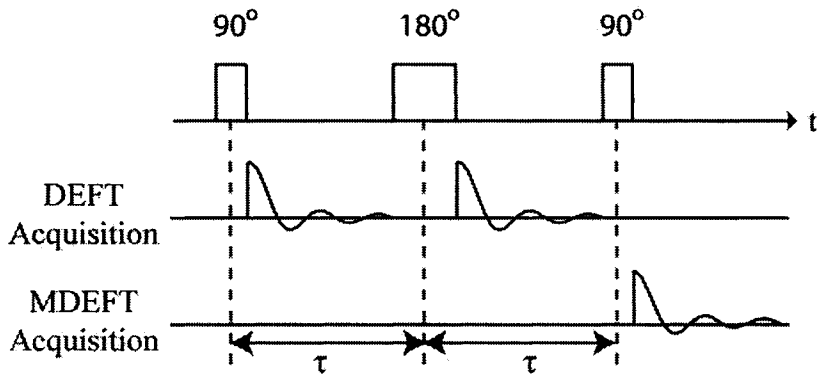

Figure 1.5 Pulse sequence timing diagram for DEFT and MDEFT. The basic sequence comprises a 90° pulse followed by a delay τ, followed by a 180° pulse, another delay τ, and a final 90° pulse.

Modified DEFT (MDEFT) is an alternate spectroscopy technique that has found renewed interest recently for imaging applications. It differs from DEFT in that the data acquisition occurs following the initial 90°-τ-180°-τ-90° sequence, rather than between the RF pulses. Historically this was used to suppress long T_1 species in proton NMR. For imaging purposes, it provides a mechanism by which the contrast and uniformity of images can be improved. MDEFT gradient echo imaging (MDEFT-GRE) will be used extensively later in this thesis.

1.7 Magnetic Resonance Angiography (MRA)

1.7.1 3-D Imaging

Due to the relation $BW_{rf} = \gamma G \Delta z$, if we desire short pulses (large BW_{rf}), 2-D imaging slice thickness is limited by the gradient strength, and the SNR may be insufficient for the

thinnest slices available. It is possible to image thin slices without gradient limitations by exciting a large slab and adding a second phase encoding step along the slab-select direction, with the width of the phase encoding spanning the BW_{rf}. This is called 3-D imaging and increases imaging time by the number of phase encoding steps across the slab, and so SNR increases by (number of slab phase encoding steps)$^{1/2}$. In addition to the finer vessel detail offered for angiography, another advantage of 3-D imaging is that the TE may be shorter because shorter pulse lengths can be used, and hence intra-voxel dispersion due to motion effects as well as T_2^* decay is decreased.

1.7.2 Time of Flight (TOF)

For angiography, high blood-background contrast is desirable. Typically, the imaging slab is oriented such that it is perpendicular to most blood vessels of interest, such that "fresh" blood with magnetization as yet untouched by RF pulses continues to flow into the slab at intervals governed by the subject's heart rate.

One method of performing MR angiography is to continuously image using a gradient recalled echo (GRE) pulse sequence until the background is at a low steady state signal level. As fresh blood continues to enter the imaging slab, the blood signal should be higher. The parameters to achieve this must be carefully chosen in order to prevent blood from experiencing too many RF pulses as it travels through the slab, and dropping to a lower signal level than the steady-state background signal. Typical values are TR = 30ms, with an excitation flip angle of 25°. This technique is called Time of Flight (TOF) MR angiography. Choice of slice thickness is constrained by:

$$\Delta z = Nv\ TR \qquad (1.67)$$

where N is the number of RF pulses that blood experiences as it travels through the volume, v is the velocity of blood, and TR is the repetition time of the experiment (v TR = distance travelled by blood in one TR).

1.7.3 Gradient Moment Nulling

The velocity of spins is usually neglected if TE is short. Examining phase including velocity effects with $r = r_0 + vt$, r_0 being the initial position of a spin along the r-axis, and r being some distance from r_0, we see:

$$\phi(r) = \int \omega(r)t = \gamma \int G\ r\ dt = \gamma \int G\ (r_o + vt)\ dt = \gamma G(r_o t + vt^2/2) \qquad (1.68)$$

Suppose a gradient -G of length τ is immediately followed by an identical gradient with opposite polarity. Subsequently, $\phi = 0$ for stationary spins, but for moving spins with $r_0 = 0$:

$$\phi(v) = -\gamma G v t^2/2 \Big|_0^{\tau} + \gamma G v t^2/2 \Big|_{\tau}^{2\tau} = \gamma G v(-\tau^2 + 2\tau^2) = \gamma G v \tau^2 \qquad (1.69)$$

That is, moving spins accumulate additional velocity-dependent phase[17]. Different phase shifts caused by multiple moving spins, each with different velocities within a single voxel, incur signal loss. On the other hand, if there is no intra-voxel dephasing, but all of the spins within a voxel move at the same rate, a global phase shift occurs, and there is no SNR penalty if the final image consists of taking the absolute values of each complex pixel's real and imaginary components. Similarly, there is no SNR penalty if different phase shifts occur for different voxels, as long as no intra-voxel phase dispersion takes place. Pulsatile blood flow implies that velocity and hence phase shift changes over time.

This causes myriad phase shifts during phase encoding, often leading to a cyclic MTF, which in turn causes multiple peaks in the image PSF and hence ghosting artefacts.

Flow compensation can be performed by a method known as first order gradient moment nulling, whereby the effects of constant velocities are accounted for. Usually during imaging, only the phase dispersion produced by the zero'th moment, $\int G\ dt$, is nulled at the centre of the readout window, ie. at $k_x = 0$. With first order gradient moment nulling, the phase generated by the first moment, $\int G\ t\ dt$, is nulled using three consecutive gradient pulses of alternating polarity, often with all three pulses of the same strength, but the middle pulse lasting twice as long. Phase accumulation due the zero'th and first moments after the third pulse will ideally be zero.

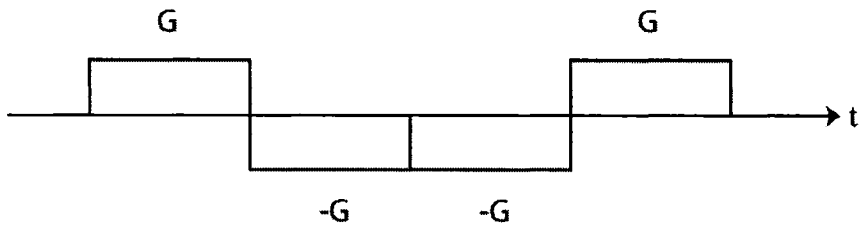

Figure 1.6 First order gradient moment nulling can be performed by three successive gradients of identical magnitude |G|. After playout of these gradients, both the zero'th and first order moments will be nulled. If this is used as part of the frequency encoding gradient, the final pulse would be extended for the rest of the encoding.

1.7.4 Inversion Recovery

T_1 differences of tissues can be exploited to provide a mechanism of contrast. Consider the effect of a 180° pulse on two tissues, one with a long T_1, the other short. Immediately subsequent to the pulse, the net magnetization for all spins should be equal to $M_z = -M_o$. The magnetization of both T_1 species will both recover at different rates, such that the M_z of both will pass through zero at different times. If an excitation pulse is applied when the

M_z of one of the tissues is equal to zero, that tissue will generate zero M_{xy}, and thus will appear darker in the final image than the other tissue.

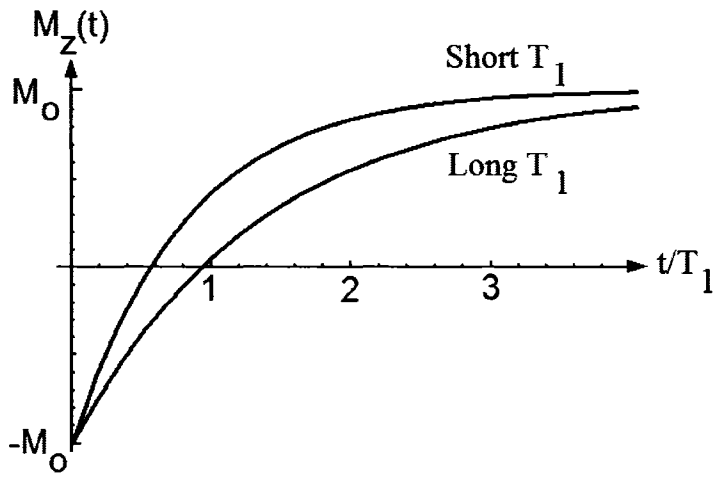

Figure 1.7 Potential for image contrast arises when two species have recovery times that are different. Shown here is the difference in longitudinal magnetization recovery for a shorter versus longer T_1 value.

This is precisely the process that is exploited with IR-MRA techniques. Acquisition occurs when the background signal is nulled. Fresh blood flows into the imaging slab after the inversion pulse, such that the acquired blood signal will be much higher than the background.

1.7.5 Signal-to-Noise Ratio (SNR)

Since EMF is directly related to the change in magnetic flux, signal depends on ω_o. Signal also depends on the ability of the coil to translate the magnetic flux into EMF. This can be measured by reciprocity; that is, if the coil were transmitting, it should maximize generated transverse $\mathbf{B_T}$ for each Ampere input. As well, signal depends upon the spin density, the number of averages N_{AV}, and directly upon $\mathbf{B_o}$ by the amount of equilibrium magnetization ($\mathbf{M_o} \propto \mathbf{B_o}$).

In in-vivo MRI, white thermal noise due to the random motion of electrons and resistance of the body dominates, with the resistance of the electronics contributing. The amount of noise collected depends on the width of the anti-aliasing filter, which is proportional to the sampling bandwidth BW_{sam}. In general, the standard deviation of the noise is used, and so here the noise intensity is proportional to $BW_{sam}^{1/2}$. To a certain extent, noise averaging occurs during the Fourier Transform process, and thus the standard deviation of the noise of an image is decreased compared to the raw data, according to the number of points used. If the number of frequency encoding points is N_F, and the number of phase encoding points is N_P, then the noise is reduced by a factor of $1/(N_P N_F)^{1/2}$. Note also frequency encoding acquisition time $t_{acq} = N_F/BW_{sam}$, and the total measurement time = $N_P N_{AV} t_{acq}$.

When averaging, because the noise is not correlated between acquisitions, the standard deviation of noise does not increase linearly and is proportional to $N_{AV}^{1/2}$. The standard deviation of the noise is also a function of (temperature × resistance) $^{1/2}$. Ignoring temperature for the moment, due to the fact that the resistance of the body dominates the noise for in-vivo MRI, the resistance $\propto \omega_o^2$, and so the standard deviation of noise $\propto \omega_o$, thus the signal-to-noise ratio (SNR) is[18]:

$$\begin{aligned} SNR &\propto (\omega_o/\omega_o) M_o B_T \Delta x \Delta y \Delta z (N_P N_F N_{AV}/BW_{sam})^{1/2} \\ &= M_o B_T \Delta x \Delta y \Delta z (\text{experiment time})^{1/2} \end{aligned} \qquad (1.70)$$

1.8 Bibliography

[1] EM Haacke, RW Brown, MR Thompson, R Venkatesan, Magnetic Resonance Imaging - Physical Principles and Sequence Design. New York: John Wiley & Sons, Inc.; 1999. 914 pages.

[2] V Kuperman, Magnetic Resonance Imaging, Physical Principles and Applications. San Diego: Academic Press; 2000.

[3] Biomedical Engineering 513 and 564: Course Notes, University of Alberta

[4] MT Vlaardingerbroek and JA den Boer. Magnetic Resonance Imaging 2nd Edition. Heidelberg: Springer-Verlag; 1999. 481 pages.

[5] DK Cheng, Field and Wave Electromagnetics. Reading: Addison-Wesley Publishing Company; 1992.

[6] E Kupce, R Freeman, Optimized Adiabatic Pulses for Wideband Spin Inversion. JMR A, 118:299-303 (1996).

[7] A Tannus, M Garwood, Adiabatic Pulses. NMR in Biomedicine, Vol 10, 423-434 (1997).

[8] RJ Ordidge, M Wylezinska, JW Hugg, E Butterworth, F Franconi, Frequency Offset Corrected Inversion (FOCI) Pulse for Use in Localized Spectroscopy

[9] JM Warnking, GB Pike, A Bandwidth-Modulated Adiabatic RF Pulse for Highly Selective Saturation and Inversion (BASSI). Proceedings of the 11th Annual Meeting of the ISMRM p.2654 (2004).

[10] M Garwood, Y Ke, Symmetric Pulses to Induce Arbitrary Flip Angles with Compensation for RF Inhomogeneity and Resonance Offsets. JMR 94:511-525 (1991).

[11] K Ugurbil, M Garwood, MR Bendall, Amplitude- and Frequency-Modulated Pulses to Achieve 90° Rotations with Inhomogeneous B_1 Fields. JMR 72, 177-185 (1987).

[12] JP Hornak, The Basics of NMR. Rochester Institute of Technology: http://www.cis.rit.edu/htbooks/nmr/.

[13] PS Allen, Some Fundamental Principles of Nuclear Magnetic Resonance. In: M. Bronskill and P. Sprawls. The Physics of MRI - 1992 AAPM Summer School Proceedings. Woodbury: American Institute of Physics, Inc.; 1993. 15-31

[14] PT Callaghan, Principles of Nuclear Magnetic Resonance Microscopy, Oxford University Press, Oxford, 1991.

[15] F Schmitt, MK Stehling, R Turner, Echo-Planar Imaging, Theory, Technique and Application. Berlin and Heidelberg: Spring-Verlag;1998.

[16] ED Becker, JA Ferreti, TC Ferrar, J. Am. Chem. Soc. 91:7784 (1969).

[17] Z Liang and PC Lauterbur, Principles of Magnetic Resonance Imaging. New York: IEEE Press; 2000. 416 pages.

[18] DI Hoult, RE Richards, Critical factors in the design of sensitive high resolution nuclear magnetic resonance spectrometers, Proc. Roy. Soc. Lond. A. **344**:311-340 (1975).

2 Radiofrequency Surface Coils

2.1 Introduction to Radiofrequency Coils

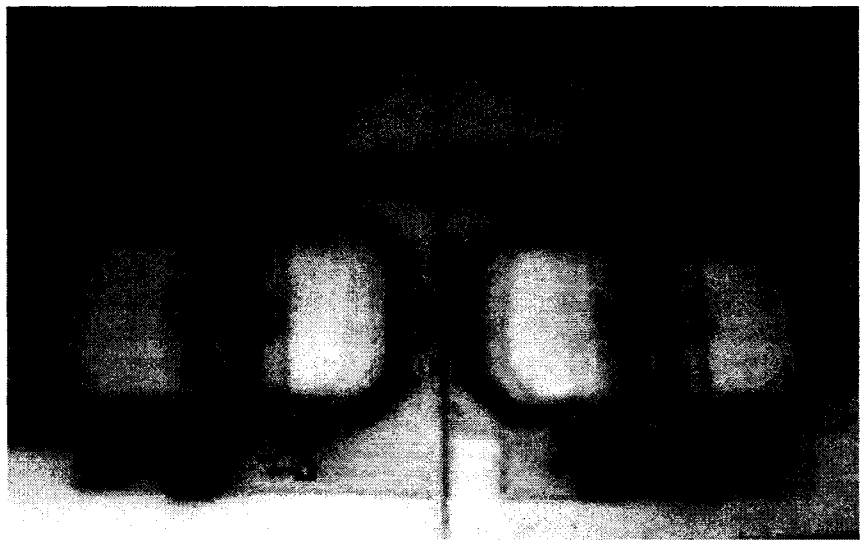

Figure 2.1 An array of four magnetic resonance imaging (MRI) coils, called a "phased array", constructed by the author for use with a 4.7 T magnet. The array acts as a receiver for the MR signal. It is designed to work in conjunction with a commercial circumscribing volume coil and was used for imaging and angiography of human anatomy such as the head and neck.

Radiofrequency (RF) coils serve two primary purposes in the field of MR. Firstly, they are able to perturb a system of nuclear spins into an excited state. Secondly, they are able to convert the magnetic flux from an excited spin system's rotating magnetization into an electrical signal. Coils capable of excitation are called transmit coils, while those which are designed as receivers are known as receive coils.

Note that in the fundamental MR equation $\omega_o = \gamma B_o$, different nuclei may have different γ, and B_o may vary, so an RF coil must be tuned to the appropriate resonant frequency of the nuclei of interest, taking into account the static magnetic field strength, B_o. For ^1H in a static magnetic field of 4.7 T, the Larmor frequency is:

$$\omega_0 = \gamma B_0 = (2.675 \times 10^8 \text{ rad/(T s)})(4.7 \text{ T}) = 1.25725 \times 10^9 \text{ rad/s}$$

$$\omega_0 = 2\pi\nu_0 \rightarrow \nu_0 = 200.098 \text{ MHz} \qquad (2.1)$$

where ν_0 describes the angular frequency of rotation of the transverse magnetization of an excited group of spins. This rotating magnetization obeys Faraday's law of magnetic induction, and is capable of inducing a small but detectable voltage in a coil.

2.2 Receiver Design

2.2.1 Surface Coil Receivers

A "surface coil" is a specialized type of MR coil that is placed adjacent to the sample of interest during experiments. The use of surface coils as receivers is advantageous because the sensitivity can be much greater than other coils, such as encompassing volume coils. The design and testing of surface coils should be performed with their target tissue or an equivalent phantom in place as a load[1]. Often, surface coils are shaped to match the unique structure of the tissues of interest. Human tissue is conductive and as such it has its own electrical properties, which are substantial in comparison to RF coils. The sample that loads the coil becomes part of the coil circuit and coupling may occur between them. The electrical characteristics will not be tuned correctly if the desired sample is not used to load the coil during design and construction. The sample should be placed as close to the coils as possible, in order to maximize receive sensitivity[2]. A falloff in sensitivity is present in regions further from the coil.

A simple surface coil can consist of a single conductive loop attached to the magnet's receiver channel in some manner, such as with a coaxial cable. In order to maximize sensitivity, the coil loop should be oriented perpendicular to the static magnetic field. The reason for this is because when a group of spins is excited, the rotating transverse

magnetization lies in a plane perpendicular to the static field. This rotating magnetization will maximally induce a voltage in a coil with a perpendicular orientation to the static field.

Ideally the coil will receive signal from only the tissues of interest. Outside noise sources such as radio stations (if the magnet room is not securely RF shielded) or electrical noise from faulty light bulbs can easily be picked up by MRI coils, and appear in images as artefacts at their respective frequency. As well, no radiation whatsoever from the coil is desired when it is receiving the MR signal. Radiation of electromagnetic waves would result in additional losses and power deposition in the sample. It could also potentially excite spins.

Inductive and capacitive coupling need to be considered when working with surface coils. Inductive coupling involves a mutual inductance forming between two current-carrying wires. With capacitive coupling, an electric field is formed between two conductors. This occurs in a similar manner to manufactured capacitors, which have two conducting parallel plates separated by an insulator (dielectric). Electrically conductive tissue can couple both inductively and capacitively with coils[3]. Coupling can also occur between the receiving coil and other nearby coils such as the transmit coil; one way to mitigate this is with specialized decoupling circuitry[4].

To receive MR signal from ^{1}H in a 4.7 T magnetic field, a surface coil needs to be designed to be sensitive within a bandwidth of approximately 10-20 kHz around a centre frequency of 200 MHz, and thus a simple inductor/capacitor (LC) circuit can be used[5]. To make the coil maximally receptive, it can be tuned such that it resonates at this centre frequency[6]. A graph of the tuned coil response over a frequency range around the centre frequency will show a single peak in sensitivity.

The impedance of a capacitor is $1/j\omega C = -j/\omega C = -jX_c$, and an inductor is $j\omega L = jX_L$, where X_L and X_C are termed reactances[7]. The design process makes use of the simple series resonant LC circuit equation, noting that reactances in series add:

$$j\omega_0 L + (-j/\omega_0 C) = 0 \rightarrow \omega_0 L = 1/\omega_0 C \rightarrow \omega_0 = \frac{1}{\sqrt{LC}} \qquad (2.2)$$

where ω_0 is the resonant frequency of the coil and is designed to be equal to the Larmor frequency, L is the inductance of the coil, and C is the coil capacitance.

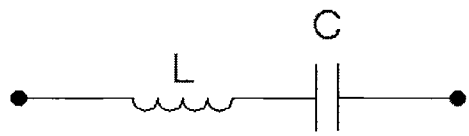

Figure 2.2 A series LC circuit. This can also be thought of as a simple representation of an isolated surface coil. Basic coils are composed of a copper foil loop with some inductance L. Capacitance C is added and the value adjusted so that its reactance resonates with the inductance. An additional resistance is also present in real surface coils (not shown).

Also important in many coil circuits is the parallel resonant circuit, and using the standard impedance divider equation[8] for parallel impedances we see:

$$j\omega_0 L \,//\, (-j\omega_0 C) = \frac{j\omega_0 L(-j/\omega_0 C)}{j\omega_0 L - j/\omega_0 C} \qquad (2.3)$$

where, // symbolizes parallel, and at resonance, $j\omega_o L + (-j/\omega_o C) = 0$, so that the net impedance is very large.

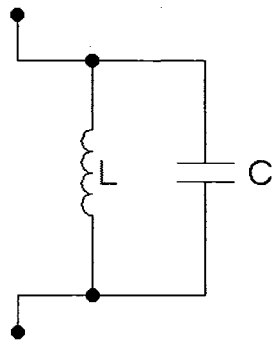

Figure 2.3 A parallel LC circuit. This basic circuit is used in many high-field coils today, including volume coils and surface coils. If the inductance and capacitance are tuned to the appropriate frequency, they create a large impedance which serves to block or at least significantly reduce currents flowing through the circuit.

Ideally a surface coil receiver would have a uniform receive sensitivity profile, and this uniform profile would only extend throughout the target tissue volume. In reality, this is not the case, because in practice, surface coil receive sensitivity is not uniform but falls off with distance from the coil. A coil that is more electrically active on one side than the other will have a less uniform sensitivity profile. That is, if an excited, rotating group of spins equidistant from both sides of a coil are inducing a greater voltage on one side of the coil than the other, one cannot say that both sides of the coil are equally sensitive to the NMR signal. Thus, the coil is said to be unbalanced[1].

A surface coil LC circuit can be as simple in practice as a conducting circular loop with an inherent inductance, in series with a single capacitor[9]. However, for in-vivo MRI, the coil dimensions are usually large enough that such a design would cause a significant difference in electrical characteristics between the side of the coil with the capacitor and the other side. This would create a nonuniform receive profile. One method of improving the uniformity of the receive sensitivity is to use a distributed capacitance. The

capacitance can be broken up into several small capacitors located at different positions around the coil loop.

When the induced MR electrical signal travels through a conductive pathway such as the copper wire of a receiver coil, it has a frequency f, and a wavelength, λ. The standard inter-capacitor distance for MRI is $\lambda/20$[10]. If this is satisfied, then each piece of conductive copper wire between capacitors can be considered a discrete (lumped-element) component. If the wire is longer than $\lambda/10$, then one must consider the non-uniform current distribution across it. Noting that capacitors by definition have electric fields between their two conducting sides, steps (ie. shielding or placement) should be taken to insure that these fields do not interact excessively with local portions of the sample.

2.2.2 The Phased Array

A four coil phased array was constructed by the author for 4.7 T use. Each coil of the array was first individually tested, tuned and matched, and decoupled, and then the coils were tuned for use in pairs. In the design, it was attempted to account for coupling interactions between each coil and between the array and the circumscribing volume coil. A network analyzer was used to first bench test the phased array, and then the array was used to acquire MRI images with a 4.7 T Varian magnet.

The historical term "phased array" is still in use today, even though there is no phase locking, and signals from the multiple coils are not summed with fixed phase. The phased array comprises two or more surface coils, each independently receiving the NMR signal. Each surface coil is usually identical to all the others.

The advantage of using the phased array is that its multiple surface coils can receive signal simultaneously and independently. Thus, a phased array is capable of attaining

similar SNR to small surface coils, over a large FOV, with no increase in imaging time. A phased array can have superior SNR to that of a single coil[11] (having the same shape and total dimension). In addition, it can mitigate high field destructive interference effects[12] that cause a falloff in receive sensitivity with circumscribing coils. Also, with a phased array, the use of parallel imaging techniques such as sensitivity encoding[13] is possible.

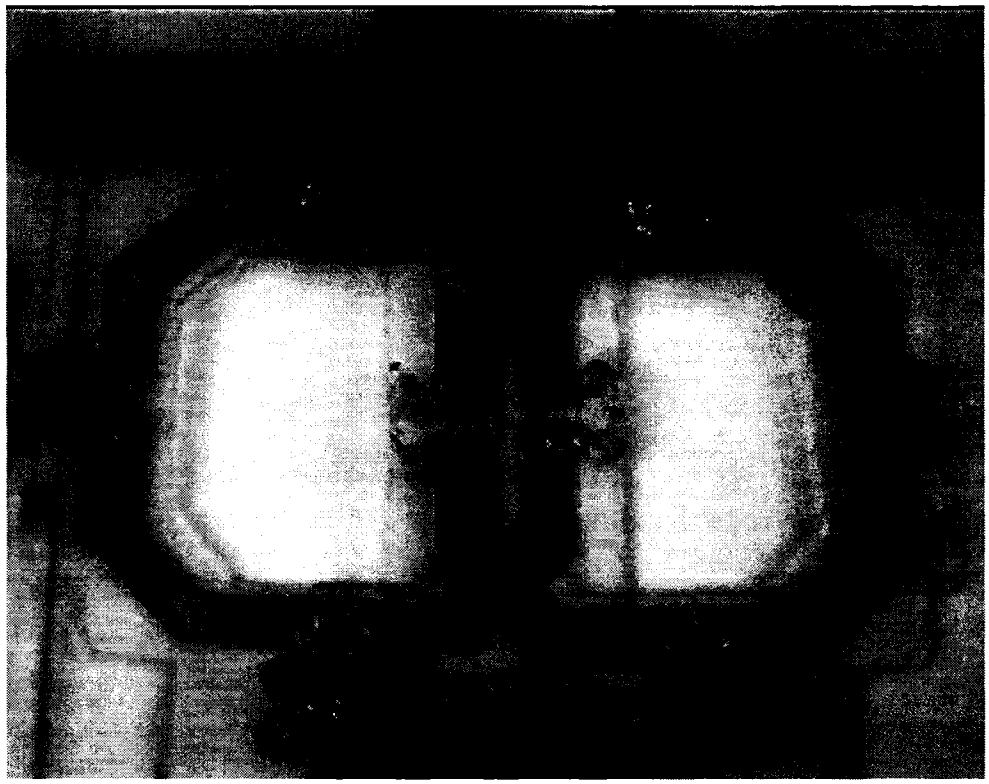

Figure 2.4 Two coils of a four coil 4.7 T MRI phased array constructed by the author for imaging of the head and neck. Thin copper foil provides the coil loop, with capacitors distributed throughout. At the bottom of each coil is the passive decoupling circuit, an inductor and crossed diodes in parallel with a capacitance. At the top, the received signal and ground lines are connected to a coaxial cable that leads to the magnet preamplifier (preamp) inputs. The electrical schematic corresponding to each coil shown above is in Figure 2.10.

2.2.3 Mutual Decoupling with Coil Overlap

Any coupling that occurs between multiple coils causes noise and signal transmission between them, and in effect, the coils are no longer independent receivers and may become detuned. Thus, coupling can result in a decrease in SNR. In addition, it degrades MR parallel imaging performance[14]. The coupling can involve a form of inductive coupling with the sample as an intermediary. Or, it can involve a mutual inductance that is created between two conducting loops in close proximity.

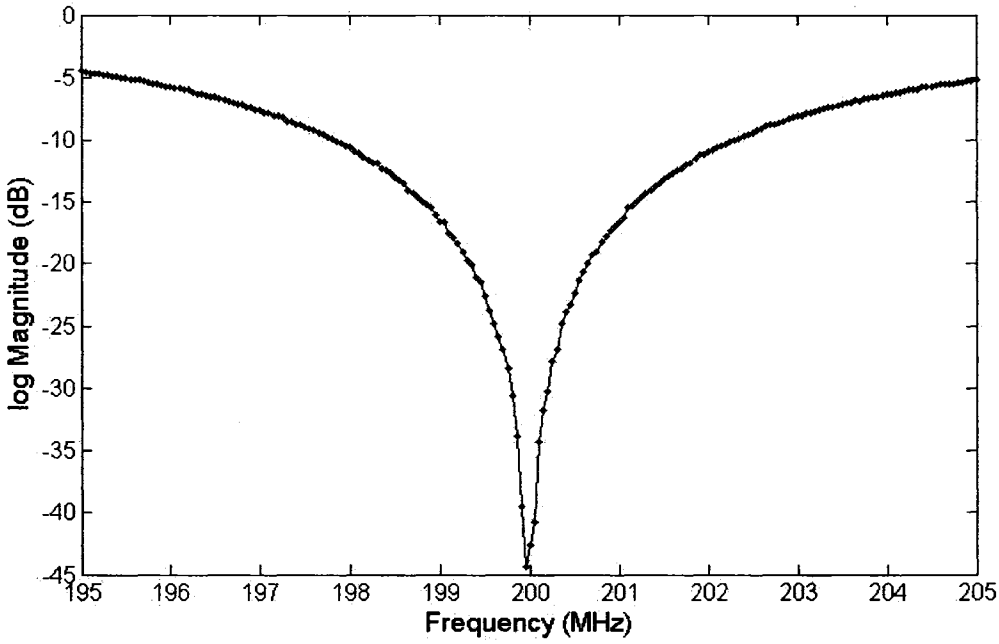

Figure 2.5 Frequency response data trace of an isolated 4.7 T surface coil as measured by a network analyzer. The coil was designed and constructed by the author. It has a single dip in response at the Larmor frequency (200 MHz) and thus is well tuned. A similar frequency response can be measured from two overlapping coils, but only if the coils are decoupled correctly.

Suppose a single coil is tuned in isolation to the Larmor frequency. A graph of the frequency response of the coil over a frequency bandwidth around the centre frequency

should show a single peak (or dip, depending on the type of measurement) in sensitivity at the Larmor frequency. If a second coil, which also was independently tuned, comes in close proximity to the first, they may magnetically couple. That is, the coils become electrically connected through a mutual impedance. The frequency response of the two coils as measured by a network analyzer will thus change significantly, and may show more than one peak, both offset from the centre frequency. Hence, the detuned coils will be much less sensitive to signal at the Larmor frequency.

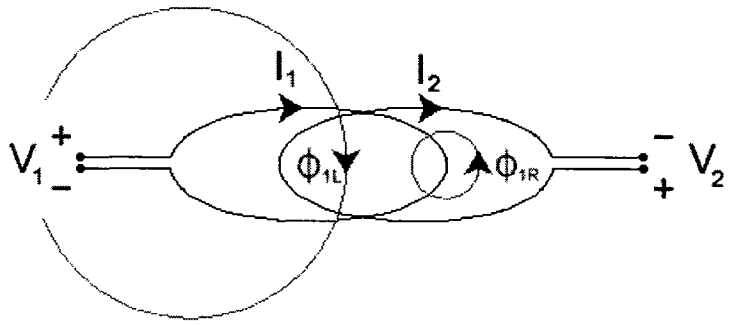

Figure 2.6 Magnetic flux coupling between two overlapped coils. Coil 1 has a current I_1 flowing through it. By the right hand rule, the direction of magnetic flux produced by the current-carrying wires is as shown. Φ_{1L} is the flux through the region of overlap produced by current in a segment of wire on the left side of coil 1, and Φ_{1R} is the flux produced by current on the right side of coil 1. Coil 2 also produces similar magnetic flux (not shown). Both Φ_{1L} and Φ_{1R} contribute to the magnetic flux through each coil, and are actually distributions of flux, which fall off with distance from the wires.

One method of reducing mutual inductive coupling between coils involves overlapping them. If coils overlap with the correct placement, the mutual inductance can be negated somewhat, and the response of each coil will return to a single peak at the centre frequency. Two circular coils can be decoupled in this manner by gradually moving them across each other so that the loops overlap until the desired single resonance response is created. The mechanism behind this is a summation and cancelling of the magnetic flux that the currents in the coils generate.

2.2.4 Tuning and Matching

Coils are tuned individually to the Larmor frequency of the nuclei of interest. At 4.7 T, the Larmor frequency is approximately 200 MHz for ^{1}H. By tuning the circuits to the Larmor frequency, we maximize their transmit and receive sensitivity to that frequency. Coils are matched to 50 Ω impedance. The purpose of matching is to attempt to minimize noise and provide a good transference of signal to the coaxial cable, as well as providing a proper mismatch if low input impedance preamplifiers are used.

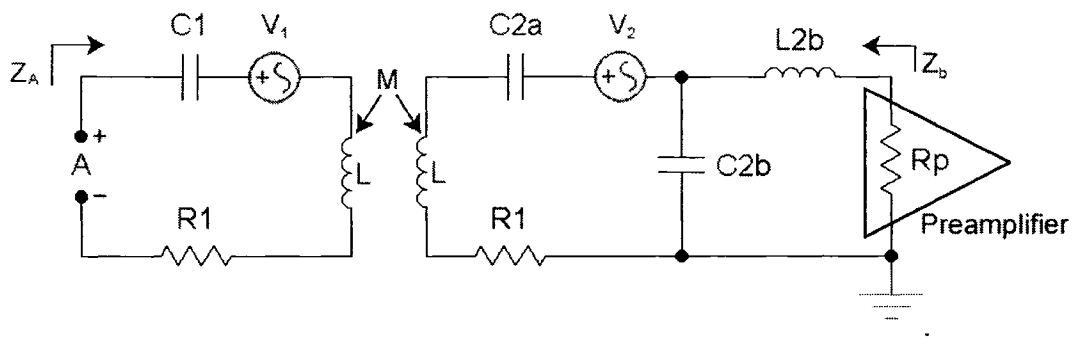

Figure 2.7 Transformer model of two coils in a phased array[15], which illustrates how tuning and matching a phased array and inter-coil coupling can be examined with conventional lumped-element circuit analysis techniques. Coil 1 is identical to coil 2 and also has a capacitor, C_{1b}, inductor, L_{1b}, and preamplifier (not shown). Coil 1 on the left couples with coil 2 on the right, and they may share a mutual inductance between them, M. The induced MR voltage is represented in each coil as V_1 and V_2. R_p is the preamplifier input impedance as seen by each coil. Coaxial cables may connect each coil to its corresponding preamp.

Insight can be gained by considering two surface coils and their mutual coupling interactions, modelled as the primary and secondary windings of a transformer[15]. Coil #1

is the primary and has a capacitance C_1, resistance R_1, and inductance L, an induced NMR signal V_1, and mutually couples with a second, identical coil, through a mutual impedance, M. Coil #2 is the secondary, has induced NMR signal V_2, and has the same lumped elements, except let us consider its capacitance split into two, C_{2a} and C_{2b}. In parallel with C_{2b} is some inductance L_{2b} in series with the input impedance of a preamplifier. The total impedance seen looking at each coil from its corresponding preamplifier is Z_b. Looking the other way, R_p is the input impedance of each preamplifier as seen by its corresponding coil.

By definition, when coils are tuned to resonate at a certain frequency, their impedance Z = R + jX is minimized such that the reactance is cancelled out and becomes zero, so Z = R. If the coils are tuned to resonate at the 4.7 T Larmor frequency then $\omega = \omega_o$ and the tuning networks involve X_L and the capacitive reactances:

$$X_L - X_{C1} = 0 \qquad (2.4)$$

$$X_L - (X_{C2a} + X_{C2b}) = 0 \rightarrow X_L - X_{C2a} = X_{C2b} \qquad (2.5)$$

It is assumed that each coil operates essentially in isolation. This assumption is justified if the coils are decoupled in some manner such that any shared impedance, M, is negligible. Remembering that at the resonant frequency $X_L - X_{C2a} = X_{C2b}$, and assuming complete isolation, the total impedance seen looking at each coil from the preamplifier input impedance is (proved in Appendix A):

$$Z_b = \frac{X_{C2b}^{\ 2}}{R_1} + j(X_{L2b} - X_{C2b}) \qquad (2.6)$$

$-jX_{C2b}$ and jX_{L2b} form the matching network (jX_{L2b} is optional for matching). C_{2b} is part of both the tuning and matching network so tuning and matching are not independent. At any rate, the coils are matched to 50 Ω. That is, Z_b = 50 Ω when, looking at the above

equation, $X_{L2b} - X_{C2b} = 0$ and $X_{C2b}^2/R_l = 50$, which gives a value for X_{C2b}. Thus, we have gone through the basic equations for designing an entire surface coil.

2.2.5 Decoupling with Low Input Impedance Preamplifiers

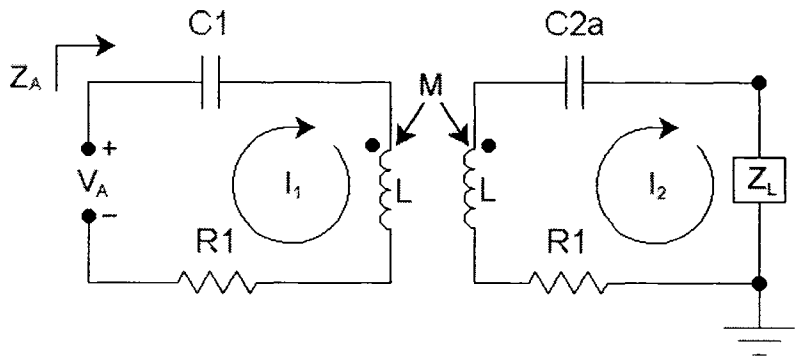

Figure 2.8 Transformer model of two coils in a phased array, with induced MR voltages removed for calculation of the input impedance at terminal A, Z_A. This terminal has an associated open circuit voltage V_A. Coil 2 drives a load Z_L, which consists of L_{2b}, C_{2b}, and the preamp input impedance R_p. Coil 1 is identical to coil 2 and also drives a load Z_L (not shown). Coil 1 on the left couples with coil 2 on the right, and they share a mutual inductance between them, M, which needs to be significantly reduced in order to improve coil isolation.

The output received by RF probes eventually works its way through the RF chain to the input of the preamplifiers. A standard coaxial cable, made of a centre conductor surrounded by a grounded cable shield, connects the surface coil from its position in the magnet bore, to the preamplifier at the back of the magnet. Alternatively, the preamp may be located adjacent to the coil without an intervening cable, with the preamp output running through a cable to another preamp at the back of the magnet. From the preamps, the signal eventually makes its way through an analog-to-digital converter, among other things, and finally is fed into a digital computer.

One might think that the input impedance of the preamplifiers would be set to the conventional 50 Ω for maximum power transfer. This, however, is not the case. Usually the input impedance of the preamplifiers is designed to be extremely low, on the order of 2 Ω[15]. A mismatch between the coil and the preamplifier is done intentionally, with the coils matched to 50 Ω. In order to understand the reason for the mismatch, consider what happens when multiple coils of a phased array are placed in close proximity to the sample of interest, conducting tissue. Substantial inductive coupling between the coils can take place with the sample as an intermediary. Purely resistive mutual impedance is possible because the sample is lossy, that is, the tissue can act as a resistor connected between coils. This impedance effectively acts as an electrical connection between coil receiver channels, and is a source of transmission of noise and signal between coils (noise correlation and crosstalk)[1].

Suppose the coils are tuned separately to the Larmor frequency so that $X_L - X_{C1} = 0$ and $X_L - (X_{C2a} + X_{C2b}) = 0$. From Figure 2.8, one can calculate the input impedance, Z_A, as follows (proved in Appendix A):

$$Z_A = R_1 + \frac{\omega^2 k^2 L^2}{R_1 + \frac{X_2^2}{R_p}} \qquad (2.7)$$

If the first coil is isolated, the impedance seen at terminal A is R_1. If the second coil is present, the impedance seen at terminal A is Z_A. The second term of this equation is the noise power[15], and if it is eliminated then the noise resistance becomes R_1. If R_p or k approaches zero, Z_A approaches R_1, and thus coil isolation is improved.

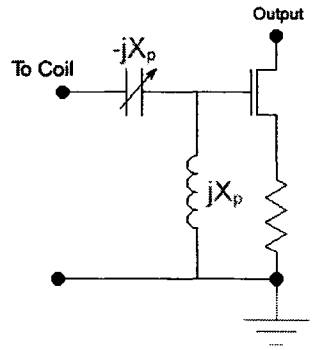

Figure 2.9 Detail of the input terminal of a Gallium Arsenide Metal Oxide Semiconductor Field-Effect Transistor preamplifier. RF coils are connected to the input, and the output signal goes to the MR computer for analysis. The capacitor $-jX_p$ and inductor jX_p are series resonant at the Larmor frequency, and serve to transform the 50 Ω at the preamp input to 1-2 MΩ at the input of the transistor. This common source transistor has very high input impedance itself, thus it acts similarly to an open circuit, so that the capacitor and inductor become a low impedance signal path to ground. This is how the low preamplifier input impedance is created.

The mismatch between the coil and the preamplifier reduces coil current by increasing the impedance seen by the coil, but maintains the same level of SNR[1]. It is critical to avoid SNR loss because one of the main purposes of using surface coils is to increase the SNR of the received NMR signal. With low input impedance preamplifiers, the impedance seen by the coil at the input of the preamplifier becomes an order of magnitude greater. As a result of the corresponding current amplitude decrease, the magnitude of the inductive coupling between multiple coils decreases. This, in turn, reduces crosstalk between receiver channels. Thus, the low input impedance of the preamplifiers effectively serves to improve the inductive decoupling and isolation of individual coils. Note that, though the coil current amplitude is decreased, the MR voltage signal is essentially not affected. The induced MR signal is received by the preamplifier with negligible degradation to the SNR because a low input impedance preamp measures, in effect, the open circuit voltage of the coil[1].

Consider again Figure 2.7. If jX_{L2b} is set so that jX_{L2b} and $-jX_{C2b}$ are a parallel resonant circuit ($jX_{L2b} - jX_{C2b} = 0$), and supposing an ideal preamplifier input impedance of zero, then no current will flow in the coil at the resonant frequency[15]. Thus the coils are effectively isolated at the resonant (Larmor) frequency, because coupling interactions are eliminated. The NMR voltage signal V_2 will still be induced in the coil even if no current flows, and it will appear at the preamplifier input with full SNR because the MR voltage across C_{2b} is independent of R1[1]. In reality, zero input impedance is impossible; practical preamplifier input impedance is on the order of 0.3 to 3 Ω. If a λ/2 coaxial cable connects the coil and preamp, additional losses occur, and the effective preamplifier input impedance increases by another 1 to 2 Ω as seen by the coil.

2.2.6 Receive-Only Decoupling Circuitry

When a circumscribing volume coil, such as a birdcage coil[16], transmits power to the sample, the surface coil can become part of the transmission circuit and interfere. Ideally, when the volume coil transmits, any surface coil receivers it surrounds are inactive and electrically isolated from it. Similarly, when receiving NMR signals, the volume coil should be inactive, and the receiver coils should be at their maximum sensitivity. A commercial transmit-only, receive-only (TORO) volume coil[17] was utilized on the 4.7 T system, with the built-in capability to decouple itself from surface coils during the receiving process.

Passive decoupling[18] was used to electrically decouple the constructed surface coils from the transmitting coil. An inductor is placed in parallel with one of the tuning capacitors distributed around the surface coil. In series with the inductor is a pair of non-magnetic crossed diodes, which act in tandem as a switch. The inductor is tuned such that when the voltage across the diodes causes the inductor to be electrically active with its parallel capacitor, the passive decoupling circuit net inductance resonates with the capacitor. When the head coil is not transmitting, the voltage across the diodes is insufficient to

activate them, and they thus present an open circuit, and so the inductor that they are in series with is not part of the circuit. Hence, the parallel LC circuit is inactive, and the coil can receive signal normally. When the head coil transmits an RF excitation pulse, a large voltage may be induced in the surface coil through coupling interactions. If the voltage is large enough, then the crossed diodes become conductive, and so the parallel LC passive decoupling blocking circuit becomes activated. As such, the impedance becomes large and current flow through the coil is decreased, effectively reducing coupling interactions, and preventing potentially harmful, large currents from flowing near human tissue.

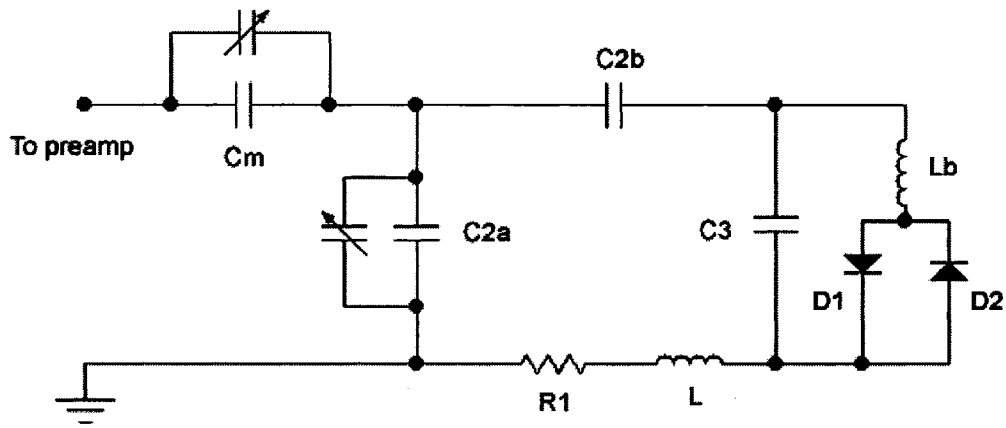

Figure 2.10 Schematic of a single coil of a 4.7 T phased array that was constructed by the author, with a passive decoupling circuit comprising a capacitor C3, an inductor Lb, and a pair of crossed diodes D1 and D2. Four of these coils were built and tested for imaging of the head and neck. Low input impedance preamps and coil overlap were relied upon to decouple the coils. Note the somewhat different circuit elements used in this case as compared with Figure 2.7. Instead of an inductor at the coil output, a tuned variable capacitor was used to provide the correct inductance at the preamplifier input[15]*. Refer to Appendix A for component values.*

Another method of decoupling, called active decoupling[19], involves the use of active diodes that are turned on and off by a switched voltage control. When the diode is active, it decouples the coil from other nearby coils. This explicit control is superior to passive decoupling, because it allows precise control of the timing of the decoupling, and there are no ambiguities as to whether or not the coil is actually being decoupled from the circumscribing volume coil, at the correct times.

2.2.7 RF Trap

Often the individual surface coils in a phased array each have their own coaxial cables connecting them to the preamplifiers. Coaxial cables consist of an outer shield, which ideally is at ground potential, surrounding an inner conducting wire that carries the MR signal. Interactions can occur by coupling between the coaxial cable shields and other cables, the coils themselves, or even the sample. Creating a high impedance circuit with the cable shield can reduce these interactions. To do this, the coaxial cable is coiled up so that it forms an inductor, and a tuned capacitor is placed in parallel with this inductance. The parallel capacitor and inductor, if tuned to resonate at the Larmor frequency, will reduce the magnitude of currents induced on the cable shield at this frequency. Thus this parallel LC loop circuit reduces cable shield coupling interactions[1] and is called an RF trap. It should itself be shielded so that it does not act as an additional surface coil receiver, or interact with other parts of the circuit.

2.2.8 Testing of the Phased Array

The phased array that was constructed by the author was fully bench tested before being used to acquire images on the 4.7 T magnet. Each coil of the phased array was first separately tuned to the Larmor frequency of ^{1}H at 4.7 T, and matched to 50 Ω, while loaded with a phantom. Tuning and matching behaviour was confirmed with a network

analyzer, an instrument that was used to measure each coil's response over a frequency range centred on 200 MHz.

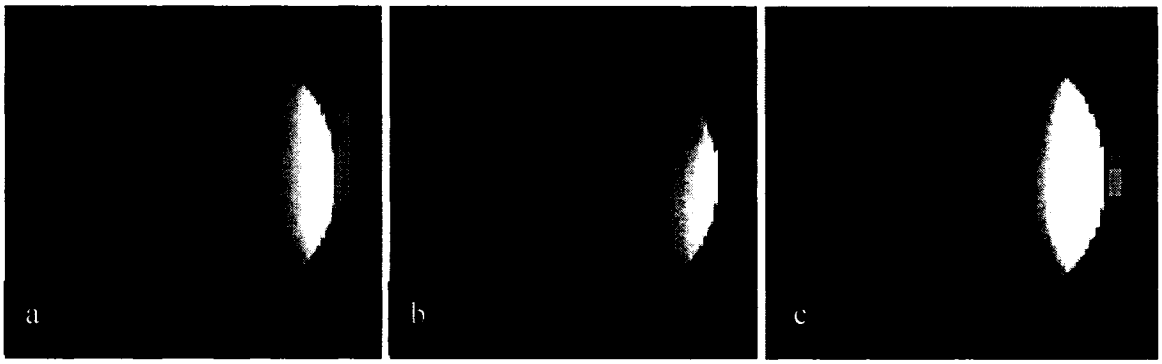

Figure 2.11 Cylindrical phantom test of the four coil phased array with the 4.7 T magnet. A pair of coils (#1 and #2) was placed on the right side of the phantom and set to receive, with the second pair of coils (#3 and #4) turned off and placed on the other side in order to demonstrate the effect of coupling interactions. (a) Coil #1 is set to receive alone. The grey rectangle represents the coil. (b) Surface coil #2 is set to receive alone. Coils #3 and #4, located on the left side, transmit some signal and noise to coil #2 through a mutual coupling interaction. This does not happen with the commercial coils[20] that were used for the images in later chapters. (c) Coils #1 and #2 are tested in combination, with the light gray area indicating coil overlap. Notice the SNR improvement due to the combination.

After it was confirmed that each coil was performing correctly independently, coils were paired, and the two pairs were tested separately with the network analyzer. For each pair, overlapping by approximately 3 cm decreased mutual coupling interactions.

Once it was confirmed by bench tests with the network analyzer that both pairs of coils were receiving signal correctly, all coils were combined together to form the four coil phased array. MR images of phantoms were acquired first to verify correct functionality. Subsequent to this, in-vivo imaging was tested.

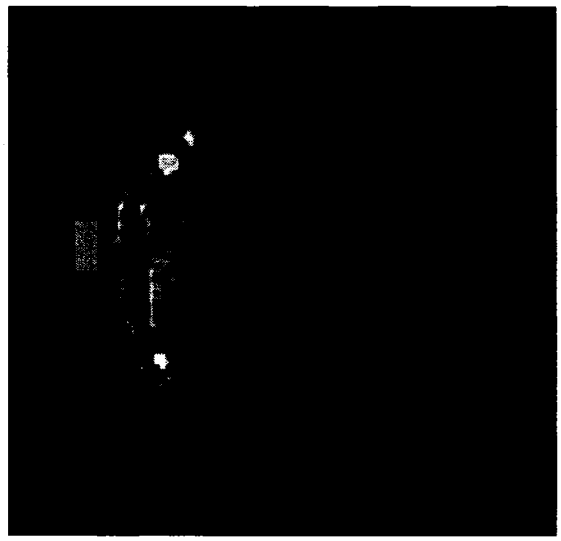

Figure 2.12 In-vivo neck image taken with a single pair of coils from the four coil phased array. This 2D FLASH image shows a cross section of the vasculature in the neck. The two coils are represented as rectangles. The light grey area indicates coil overlap.

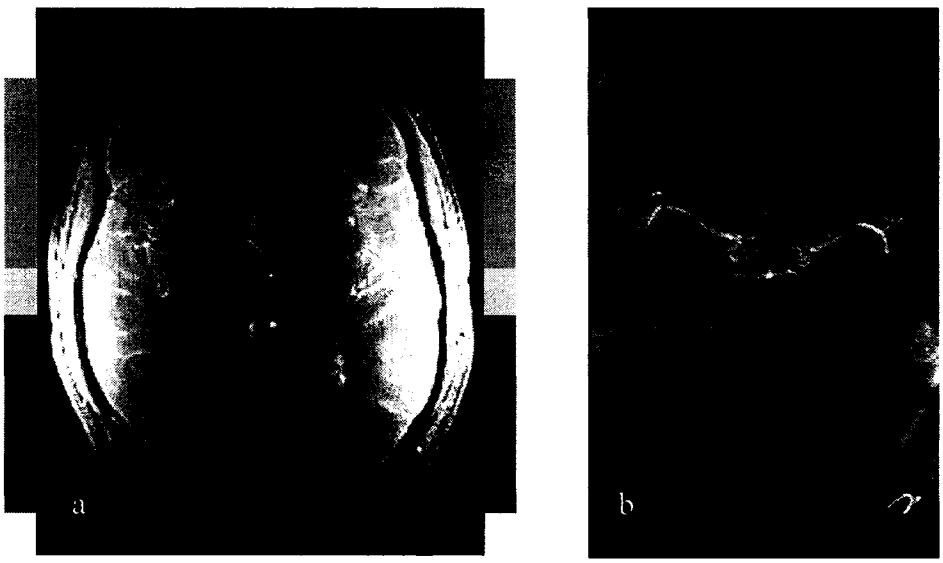

Figure 2.13 4.7 T images acquired with the four coil phased array constructed by the author. a) 4.7 T 2D MRI FLASH image of the human brain. Placement of each of the four coils is indicated by the rectangles. Notice the rapid signal falloff from the sides of the head. It is possible to receive signal with higher SNR, deeper in the brain, with a set of commercial 4.7 T coils[20] shaped to fit the contours of the human head. b) 3D MR angiography image. This is a Maximum Intensity Projection (MIP)

2.2.9 High Field Effects

There were some unexpected consequences of using low field, lumped-element circuit techniques to build high field, high frequency surface coils. The familiar, symmetric low field surface coil sensitivity profiles did not appear at 4.7 T when the coils were loaded properly with actual tissue or phantoms. Granted, part of the effect is due to the inhomogeneous B_1 transmit field of the circumscribing coil. But it turns out that destructive interference effects distort the receive sensitivity profiles of surface coils at high field as well. The profiles become antisymmetric, and appear to be rotated and shifted somewhat.

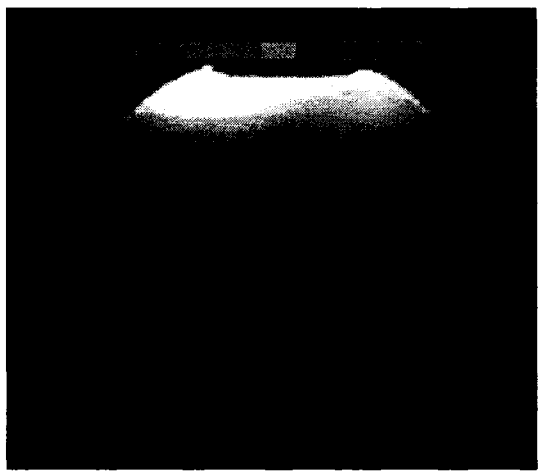

Figure 2.14 Example of high field destructive interference effects in a phantom at 4.7 T using a birdcage coil for transmission and a pair of coils from the constructed phased array for receiving. The phantom contains copper sulphate and salt, and its conductive properties lead to a distortion at 4.7 T of both the transmit coil B_1 field and receiver sensitivity. An image of the phantom at lower fields would show a much more symmetric profile.

2.3 Conclusion

A four coil phased array was constructed and tested with a 4.7 T magnet. A network analyzer was first used to bench test each of the four coils of the array, as well as the coils used in combination. After passing bench tests, the coils were tested on phantoms within the magnet, and MRI images were acquired both with phantoms and humans. Tuning and matching were performed for each coil in isolation first, and then with combinations of the coils. Mutual coil interactions were reduced by coil overlap, and the results confirmed on the network analyzer. Passive decoupling circuitry was built for isolating the array from a circumscribing volume birdcage coil.

For the final images, it was decided to move to a commercial phased array coil[20], because its irregular shape is designed with a tighter fit to the human head, thus providing higher SNR. As well, the commercial coil offers active decoupling, RF traps on the cables, and balanced/unbalanced transformers (baluns[21]). Baluns balance the voltage distribution and provide an additional means of reducing power dissipation. Furthermore, the commercial coil has superior decoupling of coil-coil interactions, even without coil overlap[22], due to the very low input impedance of its preamplifiers (approximately 0.3 Ω). This was primarily accomplished by placing the main preamplifiers adjacent to the coil, inside the magnet[23]. The purpose of doing this is to prevent the resistance of the cables and connectors from adding to the impedance seen by the coils, looking into the preamp. The constructed coils had cable running between the coil and a tune box containing capacitors, as well as another cable running from the tune box to the preamplifier. Such a configuration produces unnecessary losses through the cables and the connectors.

Local receive coils provide a means of increasing the signal near the surface of objects, compared to using volume coil receive. This signal increase is possible because the receive coils are in closer proximity to the subject as compared with volume coils. A distortion of signal sensitivity due to destructive interference effects is present in high field images acquired with circumscribing volume coils. In particular, transmission and

receive sensitivity with volume coils is strongest in the centre of the head, and weaker at the sides. It was theorized that this effect can be negated somewhat by acquiring instead with a phased array and taking advantage of its higher receive sensitivity at the sides of the head. This will be examined in later chapters.

2.4 Bibliography

[1] DM Peterson, RG Duensing, JR Fitzsimmons, MRI basics and coil design principles. RF Design January 56-64 (1997).

[2] E Fukushima, SBW Roeder, Experimental Pulse NMR: A Nuts and Bolts Approach. Reading: Addison Wesley; 1981.

[3] WI Orr, Radio Handbook, 22nd ed. Indianapolis: H.W. Sams; 1981.

[4] MR Bendall, A Conelly, JM McKendry, Elimination of Coupling Between Cylindrical Transmit Coils and Surface-Receive Coils for In Vivo NMR MRM 3:157-163 (1986).

[5] AS Sedra, KC Smith. Microelectronic Circuits, 3rd ed. New York and Oxford: Oxford University Press; 1991.

[6] Nishimura DG. Principles of Magnetic Resonance Imaging. Stanford: Stanford University; 1996

[7] EA Guillemin, Introductory Circuit Theory. New York: John Wiley & Sons; 1953.

[8] JD Irwin, Basic Engineering Circuit Analysis, 4th ed. New York and Toronto: Macmillan; 1993.

[9] CE Hayes, WA Edelstein, JF Schenck, Radio Frequency Resonators, Chapter 72, pp. 1183-1200, in Magnetic Resonance Imaging, Vol. II, W. B. Saunders, Co., 1988.

[10] C-N Chen, DI Hoult, Biomedical Magnetic Resonance Technology. Adam Hilger, New York, 1989.

[11] ZA Fayad, TJ Connick, L Axel, An Improved Quadrature or Phased-Array Coil for MR Cardiac Imaging. MRM 34:186-193 (1995).

[12] A Kangarlu, BA Baertlein, R Lee, T Ibrahim, L Yang, AM Abduljalil, PM Robitaille, Dielectric Resonance Phenomena in Ultra High Field MRI. Journal of Computer Assisted Tomography 23 (6), 821-831.

[13] KP Pruessmann, M Weiger, MB Scheidegger, P Boesiger, SENSE: Sensitivity Encoding for Fast MRI. MRM 42(5):952-962 (1999).

[14] M Weiger, KP Pruessmann, P Boesiger, 2D SENSE for Faster 3D MRI. MAGMA 14(1):10-19 (2002).

[15] PB Roemer, WA Edelstein, CE Hayes, SP Souza, OM Mueller, The NMR Phased Array. MRM 16:192–225 (1990).

[16] A Haase, F Odoj, M Von Kienlin, J Warnking, F Fidler, A Weisser, M Nittka, E Rommel, T Lanz, B Kalusche, M Griswold, NMR Probeheads for In Vivo Applications. Concepts in Magnetic Resonance 12 (6) 361-388 (2000).

[17] EA Barberi, JS Gati, BK Rutt, RS Menon, A Transmit-Only/Receive-Only (TORO) RF System for High Field MRI/MRS Applications. MRM 43:284-289 (2000).

[18] WA Edelstein, CJ Hardy, OM Mueller, Electronic Decoupling of Surface-Coil Receivers for NMR Imaging and Spectroscopy. JMR 67:156-161 (1986).

[19] N De Zanche, Anatomically-Tailored RF Probes for NMR. PhD thesis, University of Alberta; 2002.

[20] PulseTeq, England.

[21] Terman FE. Radio Engineers' Handbook. New York and London: McGraw-Hill Book Company; 1943.

[22] PJ Ledden, S Inati, Four Channel Preamplifier Decoupled Phased Array for Brain Imaging at 1.5 T. Proceedings of the 9th Annual Meeting of the ISMRM p.1117 (2001).

[23] DW Carmichael, DL Thomas, E De Vita, MA Fernandez-Seara, N Chhina, M Cooper, C Sunderland, C Randell, R Turner, RJ Ordidge, Improving Whole Brain Structural MRI at 4.7 Tesla using 4 Irregularly Shaped Receiver Coils. NeuroImage 32:1176-1184 (2006).

3 High Field Imaging Sequences

3.1 Introduction

T_1-weighted imaging with gradient echo pulse sequences has evolved since the days of spoiled FLASH. Magnetization-prepared (MP) pulse sequences are one of the current clinical standards for structural T_1-weighted imaging, but have not yet been fully explored in the literature. The author developed magnetization-prepared gradient echo pulse sequences for T_1-weighted human brain imaging using a simple sequence as a starting point. The MP sequence was fully tested both on phantoms and in-vivo using a 4.7 Tesla Varian magnet and spectrometer. Tests were conducted using both a phased array coil and a volume coil for receiving.

One purpose for utilizing magnetization preparation for brain imaging is to maximize grey matter (GM) and white matter (WM) contrast, while maintaining reasonable individual signal levels, and minimizing cerebrospinal fluid (CSF) signal intensity. It has been proven that segmented MP sequences are superior to FLASH in this regard[1]. In addition, high field B_1 inhomogeneity can be compensated somewhat by careful MP pulse sequence design.

3.2 High Field Effects

3.2.1 Destructive Interference at 4.7 T

An effect that has dominated high field MR research over the past decade is the destructive interference of electromagnetic waves[2], also termed "dielectric resonance effects"[3], or "field focussing" in the literature. Ideally, signal intensity across the brain should be constant within individual tissue classes, so that contrast has a spatially

uniform profile. High field destructive interference causes a falloff of signal across each tissue in the brain, with a centrally-located hotspot of intensity. This effect is virtually nonexistent at 1.5T; at 3 T it is noticeable. At 4.7 T, it is a major consideration for both imaging and angiography with large FOV slices.

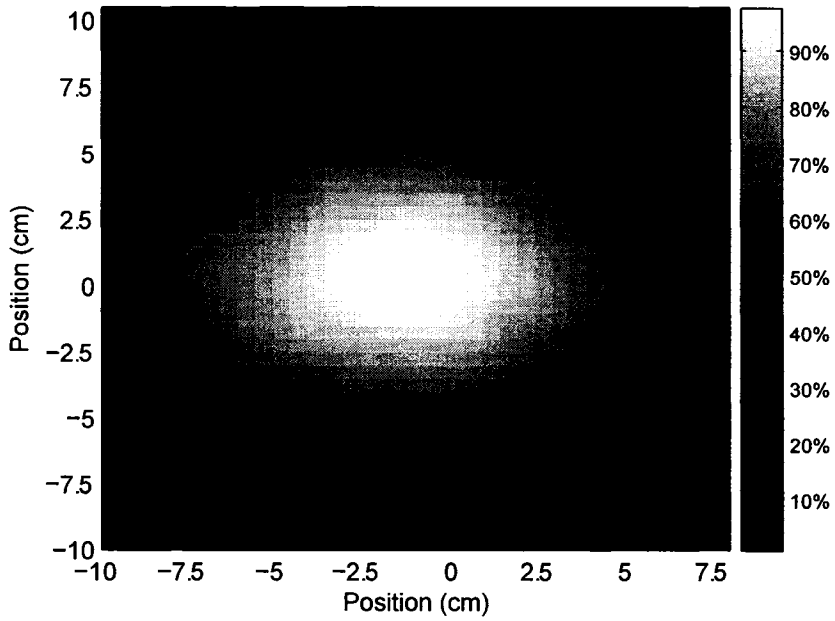

Figure 3.1 1 cm thick axial slab of a finite element model of the spatial B_1 distribution of the head in a 16 rung birdcage coil at 200 MHz (4.7 T static magnetic field strength). The eyes are on the left side of the figure. Grey scale bar on the right side of the figure indicates correspondence of each shade of grey to percent of maximum B_1. The minimum B_1 is at the sides of the head, as shown, and is 39.7% of the maximum B_1 in this theoretical model. This slab is located approximately 8 cm below the top of the head. Acknowledgement to C. M. Collins[4] for providing the data.

Cylindrical birdcage coils consist of conductors arranged as two parallel circles, with several conducting rungs (long connections) in between them. The rungs are in close proximity with the sample and when transmitting, the RF amplifier runs alternating currents through them. From the rungs, electromagnetic waves pass through air and enter

the sample, therein causing MR excitation of the spins. The electromagnetic waves will eventually have a component that leaves the sample, as well as reflecting components at the boundaries. The various electromagnetic waves from each rung will sum up constructively or negate each other destructively with some predictable distribution within the sample. As the static field strength increases, destructive interference effects will increase within the sample, with some areas affected more than others. This is directly related to the fact that a higher magnetic field strength requires a higher frequency of current to excite the spins within the sample, because the frequency of current must be equal to the Larmor frequency. The correspondingly higher frequency magnetic waves that are created by the current flowing through the coil rungs have a shorter radiation wavelength. As well, due to the electrical properties of the human head, electromagnetic waves are shortened considerably as they cross the dielectric boundary from air to tissue. If the free-space wavelength of an electromagnetic wave is λ_o, and it passes through a medium with conductive properties known as the relative permeability μ_r and relative permittivity ϵ_r, then the wavelength is shortened:

$$\lambda = \frac{\lambda_o}{\sqrt{\mu_r \epsilon_r}} \qquad (3.1)$$

Thus, at 4.7 T, the wavelengths inside the tissue medium will become on the order of the dimensions of the head, approximately 20 cm at 200 MHz. Wave superposition effects due to the shorter wavelengths cause the B_1 power to be distributed more nonuniformly at 4.7 T. At lower fields, the longer wavelengths cause waves from each birdcage rung to sum up constructively with nearly identical phase across the head. At higher fields the rungs produce waves that interfere destructively with different phases throughout the head, with the waves crossing the central region having similar phase and thus the highest B_1 amplitude due to constructive interference.

B_1 amplitude values are usually expressed as a frequency:

$$\nu_1 = \frac{\gamma}{2\pi} B_1 \qquad (3.2)$$

With a birdcage coil, the hotspot (point of maximum B_1) in the brain at 4.7 T is located in the posterior corpus callosum and has a value of approximately 680 Hz[5]. The B_1 amplitude drops down to approximately 360 Hz at the sides of the head. Not only is B_1 inhomogeneity present across the transverse plane of the head, but also across the posterior-inferior direction. Part of the effect can be explained by the reciprocity theorem, which states that the fields of both the receiver and excitation coils affect the acquired signal, and for gradient echo acquisitions the signal varies as follows:

$$\text{Signal} \propto B_{1\text{receive}}(r) \cdot \sin\left[B_{1\text{excitation}}(r)\right] \qquad (3.3)$$

Attempts have been made in the literature to mitigate destructive interference effects with novel coil design. However, even with specialized high field coils, it is extremely difficult to obtain a B_1 transmission field with reasonable uniformity over large parts of the brain.

In imaging, this effect creates spatially varying contrast profiles across the head; in angiography, blood travels across a flip angle gradient, and background suppression is nonuniform. One solution lies in the optimization of pulse sequence parameters for insensitivity to RF inhomogeneity. This approach is investigated here.

3.2.2 Specific Absorption Ratio

Power deposition must be taken into consideration, especially with birdcage transmit coils at 4.7 T and higher, where more power is required to obtain a specific flip angle as

compared with lower field strengths[6]. The pulse sequences in this work used birdcage coils for transmission of RF power and were carefully designed to be within standard specific absorption ratio (SAR) safety guidelines[7] as specified by the US Food and Drug Administration (FDA) for the head:

Table 3.1 SAR limits specified by the FDA for MRI of the head.

Site	Dose	Time (min) equal to or greater than:	SAR Limit (W/kg)
head	averaged over the head	10	3
head or torso	per gram of tissue	5	8

SAR averaged over total sequence duration was consistently below 3 W/kg for all pulse sequences that were run on humans, averaged over the head and assuming a head mass of 3 kg. SAR averaged over a short time period (ten seconds) remained below 3 W/kg in almost all situations. Note that 4.7 T, a SAR of up to 3.3 W/kg averaged over approximately 12 minutes[8] has been safely used with birdcage coil transmission.

In point of fact, SAR may not be as important as actual temperature is. Indeed, maps of the spatial distribution of the rates of change of temperature in the brain during pulse sequences look completely different than SAR maps. This is partly due to the vascularity of the brain, which efficiently transfers heat throughout the head via the capillary network. The rate of change of temperature can be a useful measure of tissue heating. One of the most important measures of sequence safety, however, is the absolute temperature of the irradiated tissue. As field strength increases, it becomes increasingly important to know the spatial distribution of the absolute temperature across the entire sample as pulse sequences run. This is not something that can be accurately measured with high resolution using current MRI pulse sequence technology. A different avenue explored recently has been the insertion of temperature probes into animal (pig) brains, with the absolute temperature distributions recorded over time during sequence runs. These measurements provide evidence that at high field, absolute temperature increases

more proportionately to B_1 power spatial distribution than SAR spatial distribution; a paper by a group in Minnesota describing this in detail at 9.4 T has yet to be released. Thus high field pulse sequence designers must be mindful that heating tends to takes place first in the centre of the brain, contrary to the spatial distribution of SAR.

3.2.3 Patient Considerations

At the next higher magnetic field strength used for whole-body imaging after 4.7 T, 7 T, it has been reported that it takes >5 minutes to load patients into the magnet, and an equivalent amount of time to remove them from it. This is due to the fact that movement in such high field strength causes uncomfortable side effects. The first human volunteers scanned at 9.4 T report many side effects during scans such as feelings of nausea, vertigo, warmth, cold, etc. This is in stark contrast to 4.7 T, where loading time of a volunteer does not take more than a score of seconds, and side effects are in general absent during the scan while the volunteer is stationary. Only in one case so far was it necessary to slow the loading of a volunteer into the magnet, as he was experiencing adverse dizziness. Some nausea has been experienced at 4.7 T, but only in cases where one continually enters and re-enters the magnetic field, within a relatively short time duration. This is not something that ordinary volunteers have to do.

Taking account of the combination of the volunteer loading and unloading time at 7 T (approximately 10 minutes), and the fact that for research studies a given clinical structural scan should only last 12-13 minutes[9] to allow time for functional scans, one sees that much scan time is wasted. Patients with severe symptoms may force scans to be even more time restricted. These considerations indicate that field strengths higher than 4.7 T may never be as convenient and patient-friendly as 4.7 T.

3.3 Methods

3.3.1 RF Inhomogeneity Compensation

At 1.5 T, images in general have spatially uniform signal intensity, for a given tissue class. This is the ideal case. In contrast, with high fields such as 4.7 T, a given tissue class will display large spatial variations in signal intensity, due to destructive interference effects[10]. Thus, a signal intensity profile of, say, WM at 4.7 T will not be flat across the brain, as it would be at 1.5 T.

A common technique to reduce the visual effect of nonuniformities at high field strengths is to use image postprocessing. Intensities can be corrected by this postprocessing such that signal profiles appear uniform across the brain. However, if images are corrected in this manner, tissue contrast will still vary spatially across images, due to flip angle nonuniformities[11]. Instead, if, at the pulse sequence level, one can mitigate B_1 inhomogeneity, it should be possible to achieve both a spatially uniform signal intensity profile, as well as a spatially uniform contrast profile, across the whole image. In turn, this would facilitate much simpler separation of tissues into their respective classes (ie. WM, GM, CSF) by tissue segmentation software.

One solution to these problems is the creation of specialized composite pulses[12] to compensate for RF destructive interference by distributing more power in certain areas as compared with conventional pulses. Another pulse-based approach would seek to utilize adiabatic excitation pulses such as BIR-4 with a FLASH-type sequence. However, the power and time requirements of a BIR-4 are prohibitive for this purpose.

Due to reciprocity, the receive sensitivity of high field coils will be just as inhomogeneous as the B_1 transmit sensitivity. This means that, even if a pulse sequence were able to create a perfectly homogeneous B_1 field, the resulting images would still retain some residual spatial signal intensity variations. The receive sensitivity profile cannot be corrected at the pulse sequence stage. It can, however, be addressed by image postprocessing.

Another technique to correct intensity nonuniformities is to build specialized high field coils designed to provide as homogeneous a B_1 distribution as possible. In practice, these coils are not perfect, and some degree of B_1 nonuniformity is always present, as demonstrated by recent images obtained by Vaughn, et al., with advanced coils at 9.4 T (paper yet to be published). Thus it is anticipated that a sequence-based method which accounts for B_1 inhomogeneity will be advantageous when used in conjunction with the new high field coils.

3.3.2 Magnetization-Prepared Gradient Echo Pulse Sequences

The preparation pulses of the sequences shown in Figure 3.2 modify the state of the magnetization to provide improved contrast compared to steady state methods like spoiled FLASH. The magnetization is given some recovery time, which allows a higher signal to be produced. By carefully timing the sequence, background suppression for angiography can be improved. Alternatively, WM-GM contrast for imaging can be optimized. With centric acquisition of k-space data, signal and contrast is preserved. These sequences are common, and in particular the sequence of Figure 3.2c is a current clinical standard for structural imaging of the brain. This is the magnetization-prepared rapid gradient echo pulse sequence, MP-RAGE[13]. Figure 3.2d's pulse sequence is called modified driven equilibrium Fourier Transform, or MDEFT[14]. The MDEFT sequence was introduced for proton spectroscopy as a modification to the DEFT sequence in

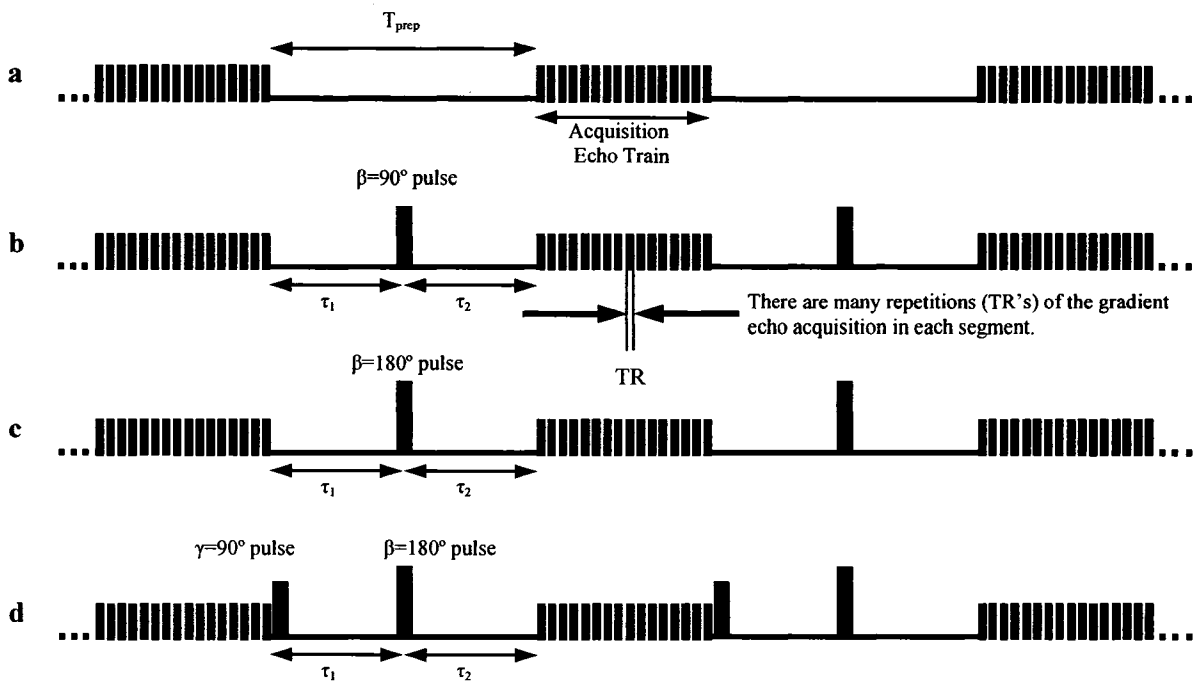

Figure 3.2 Pulse sequence timing diagram for a T_1-weighted, 3D gradient-echo sequence with four variations of magnetization preparation. Each preparation period T_{prep} comprises an RF pulse with a flip angle of γ degrees, followed by a recovery period τ_1, followed by a pulse with a flip angle of β degrees, followed by a magnetization recovery period τ_2, all prior to the acquisition segment. (a) γ = β = 0° (no preparation) (b) γ = 0°, β = 90° (c) γ = 0°, β = 180° (MP-RAGE) (d) γ = 90°, β = 180° (MDEFT).

1980[15], and has proved to have utility for providing good imaging contrast at field strengths as low as 1 T[16].

The four variations of MP segmented 3D gradient-echo pulse sequences in Figure 3.2 were implemented at 4.7 T. Each magnetization preparation period consists of two RF preparation pulses of flip angle γ and β which are separated by some relaxation time, τ_1, and followed by a period τ_2, which is an inversion recovery time (TI) when β = 180°. RF spoiling[17] and constant gradient spoiling was used to remove the unnecessary transverse magnetization following acquisition of each gradient echo. It should be kept in mind that all the preparation pulses, regardless of type, have spoiler gradients located immediately

after them. No refocusing gradient pulses whatsoever are used for them, even for those that require slice selection, because only the longitudinal magnetization is needed, and the remnant transverse magnetization is discarded.

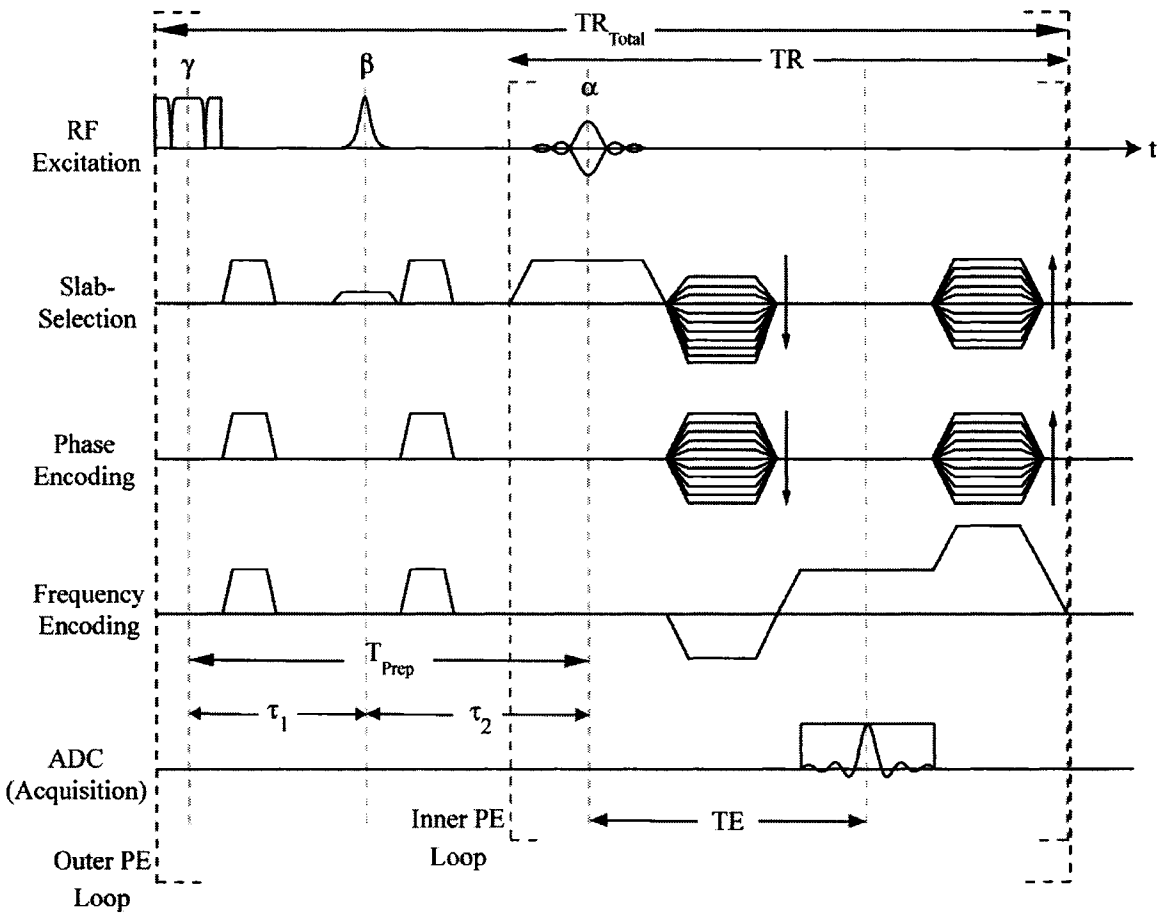

Figure 3.3 3D MDEFT pulse sequence timing in detail (not to scale). The γ, β, and α pulses are set to a constant flip angle. The entire outer PE loop within the time TR_{total} is repeated to fill k-space. T_{prep} comprises half of the γ preparation pulse, a delay τ_1, the β preparation pulse, and another delay τ_2, which runs up to the centre of the first α pulse. Each preparation pulse is followed by spoiler gradients. Each may optionally have a slab selection gradient applied simultaneously, as shown for the second pulse. Subsequent to the preparation are many gradient echo acquisitions, indicated by the inner PE loop. Data readout is indicated by the analog-to-digital converter (ADC) signal.

T_{prep} is the total amount of preparation time; that is, it is the time between the two preparation pulses. For simulations, the duration of all pulses was neglected, including the gradient echo excitation pulses. For experiments, the exact simulation timings were applied as shown in the detailed pulse sequence diagram, Figure 3.3. In the case of MP-RAGE, which only has a single pulse, T_{prep} is the total time before and after the pulse.

$$T_{prep} = \tau_1 + \tau_2 \qquad (3.4)$$

The relative positions of the two preparation pulses are described by the quotient of τ_1 and T_{prep}, sometimes simply referred to as "quotient" in the literature:

$$\text{quotient} = \tau_1/T_{prep} \qquad (3.5)$$

Given some initial longitudinal magnetization M_z^-, the magnetization following T_{prep} can be easily calculated as follows:

$$M_z(T_{prep}) = M_0 \cdot (1-(1-b)\cdot e^{-\left(\frac{\tau_2}{T_1}\right)}) + b(-M_0 + M_z^- a)\cdot e^{-\left(\frac{T_{prep}}{T_1}\right)} \qquad (3.6)$$

where $a = \cos(\gamma)$ and $b = \cos(\beta)$. The magnetization following acquisition of each view can be calculated iteratively to produce the next M_z immediately subsequent to an excitation RF pulse, $M_z(TR^+)$:

$$M_z(TR^+) = M_0 + (M_z(TR^-)\cdot\cos(\alpha) - M_0)\cdot e^{-\left(\frac{TR}{T_1}\right)} \qquad (3.7)$$

where α is the RF excitation pulse flip angle, and $M_z(TR^-)$ is the value of M_z after the last TR period finishes. Given the steady state FLASH value of M_z, which was derived previously, $M_{z,ss} = M_o\,(1 - e^{-\left(\frac{TR}{T_1}\right)})/(1 - \cos(\alpha)e^{-\left(\frac{TR}{T_1}\right)})$, one can calculate the final value of the longitudinal magnetization just following the last RF pulse of a train of n echoes[18]:

$$M_{z,final} = M_0 \cdot \left(M_{z,ss} - \left(-\frac{M_z(T_{prep})}{M_0} + M_{z,ss} \right) \cdot \left(\cos(\alpha) e^{-\left(\frac{TR}{T_1}\right)} \right)^n \right) \qquad (3.8)$$

where $M_z(T_{prep})$ is the magnetization immediately following T_{prep}. Use of this equation greatly accelerates simulations.

Any comparison between MP-RAGE and MDEFT must necessarily consider the differing contrast and signal available with each of the sequences due to the different possible timings of the preparation pulses, given the same T_{prep}. For a proper comparison, it is necessary that the total sequence time remains constant. Simulations were performed for MP-RAGE and MDEFT for different objectives, i.e. maximum WM and GM signal difference to noise ratio (CNR), maximum uniformity, and the best compromise between CNR and uniformity. Ideally one might also like the CSF suppressed to a higher level, depending on the application. Parameter values were optimized for these imaging objectives, while still constraining the transient signal modulation transfer function (MTF) of the tissues of interest to provide sufficient signal such that even small tissue compartments should be distinguishable. Centric phase encoding was also used to improve contrast.

3.3.3 High Field Power Calibration

Power calibration is a process by which the amount of power delivered to the sample is calibrated such that the flip angle is known for a given pulse shape, power, and duration. One method of power calibration involves a simple slice-selective pulse followed by acquisition of a profile of the sample. Many acquisitions occur, with some time between each acquisition to allow for recovery of the sample magnetization. All parameters are kept constant, except for power, which gradually increases by a small amount for each subsequent pulse. The highest peak observed corresponds to the pulse imparting a 90° flip angle to the sample, as described by the Bloch equations. Using the known 90° power level and the pulse parameters, one can determine the required power level to obtain any tip angle for many other pulse types.

When a hard excitation pulse is applied at low field, all the tissue is excited such that power is distributed approximately equally. That is, ideally, 100% of the B_1 magnetization strength is applied to all tissue elements throughout the spatial extent of the sample. The situation encountered in modern high field systems is different: for a transmit birdcage coil applying a given B_1 strength, instead, due to destructive interference effects, a range of B_1 strengths will be experienced by the sample. In point of fact, B_1 contours are distributed at 4.7 T similar to rings, when viewing transverse sections of the brain. For example, when imaging a slice and applying a 90° hard pulse at some point inside the brain, flip angles will be produced equal to 90° along a certain constant B_1 contour, and outside this contour the flip angles produced will be greater than and less than 90°. Thus, the best that can be done at high field for hard pulses is to calibrate power such that the average flip angle across the head is known. This power level is labelled "100% B_1 strength", sometimes called the nominal power level. It is known that flip angles in the head at 4.7 T will be within a certain well-defined range, usually from 50 to 150% of nominal B_1 strength, with birdcage-type and transverse electromagnetic (TEM) volume transmit coils.

Results will vary greatly, depending on if one chooses to calibrate power such that the specified flip angle occurs at the centre of the head, sides of the head, or is averaged across the head (nominal). Furthermore, the power required for a given flip angle may be different if one chooses to calibrate power using a profile of a large slab instead of a localized slice. Destructive interference causes a greater concentration of power to reach the centre of the human brain as compared with the sides, and thus it requires relatively less power to obtain a specific flip angle at the centre of the head as opposed to the sides. At 4.7 T, a 180° flip angle at the sides of the head requires roughly 6 dB more power than the centre. However, even if the transmission effect is corrected by some method, the reciprocal receive sensitivity of a Transmit-only Receive-only (TORO) birdcage coil means that the signal intensity at the sides of the head will be lower than the centre in most cases.

Furthermore, the RF amplifiers are not perfectly linear, and as such a 6 dB increase from a power level of 57 dB to 63 dB may actually be closer to 8 dB in the hardware RF chain. This further complicates obtaining exact flip angles. Linearity of the amplifiers decreases further at the highest power levels available, which are unfortunately the levels at which most in-vivo work is performed. A workaround to this is to use the spectrometer software to specify different flip angles not with the use of the fine or coarse attenuators, but instead by changing the RF pulse. That is, the fine and coarse attenuators can be set to one setting, and the RF flip angle changed by simply varying the height of the RF pulse profiles.

Another power calibration consideration is the effect of B_1 inhomogeneity upon thin slice profiles. Suppose one is using slice profiles through the central, highest B_1 amplitude portion of a sample. To find the 90° flip angle, the power is gradually incremented, and successive profiles are acquired. One must be aware of the fact that the peak profile does not exactly determine the 90° flip angle for all parts of the sample. This is because, within a given slice, there are usually parts of the sample on either side of the part with

the maximum B_1 amplitude which have lower B_1 amplitude. Thus, the maximum B_1 profile could occur for example when the centre of the sample is at 85° and the sides are at 80°. As power gradually increases, if the centre reaches 95°, the sides may reach 90°, and both 90° sides become summed when forming the profile. The result could well appear to be the highest profile, which would then be erroneously considered by the automated software as the true 90° for all points within the sample. Considering that the coil receive sensitivity has a similar profile shape to that of the transmission sensitivity due to reciprocity, this effect is mitigated somewhat so that using profiles provides a reasonable, but still somewhat inaccurate, approximation when power calibrating.

One workaround to this is to use a voxel-selective pulse sequence such as point resolved spectroscopy (PRESS) to measure signal only from a small part of a sample, say 10x10x10 mm. In this manner, the exact 90° flip angle can be determined with a high precision, for a small voxel with a relatively uniform B_1 profile. Using this point as a reference, and assuming the relative B_1 distribution throughout the rest of the sample is known, the average flip angle across the head can be set. If PRESS is used, enough TR time must be allowed between acquisitions of spectra for full T_1 recovery, otherwise power calibration accuracy is sacrificed. In-vivo, a TR of approximately 3 seconds gives a good approximate power calibration result. For in-vivo best results, 15 seconds is ideal.

3.3.4 Effects of Preparation Pulses on Image Homogeneity

Birdcage and transverse electromagnetic (TEM) volume coils have an inherently large degree of B_1 transmit inhomogeneity at high static field strength. The MDEFT pulse sequence can be tailored to mitigate this, mainly by modifying one or both of its magnetization preparation pulses. Attempts to do this in-vivo with MDEFT, in whole-body magnets greater than 3 T, date back to 1994[19]. More recently, B_1 inhomogeneity effects have been minimized by replacing the 180° adiabatic inversion pulse historically used for MDEFT with a lower flip angle hard pulse[20]. In order to understand how this is

possible, three variations of the magnetization preparation pulses were examined (Figure 3.4, Figure 3.5, and Figure 3.6). For each situation, the gradient echo (GRE) excitation pulse flip angle is varied over a range from 50 to 150% of the nominal flip angle, as shown in the figures, and the effect on the signal intensity of different tissues was investigated through simulation. The flip angle of the excitation pulse is proportional to the magnitude of the B_1 field. In addition, these plots show transverse magnetization; that is, the sine dependence of the excitation flip angle is factored into the signal equation, just as what occurs in actual images.

It is important to note here as well that the sequence employs centric encoding. That is, the signal intensity of a given tissue is determined by the central views of k-space. By encoding spatial information about the central views first in echo trains, more information from the preceding magnetization preparation is preserved. This encoding scheme enables superior contrast and signal intensity levels compared to linear encoding schemes.

In Figure 3.4, the MDEFT magnetization preparation consists of a two adiabatic pulses, each followed by some time delay. Note that adiabatic pulses bring about the same flip angle throughout their area of application; that is, they are B_1-insenstive, so that 100% of the flip angle is applied to all tissue within a large spatial extent. To put it another way, as the excitation flip angle varies from 50 to 150%, as in Figure 3.4, adiabatic pulse flip angles remain constant at 100% of their specified value. The 90° adiabatic BIR-4 global saturation pulse[21] nulls the longitudinal magnetization, and its subsequent spoiling gradients null the transverse magnetization. After a delay, a standard 180° adiabatic hyperbolic secant[22] inversion pulse is used, followed by more spoilers and another delay. In practice, 100% inversion of the longitudinal magnetization is not possible with this type of adiabatic pulse, but 95-98% is. To all intents and purposes, the two adiabatic preparation pulses are insensitive to B_1. The RF excitation pulse, on the other hand, is very sensitive to B_1: it is proportional to the applied B_1, and thus directly affects the overall signal intensity as B_1 changes, which shows up clearly in the figure.

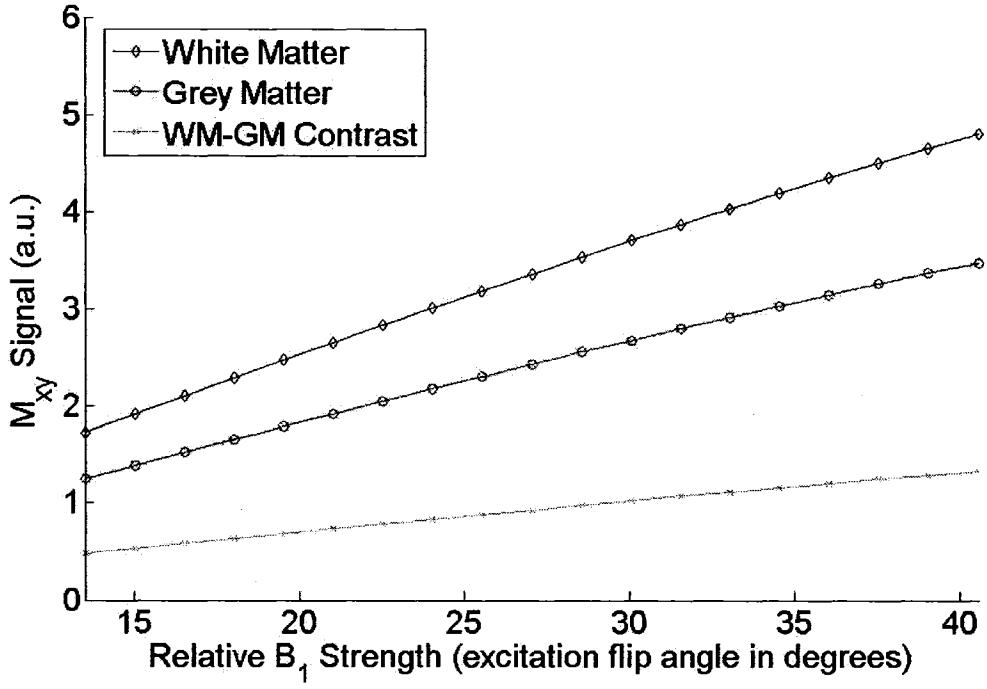

Figure 3.4 Simulation of an MDEFT sequence that uses first a 90° adiabatic magnetization preparation pulse, followed by a 180° adiabatic *preparation pulse*[23]*. The efficiency of the inversion is essentially immune to B_1 changes due to the adiabaticity of the inversion pulse. Thus, the relative signal seen is proportional to the RF excitation flip angle. τ_1/T_{prep} = 0.45, τ_2 = 314.6 ms and mean flip angle = 27.5°. The vertical axis has arbitrary units.*

In Figure 3.5, the MDEFT sequence is identical to the previous case, with the exception that a hard inversion pulse replaces the adiabatic inversion pulse. The hard inversion pulse has a mean flip angle of 180°; that is, where the excitation pulse has its nominal flip angle, the hard inversion pulse has a flip angle of 180°:

$$\text{GRE excitation pulse flip angle} \propto \text{Hard inversion pulse flip angle} \qquad (3.9)$$

When the B_1 field amplitude is less than its average value, the excitation pulse flip angle is lower, and this contributes to a lower tissue signal intensity. However, the flip angle of the second preparation pulse will also be lower, because it is a hard pulse with an average flip angle of 180°. This reduced inversion efficiency means that the longitudinal magnetization will be higher after the magnetization preparation period ends. In turn, this contributes to a higher signal intensity. So by using a hard pulse, decreasing B_1 amplitude is compensated, so that signal levels for lower B_1 remain nearly the same as at 100% B_1.

When the B_1 field strength is greater than the average value across the head, as is the case in the centre of the brain at high field with birdcage-type and TEM volume coils, the signal intensity in the final image is brighter. This is due to the fact that with the centric T_1-weighted gradient echo sequence used here, the higher RF excitation flip angles that are present lead to higher signal. In addition, this effect is compounded by the decreased inversion efficiency of the 180° hard pulse: at B_1 strengths higher than average, the hard pulse flip angle is >180°. Looking at the effect on magnetization of a flip angle of >180°, with the classical vector model of MR, one sees that the final magnetization is actually less than that of the nominal 180°. So again, when the preparation pulse is over, signal intensity will be higher than average, and so the hard inversion pulse plays a role in increasing signal intensity because there is more magnetization available when the acquisition echo train begins. In effect, we have *increased* B_1 sensitivity of the sequence, for high B_1 values.

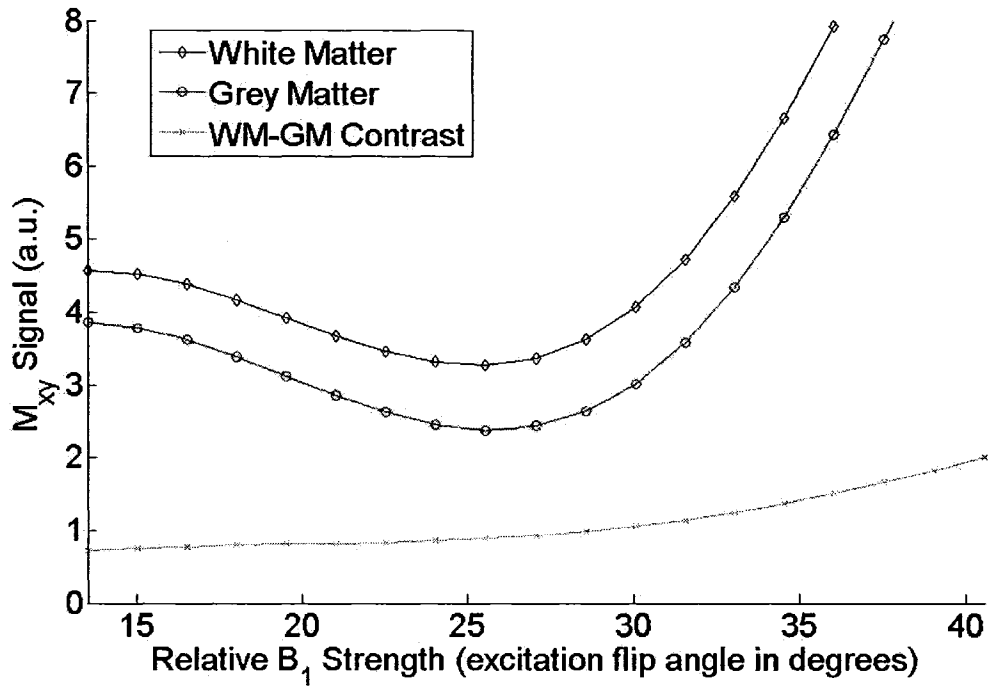

Figure 3.5 Simulation of an MDEFT sequence that uses first a 90° adiabatic magnetization preparation pulse, followed by a 180° hard *preparation pulse[23]. The second preparation pulse flip angle linearly increases across the graph, and is 180° in the centre. When this preparation pulse is less than 180° (on the left half of the graph), its increase in flip angle with B_1 causes a reduction of longitudinal magnetization with B_1, opposed by the linearly increasing excitation flip angle. As the preparation increases over 180°, the inversion is less complete and so more magnetization is available, increasing signal. $\tau_1/T_{prep} = 0.45$, $\tau_2 = 314.6$ ms and mean flip angle = 27.5°.*

In Figure 3.6, the situation is the same as the previous two cases, except for the fact that a 125° hard pulse replaces the inversion pulse. Again, this flip angle is assumed to be the average across the head, and the excitation flip angle is proportional to it. For Figure 3.6, when the B_1 field amplitude is lower than its average value, the situation is quite similar as the previous figure. Lower B_1 translates to lower T_1-weighted signal intensity for WM and GM, due to lower RF excitation flip angle. Additionally, the lower B_1 causes the flip

angle of the hard pulse to be lower than 125°. The consequence of the reduced inversion efficiency is a higher remnant magnetization and hence signal level.

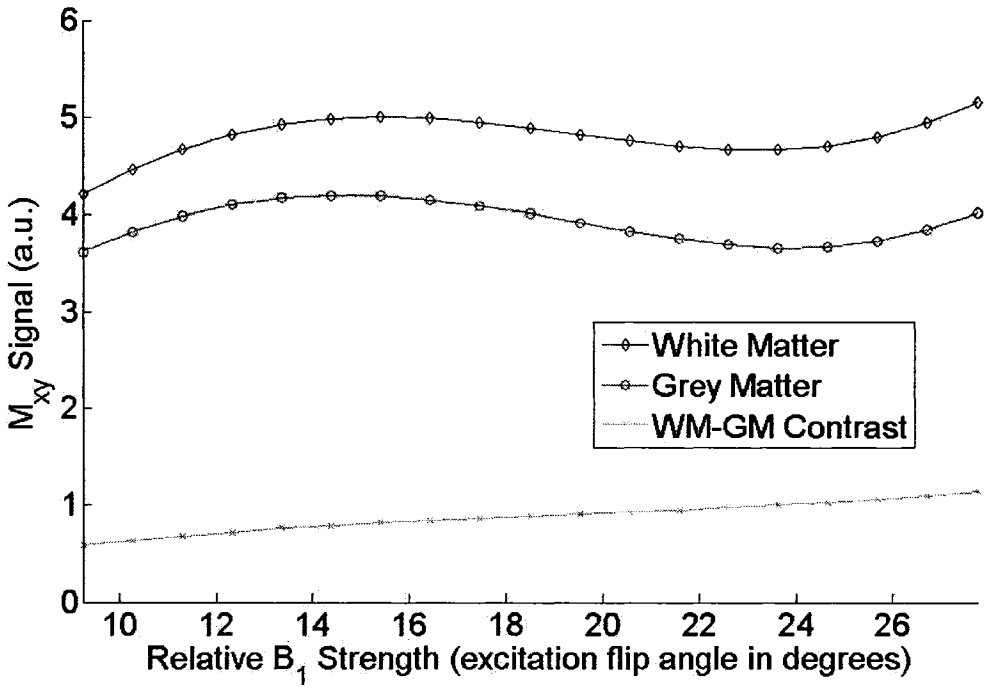

Figure 3.6 Simulation of an MDEFT sequence which uses first a 90° adiabatic magnetization preparation pulse, followed by a 125° hard *preparation pulse*[23]*. The second preparation pulse flip angle linearly increases across the graph, and is 125° in the centre. As the preparation pulse flip angle increases with B_1, the longitudinal magnetization decreases, compensating the excitation flip angle's proportionality to B_1. τ_1/T_{prep} = 0.39, τ_2 = 348.9 ms and the excitation flip angle = 18.5°. τ_1/T_{prep}, τ_2 and the excitation flip angle are different from the two previous figures because it provides better WM/GM/CSF signal intensity for small tissue compartments, given this choice of magnetization preparation. Similarly shaped profiles would result if the excitation flip angle and τ_1/T_{prep} were the same as in the previous two figures.*

The difference in Figure 3.6 from previously considered cases occurs when the B_1 field amplitude is higher than its average value in the sample. The excitation flip angle continues to increase with the B_1 field as before. However, with a flip angle greater than

125° and still less than 180°, the hard preparation pulse has a low inversion efficiency compared to a true inversion pulse. The hard pulse magnetization preparation will continually reduce the signal level as the B_1 amplitude increases. The net effect of the two competing pulses is to mitigate the effect of the field homogeneity by maintaining the overall signal levels at a reasonably consistent level. One can see from the figure that this B_1 compensation effect causes the contrast profile to be quite flat across the whole B_1 range. Ordidge, et al.,[23] pioneered this basis of MDEFT nonuniformity compensation at high field. It turns out that an average of 125° is the optimal value of the second inversion pulse, resulting in signal profiles that are the flattest possible for WM and GM imaging at 4.7 T, given the assumption of certain values of the other pulse sequence parameters.

3.3.5 Selection of the Excitation Pulse Flip Angle

In brain imaging, there may be situations where a single pixel of tissue is surrounded by another tissue type. The surrounding tissue class will modify the pixel signal intensity. Dependent upon the signal intensity of the surrounding region, the enveloped tissue may not be bright enough to be distinguished by tissue classification programs such as Statistical Parametric Mapping (SPM2[24]). The point spread function (PSF) and its Fourier Transform, the modulation transfer function (MTF) have already been discussed. MTF falloff is produced by FLASH gradient echo trains, and the result is a widening of the PSF width. This means that pixels will be blurred instead of ideal delta functions, with image energy spread across adjacent pixels. Such blurring noticeably occurs at tissue boundaries. Careful selection of the excitation pulse flip angles, taking into account the modification of the PSF width by a large surrounding region of another tissue class, can ensure that small tissue region information is not lost[25]. The tools necessary to accomplish this require the calculation of the signal intensity of large as well as small tissue spaces.

Consider for example a centric FLASH sequence with a relatively low flip angle. The transient signal evolves over time, such that the final image data will be modulated by the

k-space MTF. For a large homogeneous region, the image intensity is proportional to the central value of the k-space MTF. This applies not only for a simple, centric FLASH acquisition, but also in the case where k-space data is centrically reconstructed such that central k-space comprises multiple adjacent, identical values. Such a result can be readily demonstrated by simulation. First an artificial, large region with uniform and unity intensity is Fourier transformed to yield its k-space equivalent, which resembles a delta function. The k-space data may be spatially shifted as necessary at this point. Then, the MTF data can be applied by multiplication, in which case the final result would need to be inverse Fourier transformed and shifted, and the absolute value taken. Equivalently the MTF can be applied by convolving its PSF with the image data. Both approaches are standard, and lead to the identical result – the large region's pixels take on the central MTF value.

Deichmann[25] proposed to use the integral of the PSF, that is, the sum of all its points, as a measure of the signal intensity of large uniform regions. For these homogeneous regions, the integral of the PSF is not always proportional to the signal intensity, whereas the centre of the MTF is. One common example where this applies is the case of an MTF where more than one central value is identical. The centre of the MTF was used for the signal intensity value of large regions.

A measure of the signal intensity of small areas (1 pixel or less) is also necessary. If an artificial image has only a single pixel with a unity value, the application of an MTF will cause the pixel's value to change to be equal to the maximum amplitude of the PSF corresponding to the MTF. The maximum PSF amplitude was used for the signal intensity value of small regions.

The calculation of the PSF by Fourier Transform is slow. In the case of noncyclic MTF's with perfect symmetry about the central axis, the corresponding PSF's will have a single maximum point at the centre. Prior to the final shift operation which exchanges the two PSF halves, the PSF peak will be located at the leftmost point in the data points. Thus a

tremendous decrease in processing time can be afforded because one can simply limit calculation to the first point of the PSF, if only the maximum amplitude is needed. If the PSF is given by:

$$x(n) = \text{Fourier transform } \{X(k)\}$$

$$x(n) = \sum_{k=1}^{N} (1/N)X(k)*\exp(j*2*\pi*(k-1)*(n-1)/N) , 1 <= n <= N \qquad (3.10)$$

where x(n) is the n'th point of the PSF, X(k) is the k'th point of the MTF, N is the number of data points, then the intensity of a small area of 1 pixel is given by:

$$x(1) = \sum_{k=1}^{N} (1/N) \qquad (3.11)$$

where x(1) is the first point of the PSF, the maximum amplitude (before shifting). x(1) is real, so the absolute value does not need to be calculated.

With many techniques that use flip angles greater than 90°, it is possible for longitudinal magnetization to take on any value between $-M_o$ and M_o inclusive[26]. In practice one needs to be mindful of tissue magnetization magnitudes that are very close to zero. If a tissue's MTF crosses zero, and the PSF is calculated by taking the absolute value, then the PSF will consist of multiple peaks. In this case, the maximum value of the PSF will no longer be centred, and this speed optimization cannot be performed. Such a situation can be avoided if signal values near zero are not considered. Phase-sensitive real reconstruction could also be performed to avoid this problem, although it was not used because it requires specialized phase correction methods[27,28,29,30].

A small area of one tissue type will have its signal intensity modified by several things. These include the small area's PSF width, and the PSF width and signal intensity of a

larger surrounding tissue region. Consider a unit area pixel consisting solely of GM. If a large area of WM with uniform intensity encompasses it, then the signal intensity of the GM area is:

$$S(\text{GM in WM}) = I_W + A_G - A_W \qquad (3.12)$$

where I_W = signal intensity of a large region of WM, and A_G and A_W are the signal intensities of small GM and WM regions, respectively. This is equivalent conceptually to removing a unit area of white matter from a large white matter region, and filling the resultant hole with grey matter. Similarly, the signal intensities for other situations can be calculated as follows, where I_G and I_C are the signal intensities of large regions of GM and CSF, and A_C is the signal intensity of a small CSF region:

$$S(\text{WM in GM}) = I_G + A_W - A_G \qquad (3.13)$$

$$S(\text{GM in CSF}) = I_C + A_G - A_C \qquad (3.14)$$

$$S(\text{CSF in GM}) = I_G + A_C - A_G \qquad (3.15)$$

Given these equations for the signal intensities of small tissue compartments surrounded by other tissues, it is possible to calculate limits that will allow proper classification of the compartments by automatic tissue segmentation programs[31]. Consider an image with a range of WM and GM signal intensities, with the restriction $I_W > I_G$. Tissue segmentation algorithms should classify WM and GM correctly if their intensities are above and below, respectively, their average intensity, $(I_W + I_G)/2$. There should also be some leeway, taking into consideration the standard deviation of noise, σ:

$$WM_{min} = (I_W + I_G)/2 + \delta(I_W - I_G) \quad (3.16)$$

$$GM_{max} = (I_W + I_G)/2 - \delta(I_W - I_G) \quad (3.17)$$

where

$$\delta(I_W - I_G) \geq \sigma, \delta < 1 \quad (3.18)$$

Given the knowledge that the measured SNR's of GM and WM are I_W/σ and I_G/σ, respectively, σ can be derived:

$$CNR = (I_W - I_G)/\sigma$$

$$\sigma = (I_W - I_G)/CNR \quad (3.19)$$

From the above equations we determine the following limit for δ:

$$\delta(I_W - I_G) \geq \sigma \rightarrow \delta(I_W - I_G) \geq (I_W - I_G)/CNR \rightarrow \delta \geq 1/CNR \quad (3.20)$$

An assumption must be made about the minimum CNR at this point, $CNR_{min} = 7$[31]. It turns out that this is a reasonable number in many cases at 4.7 T, but not all. At any rate, this leads to a minimum δ of:

$$\delta = 1/7 \cong 0.15 \quad (3.21)$$

This value can also be applied to calculate the remaining limits:

$$GM_{min} = (I_G + I_C)/2 + \delta(I_G - I_C) \quad (3.22)$$

$$CSF_{max} = (I_G + I_C)/2 - \delta(I_G - I_C) \quad (3.23)$$

Thus, when determining the excitation flip angle, one typically would check that the signal intensities of small compartments are within the limits, like so:

$$S(WM \text{ in } GM) > WM_{min} \quad (3.24)$$

$$S(GM \text{ in } WM) < GM_{max} \quad (3.25)$$

$$S(GM \text{ in } CSF) > GM_{min} \quad (3.26)$$

$$S(CSF \text{ in } GM) < CSF_{max} \quad (3.27)$$

One assumption is that the images are T_1 weighted, so that $I_W > I_G > I_C$. If this is not true, these equations will fail to provide the optimal excitation flip angle. This occurs in certain situations, such as when WM and GM signal intensities are less than zero and magnitude images are formed. This would not happen with real reconstruction[32].

It may also be desirable to lower the intensity of CSF beyond what the above equations specify. During the simulation, a check can be made of the CSF intensity, and if it is greater than 25% of GM, then the parameter set can optionally be discarded in favour of one with brighter relative GM intensity, or lower CSF intensity.

By following the above methodology for selection of the excitation flip angle, signal intensities will be strong enough for small areas of WM, GM, and CSF to be individually classified. This technique also requires that PSF widths be checked as a final step. Ideally, with a flat MTF, the PSF should be a delta function with unit width. In practice, as long as the PSF widths for different tissues are close to one, small tissue compartments should be identifiable. Even though the PSF is a discrete function here, it can be approximated with the FWHM, with a piece-wise linear interpolation between pixels as

needed. Another PSF approximation involves calculating the power spectrum of the PSF[33]; this was not used because it is a much slower calculation in practice. As well, the maximum intensity of PSF data values on either side of the absolute maximum data value should be small; sidebands in the PSF lead to ghosting. As an additional word of caution, changing δ even slightly from 0.15 can result in different excitation flip angles being calculated, which have a profound effect on the simulated CNR values.

3.3.6 Through-plane vs. In-plane Blur

It is possible to have the slice select direction as the MTF falloff direction during readout, as opposed to the phase encode direction. One reason for doing this is that through-plane blurring is not very noticeable, while in-plane blurring is. Also, blurring can be exaggerated if one uses a longer readout train during each segment (in order to reduce total imaging time). Usually the number of 3D phase encoding views is smaller than the number of 2D phase views. Thus, in order to alter the direction of blurring and use smaller echo train segments, the inner 2D phase encoding loop is swapped with the outer loop. From a 3d perspective the degree of blurring will be the same, just spread differently.

3.3.7 Soft vs. Hard Pulses

All of the above theory and experiment is equally valid if all of the hard preparation and excitation pulses are replaced with soft slice-selective pulses. If this is done, the only requirement for achieving B_1 compensation is that pulse types are not intermingled; that is, if there are hard pulses used for magnetization preparation, then the excitation pulse should also be a hard pulse. If the excitation is a sinc pulse (which is a soft slice-selective pulse), then any non-adiabatic magnetization preparation pulses must be exactly the same slice-selective pulse shape, sinc. They must also be the same thickness.

3.4 Contrast-to-Uniformity Ratio Optimization

3.4.1 Introduction to CUR

High field destructive interference effects are the reason for the nonuniformity in MDEFT and MP-RAGE images. Some metric is required to measure the efficacy of any attempt to compensate image nonuniformity. Furthermore, white matter (WM) to grey matter (WM) contrast is important for structural brain imaging. The Contrast-to-Uniformity (CUR) ratio[23] provides a measure of the contrast and uniformity of an image:

$$\text{CUR} = \frac{(\text{WM SNR}) - (\text{GM SNR})}{\text{Average of the standard deviations of WM and GM SNR}} \qquad (3.28)$$

The numerator provides a measure of the WM and GM contrast; the denominator, uniformity. The contrast is usually calculated for 100% B_1 strength only[11], that is, the average value across the head that the flip angles are calibrated to. The standard deviations are calculated over a range of B_1 strengths, usually from 50% to 150%.

The higher the CUR, the better the contrast, and the better the uniformity. Note that by incorporating the standard deviations of both WM and GM signal intensity, one gets a simultaneous measure of the homogeneity of the signal profiles of both WM and GM. That is, it is actually a measure of the contrast uniformity, so that the lower the denominator, the flatter the contrast profile across the head. A denominator of zero indicates perfectly flat signal profiles, and hence a very large CUR.

Note that the CUR number is somewhat misleading, because a sequence combination that produces a low contrast in combination with a flat contrast profile can have the same

CUR as a sequence with high contrast and a relatively nonuniform contrast profile. Therefore, in addition to the CUR itself, its numerator and denominator should also always be kept in mind, so that the whole picture is known.

3.4.2 CUR Optimization

Several possible combinations of magnetization preparation pulses were investigated, such as adiabatic/adiabatic, adiabatic/soft, soft/adiabatic, soft/soft. For each given combination of preparation pulse types, the flip angles of the preparation pulses were cycled from 0° to 180° in steps of 10°, and the best CUR chosen was from all the possible flip angle combinations. For each chosen preparation pulse flip angle, an excitation pulse flip angle was chosen to ensure that small matter compartments would have sufficient SNR, using the methods described previously. This process was performed for each τ_1/T_{prep} value from 0 to 1, which corresponds to changing the position in time of the second preparation pulse from immediately after the first preparation pulse ($\tau_1/T_{prep} = 0$), to just before acquisition ($\tau_1/T_{prep} = 1$).

Thus, values of the best CUR and their corresponding preparation pulse combination were generated over the specified range of τ_1/T_{prep} values. From this list of CUR values, the maximum CUR can be easily selected. In the case of two preparation pulses, the first preparation pulse always occurs immediately after the preceding echo train acquisition. In the case of MP-RAGE, with only one preparation pulse, the pulse was allowed to freely vary throughout T_{prep}.

For 4.7 T simulations, T_1 values from the literature[20] were used: WM T_1 = 1.05 s, GM T_1 = 1.5 s, and CSF T_1 = 4.6 s, with the following spin densities: WM ρ = 0.65, GM ρ = 0.75, CSF ρ = 1.00. Another source[34] in the literature mentions WM T_1 = 1.07 s, GM T_1 = 1.63 s at 4.7 T, while another source[35] specifies the following 4 T values: WM T_1 = 1.043 s, GM T_1 = 1.724 s, CSF T_1 = 4 s, Blood T_1 = 2 s.

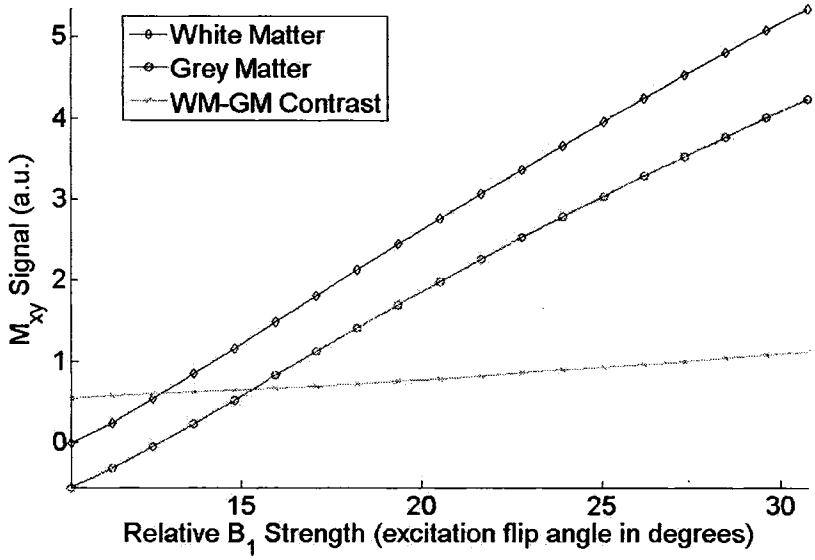

Figure 3.7 4.7 T simulation showing the MP-RAGE sequence with optimized CUR using a 180° adiabatic *preparation pulse.* τ_1/T_{prep} = *0.26,* τ_2 = *423.3 ms, and mean excitation flip angle = 20.5°.*

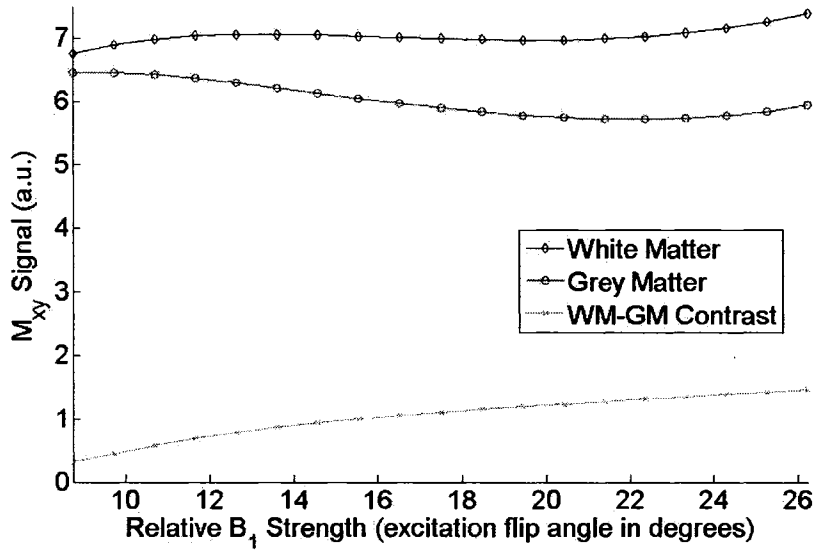

Figure 3.8 4.7 T simulation showing the MP-RAGE pulse sequence with optimized CUR using a 100° soft *preparation pulse. Note the marked improvement in uniformity and signal levels.* τ_1/T_{prep} = *0.23,* τ_2 = *440.4 ms, and mean excitation flip angle = 17.5°.*

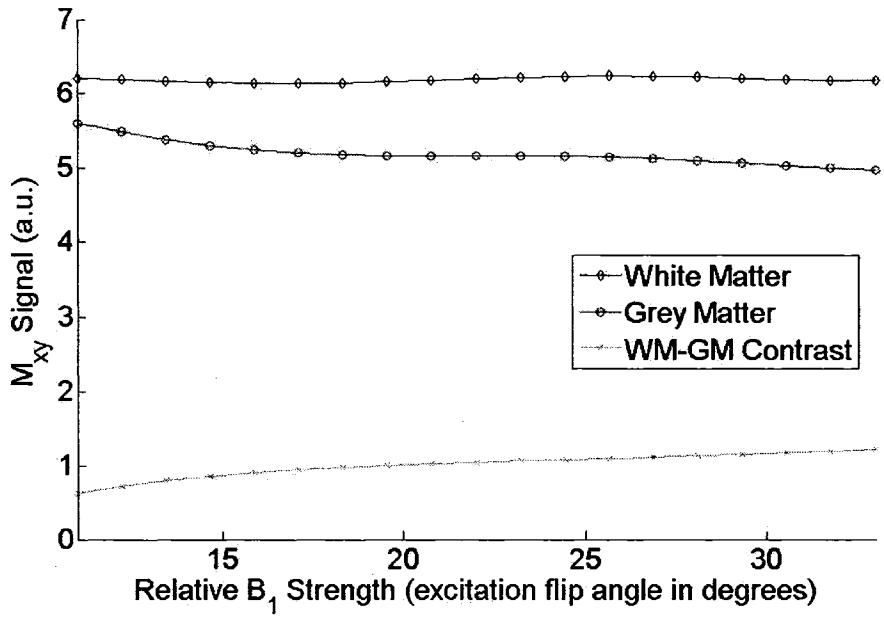

Figure 3.9 4.7 T simulation showing the MDEFT pulse sequence with optimized CUR using two 110° soft preparation pulses. τ_1/T_{prep} = 0.44, τ_2 = 320.3 ms, mean excitation flip angle = 22°. Notice the high signal and excellent uniformity over a range of B_1 strengths for the WM, GM, and contrast.

3.4.3 Optimized CUR Images

Consider the images in Figure 3.10 to Figure 3.12. For these scans, T_{prep} = 572 ms (constant). This is precisely the T_{prep} value that is used in the recent literature to explore CUR optimization[23], and holding it constant does in fact it does limit the attainable range of results, but it provides consistent timing. Also held constant were the TR at 13.1 ms, and TE at 5.89 ms, BW_{sam} = 37.506 kHz giving an acquisition time of 6.8256 ms for a 256x224 matrix size, symmetric echo, and a 2-D slice thickness of 5 mm. Segment size consisted of 112 phase views in addition to 8 dummy views without RF, and 6 dummy segments preceded each acquisition echo train. The dummy views were found to be necessary to reduce low SNR background ghosting along the phase encoding direction, likely caused by low amplitude eddy current transients. RF spoiling with a phase

increment of 117° was used in combination with gradient spoiling of 21 mT/m for 2ms. 15 ms, 58 dB 3rd order hyperbolic secant pulses were used for adiabatic inversion, while 15 ms, 58 dB BIR-4 pulses were used for the lower flip angle adiabatic pulses. Over 20 volunteer scans were performed for testing purposes.

All the images shown in Figure 3.10 to Figure 3.12 were acquired with identical receiver gain (40 dB) with a transmit/receive TEM head coil. For Figure 3.10, the window and level of each image, corresponding to contrast and brightness settings, were individually optimized to bring out the most detail. For Figure 3.11 and Figure 3.12, the window and level of each image were identical. This allows visual comparison of the different signal intensity levels and relative uniformity.

For each of the lettered images in Figure 3.10 to Figure 3.12, the corresponding sequence magnetization preparation and excitation pulse characteristics, and τ_I/T_{prep} timing value, are shown in Table 3.2.

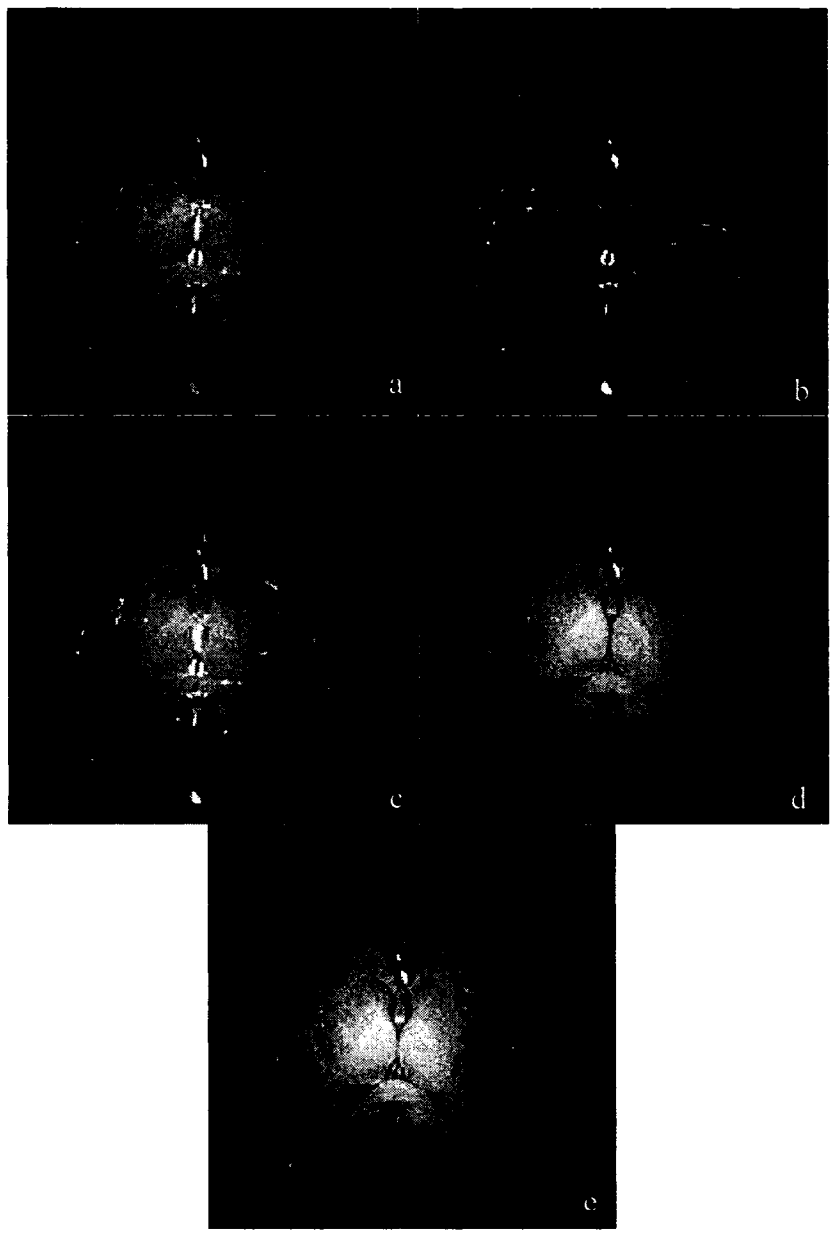

Figure 3.10 Axial 4.7 T 2-D images acquired with a TEM volume coil using identical receiver gain and individually optimized window and level. T_{prep} *= 572 ms, TR = 13.1ms, and TE = 5.9 ms in all cases. (a) MP-RAGE using a soft (slice-selective) preparation pulse with a flip angle of 100°. (b) MP-RAGE using a 180° adiabatic preparation. (c) MDEFT with two 110° soft preparation pulses. (d) MDEFT with 110° adiabatic and 125° soft preparation[23]. (e) MDEFT with 90° adiabatic and 125° soft preparation[23] (see Figure 3.6).*

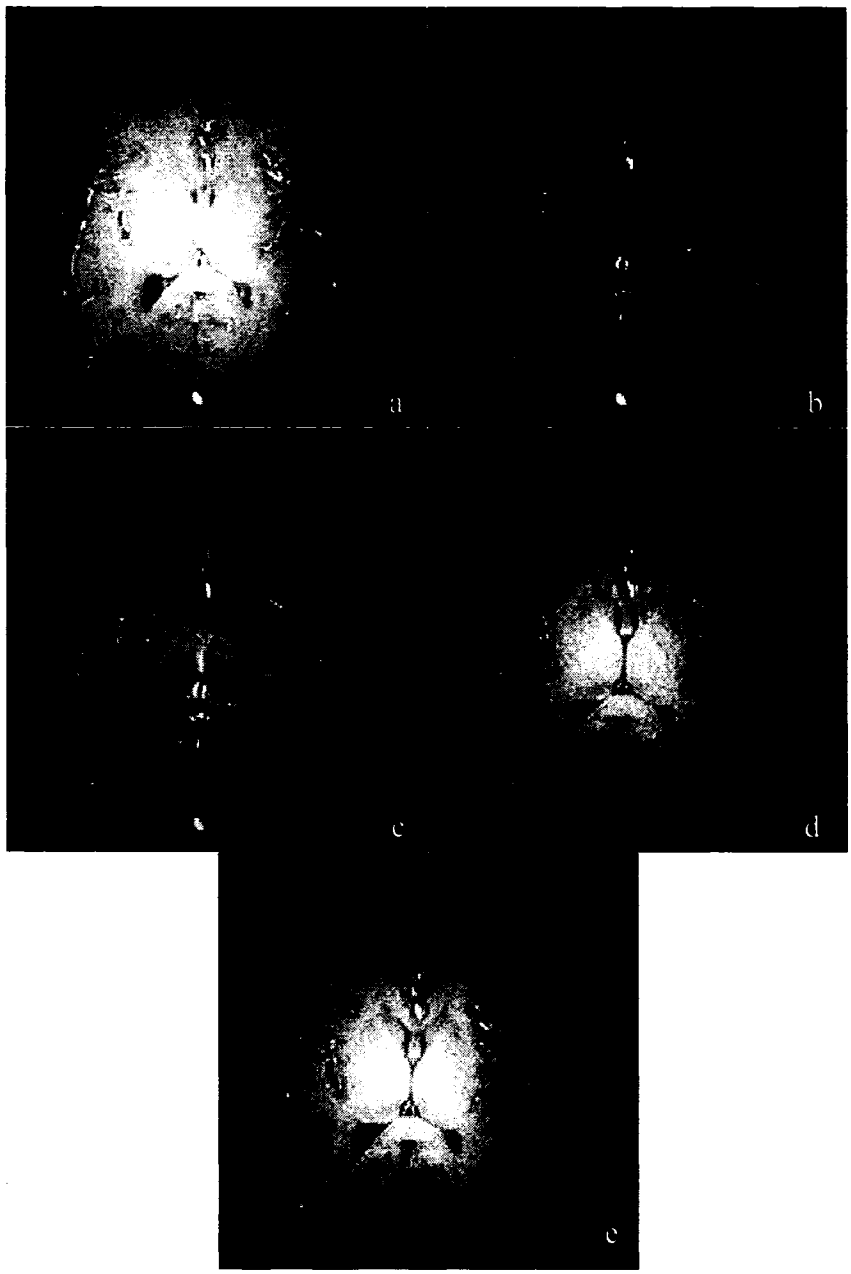

Figure 3.11 Axial 4.7 T 2-D images acquired with a TEM volume coil using identical receiver gain and window/level. Note that the receiver used was a volume coil, which has low receive sensitivity and low transmit B_1 at the sides of the head compared to the centre, due to destructive interference effects. This is the main reason for the nonuniformity seen in the images. Pulse sequence parameters were chosen for each sequence type to attempt to correct for the coil transmit nonuniformity while maximizing WM-GM CNR. Parameters other than window/level are the same as the previous figure.

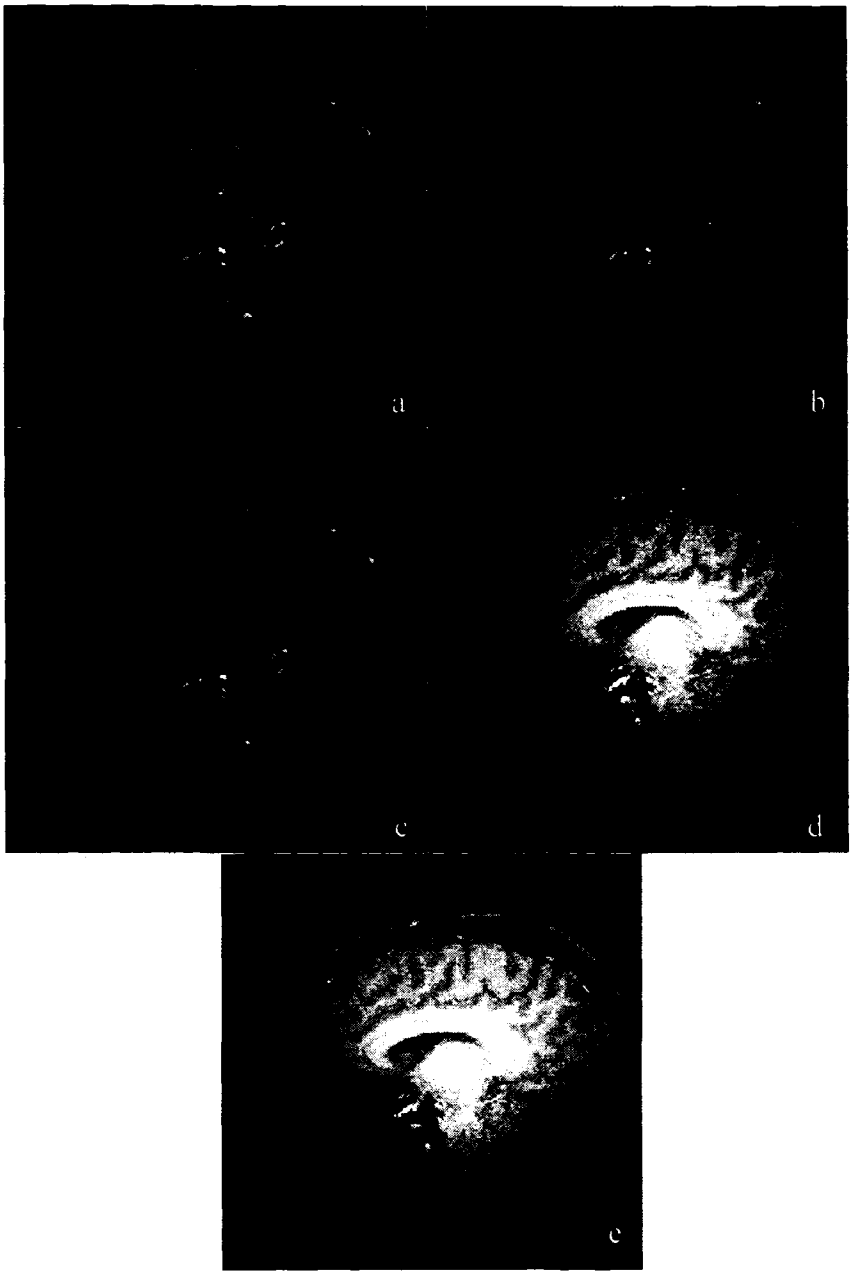

Figure 3.12 Sagittal 4.7 T 2-D images acquired with a TEM volume coil using identical receiver gain and window/level. Parameters other than slice orientation are the same as the previous two figures. The images show a choice of parameters for good CUR given each magnetization preparation pulse type (ie. MDEFT with soft pulses). If a phased array receiver coil had been used, the apparent image uniformity would increase because the inherently higher SNR of the phased array would provide additional compensation to that of the pulse sequences for areas of low B_1 at the sides of the head.

Table 3.2 Parameters for pulse sequences in Figure 3.10, Figure 3.11 and Figure 3.12. Pulse sequences in (a), (b), and (c) were designed by the author; parameters in (d) and (e) are from the literature[23] and implemented on a 4.7 T system by the author.

	Pulse Flip Angles in Degrees			τ_1/T_{prep}	τ_2 (ms)
	Magnetization Preparation Pulse #1	**Magnetization Preparation Pulse #2**	**RF Excitation (Average)**		
a	N/A	100 soft, average	17.50	0.23	440.4
b	N/A	180 adiabatic	20.50	0.26	423.3
c	110 soft, average	110 soft, average	22.00	0.44	320.3
d	110 adiabatic	125 soft, average	19.85	0.45	314.6
e	90 adiabatic	125 soft, average	18.50	0.39	348.9

Table 3.3 Measured values from Figure 3.10 and Figure 3.11. The listed CNR's and signal intensities are mean values measured in high B_1 regions of interest. The standard deviations of WM and GM for CUR were measured by using mean values from two regions of interest each, one in an area of high B_1, the other in an area of low B_1. In addition to the B_1 transmit inhomogeneity, it should be noted that the measured CUR values are affected by coil receive sensitivity. As an aside, notice that this table shows the CNR and SNR values are within the limits discussed in section 3.3.5 for selection of the excitation flip angle.

	Measured Central CNR	**Measured CUR**	**Central SNR**		**Side SNR**	
			WM	**GM**	**WM**	**GM**
a	8.7	1.1	39.1	30.3	27.7	20.0
b	8.7	1.0	21.1	12.4	5.27	2.7
c	11.1	1.3	39.6	28.5	25.9	19.5
d	9.3	1.1	31.4	22.2	18.0	11.1
e	9.0	1.0	32.0	23.0	18.2	11.1

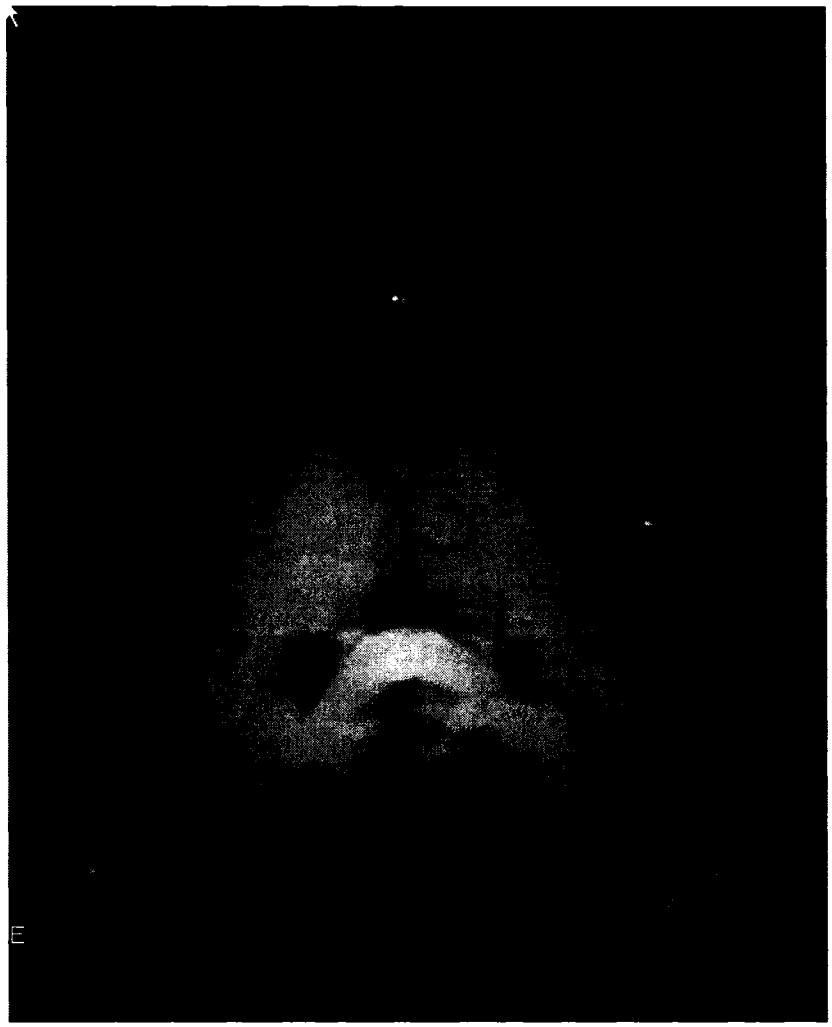

Figure 3.13 Single 1 mm thick slice from a 4.7 T MP-RAGE 3-D data set, using volume coil transceiver and adiabatic inversion. This image shows field focussing in the centre of the head and was acquired with parameters that were optimized for contrast but not for uniformity. At 4.7 T with a volume coil, the corpus callosum is the point of highest B_1 in the head[5]; it is the brightest region in the image.

Figure 3.13 was acquired with a matrix size of 256 (read) x 256 (PE_{inner}) x 64 (PE_{outer}). Each $TR_{overall}$ consisted of 64 views (PE_{inner}), for a total of 4 segments per PE_{outer}. FOV was 220 mm x 220 mm x 64 mm for a .859 x .859 x 1 mm voxel resolution. 1 average, 0 dummy views preceding each 64 view echo train, and 6 dummy segments were used. The magnetization preparation consisted of a 180°, 14.5 ms, 57 dB first order hyperbolic

secant adiabatic pulse, with TI = 1.08 s, slab thickness 70 mm, and a recovery time following acquisition and prior to the inversion pulse of 0.42 s. For the gradient echo, the excitation slab thickness was 64 mm, with flip angle = 23° and RF spoiling with 117° phase shifting, TR 10.51 ms, TE 4.62 ms, BW_{sam} = 50 kHz, acquisition time of 5.12 ms for 512 complex points, and a symmetric echo. The receiver gain was 14 dB.

Figure 3.14 Single slice from a sagittal reformat of the 4.7 T MP-RAGE 3-D data set shown in the previous figure, using volume coil transceiver and adiabatic inversion. Again, the corpus callosum is the brightest region in the image.

3.4.4 Discussion

Consider Figure 3.10 to Figure 3.12. Pulse sequence (a) is an MP-RAGE image designed by the author. It shows that MP-RAGE at 4.7 T is capable of producing images with a reasonable degree of uniformity and WM-GM contrast. In (b), the parameters were chosen to give a compromise between signal and uniformity; a different choice would yield slightly better signal and contrast but somewhat worse uniformity. One can see that it has the poorest B_1 inhomogeneity and signal of the five selected sequences. MP-RAGE with an adiabatic inversion is not capable of producing improvements in uniformity with the chosen T_{prep}.

The MDEFT pulse sequence with two soft preparation pulses in (c) displays a good degree of uniformity and WM-GM CNR. Pulse sequence parameter choices in (d) and (e), were taken from the literature[23] and implemented by the author. Pulse sequence parameters chosen in (a), (b) and (c) were discovered by the author. From Table 3.3, it appears that the CUR and CNR of the author's choices in (a) and (c) is comparable to that of Ordidge's 4.7 T MDEFT pulse sequence choices. Note that (a) and (c) do not use adiabatic pulses and therefore, the sequence SAR is much lower than (d) and (e); a greater SAR budget could allow for more RF pulses to further increase sequence capabilities, such as adding fat suppression. (d) and (e) show suppression of some blood vessels due to the use of the global adiabatic BIR-4 pulse. Be mindful also of the fact that part of the nonuniformity seen in these images is caused by the TEM volume coil's inhomogeneous receive sensitivity, and this affects the measured versus theoretical CUR values because the simulations do not take account of this.

3.5 Conclusion

Magnetization-prepared gradient echo pulse sequences, including MP-RAGE and MDEFT, were designed and fully tested, with both phantoms and in-vivo, by the author. A basic gradient echo sequence was used as the foundation. The MP sequences were designed to image human brain with the intent to maximize WM-GM contrast while attempting to minimize any signal intensity nonuniformities.

Numerical simulations were performed to compare 4.7 T profile flatness, signal amplitude, and contrast for a variety of situations: adiabatic vs. hard/soft preparation pulses; variation of readout flip angle; variation of magnetization preparation pulse flip angles; power calibrated to achieve an average flip angle across the head; variation of preparation and recovery times. Sequences must be individually optimized to maximize contrast, signal, and signal profile uniformity.

It has been shown in the literature that with FLASH[36] and MDEFT it is possible to reduce image centre brightening. Specifically at 4.7 T, experiments in the literature[23] indicate that it is possible with MDEFT using several variations of magnetization preparation. Comparable pulse sequences designed by the author were simulated and tested in-vivo at 4.7 T that show similarly uniform signal profiles and good contrast, with lower SAR. It was shown by the author that MP-RAGE can produce comparable contrast and uniformity to MDEFT. In addition, the use of local receive coils can mitigate the receive sensitivity falloff of circumscribing volume coils that cannot be accounted for by pulse sequence design.

Future work should consider that for these results, the T_{prep}, TR, and TE are constant, so the whole picture is not being seen. For example, there may be other MP-RAGE pulse sequences that have a superior contrast/uniformity to those already shown, for different values of T_{prep}. In addition, the choice of excitation flip angle may be somewhat limiting, because it is possible that slightly lower flip angles could have provided a further improvement in contrast or uniformity.

3.6 Bibliography

[1] JP Mugler III, FH Epstein, JR Brookeman, Shaping the Signal Response During the Approach to Steady-State in Three-Dimensional Magnetization-Prepared Rapid Gradient-Echo Imaging Using Variable Flip Angles. MRM 28, 165-185 (1992).

[2] PF Van de Moortele, C Akgun, G Adriany, S Moeller, J Ritter, CM Collins, MB Smith, JT Vaughan, K Ugurbil, B_1 Destructive Interferences and Spatial Phase Patterns at 7 T with a Head Transceiver Array Coil. MRM 54:1503-1518 (2005).

[3] H Barfuss, H Fischer, D Hentschel, R Ladebeck, A Oppelt, R Wittig, W Duerr. In Vivo Magnetic Resonance Imaging and Spectroscopy of Humans with a 4 T Whole-Body Magnet. NMR in Biomedicine, Vol. 3, No. 1, 31-35 (1990).

[4] CM Collins, W Liu, W Schreiber, QX Yang, MB Smith, Central Brightening Due to Constructive Interference With, Without and Despite Dielectric Resonance. JMRI 21:192-196 (2005).

[5] DL Thomas, E De Vita, S Roberts, R Turner, TA Yousry, RJ Ordidge, High-Resolution Fast Spin Echo Imaging of the Brain at 4.7 T: Implementation and Sequence Characteristics. MRM 51:1254-1264 (2004).

[6] CM Collins, S Li, MB Smith, SAR and B_1 Field Distributions in a Heterogeneous Head Model within a Birdcage Coil, MRM 40:847-856 (1998).

[7] Guidance for Industry and FDA Staff: Criteria for Significant Risk Investigations of Magnetic Resonance Diagnostic Devices. US Food and Drug Administration: Center for Devices and Radiological Health. Available from:
http://www.fda.gov/cdrh/ode/guidance/793.html. Document issued on: July 14, 2003.

[8] DL Thomas, E De Vita, S Roberts, R Turner, RJ Ordidge, Implementation of High Flip Angle Fast Spin Echo Imaging at 4.7 T Without Exceeding Safety Limits: Application to Human Brain Imaging. Proceedings of the 11th Annual Meeting of the ISMRM p.540 (2004).

[9] FH Epstein, JP Mugler III, JR Brookeman, Optimization of parameter values for complex pulse sequences by simulated annealing. Application to 3-D MP-RAGE imaging of the brain. MRM 31:164-177 (1994).

[10] JT Vaughan, M Garwood, CM Collins, et al., 7T vs. 4T- RF Power, Homogeneity, and Signal-to-Noise Comparison in Head Images. MRM 46:24-30 (2001).

[11] DL Thomas, E De Vita, R Deichmann, R Turner, RJ Ordidge, 3D MDEFT Imaging of the Human Brain at 4.7 T with Reduced Sensitivity to Radiofrequency Inhomogeneity. MRM 53:1452-1458 (2005).

[12] R Deichmann, CD Good, Turner R. RF Inhomogeneity Compensation in Structural Brain Imaging. MRM 47:398-402 (2002).

[13] JP Mugler III, JR Brookeman, Three-Dimensional Magnetization-Prepared Rapid Gradient-Echo Imaging (3D MP-RAGE). MRM 15:152-157 (1990).

[14] JH Lee, M Garwood, R Menon, G Adriany, P Andersen, CL Truwit, K Ugurbil, High Contrast and Fast Three-Dimensonal Magnetic Resonance Imaging at High Fields. MRM 34:308-312 (1995).

[15] J Hochmann, H Kellerhals. Proton NMR on Deoxyhemoglobin: Use of a Modified DEFT technique. JMR 38:23-39 (1980).

[16] DG Norris, TW Redpath, The MDEFT Sequence is Applicable for Clinical Systems Operating at 1 T. Proceedings of the 5th Annual Meeting of the ISMRM p.686 (1997).

[17] Y Zur, ML Wood, LJ Neuringer. Spoiling of Transverse Magnetization in Steady-State Sequences. MRM 21, 251-263 (1991).

[18] R Deichmann, A Haase, Quantification of T_1 Values by Snapshot-FLASH NMR Imaging. JMR 96:608-612 (1992).

[19] K Ugurbil, M Garwood, J Ellermann, K Hendrich, R Hinke, X Hu, SG Kim, R Menon, H Merkle, S Ogawa, R Salmi, Imaging at High Magnetic Fields: Initial Experiences at 4 T. Magnetic Resonance Quarterly, Vol. 9, No. 4, 259-277 (1994).

[20] DL Thomas, E De Vita, R Deichmann, R Turner, RJ Ordidge. Can Two Wrongs Make a Right? B_1-insensitive T_1-weighted Imaging of the Human Brain at 4.7 T using 3D MDEFT with a Standard Non-Adiabatic Preparation Pulse. Proceedings of the 11th Annual Meeting of the ISMRM p.84 (2004).

[21] RS Staewen, M Garwood, et al., 3-D FLASH Imaging Using a Single Surface Coil and a New Adiabatic Pulse, BIR-4. Investigative Radiology. 25:559-567 (1990).

[22] DG Norris, Adiabatic Rdaiofrequency Pulse Forms in Biomedical Nuclear Magnetic Resonance. Concepts in Magnetic Resonance, Vol. 14(2) 89-101 (2002).

[23] DL Thomas, TK Small, E De Vita, P Kinchesh, R Deichmann, R Turner, RJ Ordidge. Uniform Whole Human Brain T_1-weighted Imaging at High Field using 3D MDEFT with Optimized Preparation Pulses, Abstract and Poster. Proceedings of the 13th Annual Meeting of the ISMRM p.2173 (2005).

[24] www.fil.ion.ucl.ac.uk/spm

[25] R Deichmann, CD Good, O Josephs, J Ashburner, R Turner, MP-RAGE Sequences for Structural Brain Imaging. NeuroImage 12:112-127 (2000).

[26] IR Young, DR Bailes, GM Bydder, Apparent Changes of Appearance of Inversion-Recovery Images, MRM 2:81-85 (1985).

[27] HW Park, MH Cho, ZH Cho, Real-Value Representation in Inversion-Recovery NMR Imaging by Use of a Phase-Correction Method, MRM 3:15-23 (1986).

[28] JA Borrello, TL Chenevert, AM Aisen, Regional Phase Correction of Inversion-Recovery MR Images, MRM 14:56-67 (1990).

[29] PA Gowland, MO Leach, A Simple Method for Measuring Signal Polarity in Multi-Image Inversion Recovery Sequences for Measuring T_1. MRM 18:224-231 (1991).

[30] P Kellman, AE Arai, ER McVeigh, AH Aletras, Phase-Sensitive Inversion Recovery for Detecting Myocardial Infarction Using Gadolinium-Delayed Hyperenhancement, 47:372-383 (2002).

[31] R Deichmann, C Schwarzbauer, R Turner, Optimisation of the 3D MDEFT sequence for anatomical brain imaging: technical implications at 1.5 and 3 T. NeuroImage 21:757-767 (2004).

[32] RT Droege, SM Adamczak, Boundary Artifact in Inversion-Recovery Images, MRM 3:126-131 (1986).

[33] R Deichmann, H Adolf, U Noth, E Kuchenbrod, C Schwarzbauer, A Haase, Calculation of Signal Intensities in Hybrid Sequences for Fast NMR Imaging. MRM 34:481-489 (1995).

[34] N Takaya, H Watanabe, F Mitsumori, Elongated T_1 Values in the Brain and the Optimization of MDEFT Measurements at 4.7 T. Proceedings of the 11th Annual Meeting of the ISMRM (2004).

[35] EM Haacke, High Resolution Imaging: Why is it Important for T_1 Weighted Imaging, MRA, and SWI? Wayne State University, Categorical Course: Human MRI/MRS at High Static Magnetic Fields (2004).

[36] D Wang, K Heberlein, S LaConte, X Hu, Inherent Insensitivity to RF Inhomogeneity in FLASH Imaging. MRM 52:927-931 (2004).

4 High Field Magnetic Resonance Angiography

4.1 Introduction

Magnetic resonance angiography (MRA) is a well-known technique that is used to create images of blood vessels. The principal purpose of this investigation is to examine methods to optimize blood to background contrast and compensate for the effects of high field, such as longer recovery times and inhomogeneity of transmit and receive sensitivities, on in-flow angiograms. The magnetization prepared magnetic resonance angiography (MP-MRA) technique was chosen and implemented by the author on a 4.7 T Varian system, starting with a rudimentary sequence. This technique allows for excellent background suppression and cardiac gating, which account for B_1 nonuniformity and vessel pulsatility, respectively. A technique using no magnetization preparation was developed and compared to MP-MRA. Blood-to-background contrast is optimized by maximizing the amount of blood that flows into the imaging volume between gated 3D gradient echo pulse sequence data acquisitions, while minimizing background signal levels. Increased time for blood in-flow can be produced by exploiting the long high field T_1 values of brain tissue.

4.2 Methods

4.2.1 TOF vs. MP-MRA

TOF MRA relies on the fact that fresh, unsaturated blood is continually and quickly entering the imaging volume. Blood that has experienced the fewest RF pulses will tend to be the brightest, while tissue that has experienced the greatest number of RF pulses will be saturated, with its signal attenuated. This is the fundamental blood-to-background contrast mechanism underlying TOF.

There are certain cases where blood will be in a situation where it is necessary for it to experience many RF pulses as it travels through the imaging slab. This is where TOF blood signal begins to drop. MP-MRA[1] is beneficial in such situations, as the background suppression mechanism is different and does not directly rely on the same pulses as those used for imaging the blood. Instead, magnetization preparation pulses control the background WM and GM signal levels.

4.2.2 MP-MRA

In magnetic resonance angiography, inversion recovery (IR) is often used to create gated in-flow angiograms with background tissue suppressed. An IR fast 3D gradient echo MP-MRA[2] pulse sequence such as MP-RAGE facilitates imaging with low SAR at high fields within clinical time constraints, while accounting for vessel pulsatility and B_1 inhomogeneity.

The basic procedure for MP-MRA is as follows. First a slab of interest is chosen over which it is desired to image blood vessels. Axial slab orientations tend to have the fastest through-plane flow in the head and neck. Sagittal orientations tend to have in-plane flow, and these should especially bring out the advantages of the magnetization-prepared (MP) technique.

Some sort of time alignment to the heartbeat may be performed, called cardiac triggering or gating. At the appropriate time, the magnetization preparation pulses prepare the imaging region of interest. Usually for MRA, selective inversion pulses are used. The effect of the selective inversion is ideally completely localized to the excited slab, and directly affects the tissues (such as WM, GM and CSF) that are located within the slab limits defined by the preparation pulse slab selection gradient.

As time passes, the longitudinal magnetization recovers from the inversion according to the well-known equation, which has already been discussed: $M_z(t) = M_0(1 - 2\exp(-t/T_1))$ where M_0 is the initial magnetization, and t is the time after the inversion. In reality, this is just a simplified case of the MDEFT magnetization preparation equation, with the first preparation pulse set to 0° and the second pulse set to 180°. Noting that the possible received signal intensity is directly proportional to the current level of the longitudinal magnetization, acquisition of data can be timed to occur when the value of the magnetization passes through an arbitrary value, from $-M_o$ to M_o.

In general physiology, several different tissue types, such as muscle or fat, can envelop vessels. For MRA purposes, it be can considered that WM or GM surrounds most of the vasculature of the brain. Unfortunately, WM and GM have different T_1 values, different by approximately half a second at 4.7 T. In this work, it was chosen to null the WM instead of the GM, because larger-sized vessels can be more clearly imaged given the resolutions involved, and these are situated mainly in WM. It may also be feasible to acquire data when GM signal is nulled. Another possibility is acquisition when WM and GM magnetizations are equidistant from the zero level.

During the longitudinal magnetization recovery time, fresh blood, which has been untouched by any magnetization preparation pulse, flows into the imaging volume. The signal of the blood that enters the imaging volume during magnetization recovery will be bright, because the blood does not experience the magnetization preparation pulse. If the blood had experienced the 180° pulse, because blood T_1 values at 4.7 T are on the order of WM/GM T_1 values (WM $T_1 \cong 1.05$ seconds, GM $T_1 \cong 1.5$ seconds, blood $T_1 \cong 1.9$ seconds[3]), by the time the WM/GM longitudinal magnetizations pass through their zero level, blood signal would be nearly zero as well. Hence, it is imperative that blood not experience any sort of RF pulse until such time as it is necessary to actually begin acquiring data.

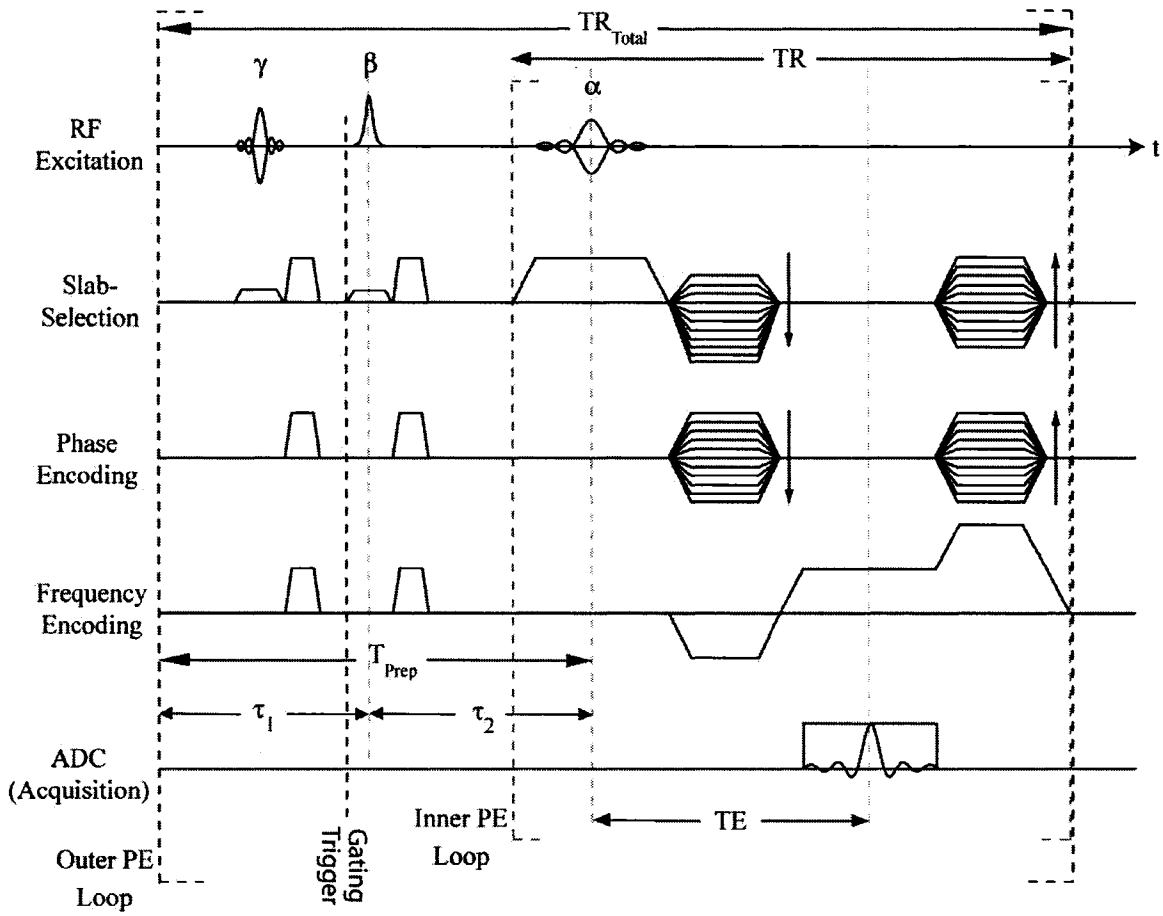

Figure 4.1 3D MP-MRA pulse sequence timing in detail (not to scale). $\gamma = 180°$ soft, $\beta = 180°$ adiabatic, $\alpha = 20°$ here. The γ pulse is a venous saturation pulse. Gating is set to begin waiting for a trigger after γ. Immediately after triggering, β is applied. The entire outer PE loop within the time TR_{total} is repeated to fill k-space. T_{prep} comprises a delay τ_1, the β preparation pulse, and another delay τ_2, which runs up to the centre of the first α pulse. Each preparation pulse is followed by spoiler gradients. Subsequent to the preparation are many gradient echo acquisitions, indicated by the inner PE loop. Data readout is indicated by the analog-to-digital converter (ADC) signal.

After the magnetization preparation period, sometimes labeled "inversion recovery time" TI, ends, data acquisition begins. Usually acquisition occurs over several phase encoding steps, also called phase encoding views or, simply, views. Each view consists of an RF

pulse followed by some selected method of data acquisition. Numerous sequence choices are possible for the echo train that is acquired, such as steady-state free precession (SSFP), etc. A spoiled FLASH gradient echo pulse acquisition was chosen for this work due to its T_1-weighted contrast.

Due to the limited number of phase views that can be acquired per heartbeat, it is necessary to break the acquisition up into multiple segments. Thus, subsequent to the acquisition of a small number of phase views followed by a possible additional delay, the entire pulse sequence begins again. The additional delay may be necessary in order to wait for another cardiac trigger to occur. Then, another delay after the trigger may occur, and the entire process begins again starting with the magnetization preparation step.

Certain modifications[4] to the original MP-MRA sequences were taken advantage of in this work. The time between the preparation pulse and the acquisition of data was optimized to attempt to provide the best blood-to-background contrast. First order gradient moment nulling was not used. With the removal of the excess gradients required for first order moment nulling, the TE and TR periods were significantly shortened. In the read (frequency encoding) direction, an asymmetric echo was used, which served to further reduce the TE and TR. Steps were taken to reduce venous lumenal signal intensity, involving the addition of a soft-pulse inversion slab.

Centric phase-encode ordering[5] was used. With centric acquisition of k-space data in conjunction with magnetization preparation pulses, the preparation step can precisely determine contrast and signal of the background. Though the drop in magnetization during acquisition views later in each segment may result in some blurring, blood-to-background contrast is well preserved[6,7].

In addition, consideration of the direction of blurring may be of interest, relative to the direction of blood flow, as through-plane blur will not be very noticeable with through-plane flowing blood, whereas in-plane blur will be. Reversing the nesting of the 3D and

2D phase encoding loops can control the direction of blur. For MRA, the optimal slab orientation relative to the direction of vessels must be considered carefully[8], and may override concerns about the direction of blur.

Excitation slab thickness profoundly affects the signal intensity of distal vessels furthest from the blood entry point. As blood travels through the slab, phase dispersion in combination with saturation during the application of excitation pulses combine to reduce the blood signal. Thinner slabs will provide more uniform intensity across their volume, because blood experiences fewer RF pulses as it travels. The cost is that less vascular territory will be covered during the course of the scan. For these reasons, multiple thin slab acquisition was chosen. There is some time cost associated with multiple thin slab acquisition because the slabs necessarily overlap. The reason for the overlap is due to the fact that partitions (slices) on either side of the slab usually have to be discarded because of signal phase aliasing, due to the imperfect slice selection profiles of soft excitation pulses. That is, because the profiles are not perfectly rectangular, signals from either end of the slab may intermingle.

4.2.3 Blood-to-Background Contrast Optimization

A noise-independent measure of blood-to-background contrast can be calculated as[9]:

$$\text{Contrast} = (\text{Blood Signal} - \text{Background Signal}) / (\text{Background Signal}) \qquad (4.1)$$

Another method of evaluating contrast is by calculation of the blood-to-background contrast-to-noise ratio:

$$\text{CNR} = (\text{Blood Signal} - \text{Background Signal}) / (\text{Noise}) \qquad (4.2)$$

where "Noise" is the standard deviation of the noise, and is measured in an area such as air. The CNR number incorporates actual SNR values of the blood and background, so it is more meaningful when compared against SNR values of other tissues. High blood-background contrast is desirable.

In MP-MRA, blood-to-background contrast is optimized by carefully controlling the amount of blood that flows into the imaging volume during the time TI between the preparation pulse and the 3D gradient echo pulse sequence data acquisitions. Simultaneously, background signal levels have to be minimized. TI affects both the background and the blood signal intensity. There is usually a tradeoff that has to be made, and one or the other is sacrificed to try to maximize blood-to-background contrast. The longer T_1 values of brain tissue at high fields can be exploited to provide improved blood-to-background contrast by satisfying the competing time requirements of blood in-flow and background suppression. Remember that SNR is proportional to field strength[10]; the increased SNR available at 4.7T further increases the achievable CNR.

With the MP-MRA technique, the main mechanism for control of the blood signal level stems from the timing of the magnetization preparation pulse. Usually it is the time between the magnetization preparation pulse and the beginning of data acquisition that is increased in order to attempt to provide maximal inflow enhancement. With more time between the magnetization preparation and the beginning of data acquisition, more fresh, unsaturated blood is allowed to enter the imaging volume. In turn, blood signal will be higher. This is especially important in regions of slow flow, such as the distal intracranial arteries. The more time allowed for in-flow replenishment, the higher the blood signal.

For inversion recovery angiography, often it is desired to limit the background signal relative to the blood vessels of interest. Suppressing the background will increase blood-to-background contrast. Control of background suppression for IR angiography is possible by carefully timing the inversion pulse. After the inversion pulse, the background tissue recovers from the inversion, over time. If the timing is correct, the

tissue signal can be minimized by acquiring data when the longitudinal magnetization passes through its zero point, $M_z(t) = 0$. With minimal signal received from background tissue, blood vessels will be more easily discerned.

The timing can be optimized through numerical simulation of the Bloch equations[11]. Analysis of the longitudinal magnetization transient evolution provides sufficient information to maximize background suppression. For a given heartrate, at steady state the signal levels and the required TI to null the background tissue signal can be calculated. Thus, for a range of different heartrates the optimal TI for background suppression is determined. The reason that TI is different for different heartrates is because the total echo train time stays the same while the total time between data acquisition segments continually decreases as heartrate increases. Thus, the steady state signal level at the time of the inversion pulse will continually decrease as heartrate increases. In turn, the time required for the background tissue longitudinal magnetization to recover to zero decreases with increasing heartrate.

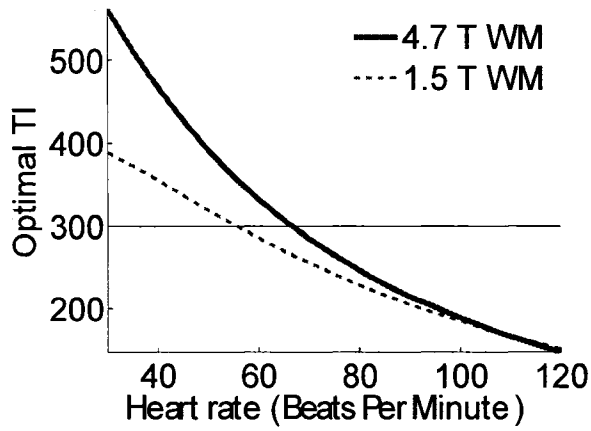

Figure 4.2 Effect of field strength on the optimal inversion time required to null white matter (WM). Clearly, optimal TI is increased at high field, especially for lower heart rates. This is due to the longer tissue T_1 times at higher field strengths. In comparison, the optimal time required to suppress the background is somewhat shorter at 1.5 T, due to the shorter T_1 times. The extra 4.7 T inflow time increases blood signal, resulting in improved blood to background image contrast.

4.2.4 Venous Saturation

Use of the MP-MRA technique can produce venograms intermingled with angiograms. Often it is desirable to remove the veins; using postprocessing to accomplish this is a possibility. Another technique involves changing certain parameters, so that venous saturation can be performed by the pulse sequence. The latter was investigated.

One variation calls for the adiabatic inversion pulse to be increased in thickness, such that it extends superiorly in the human head to envelop the veins. Besides changing the pulse profile bandwidth, the slab selection offset parameter must be changed as well, so that the inversion profile begins at the same place on the blood-inflow side. This way, on the side of the slab where blood enters, blood will begin to experience the inversion at the same spatial location as for the case where the inversion pulse is not extended.

Instead of the single-pulse slab extension method, a second simultaneous inversion slab offset from the imaging slab was opted for in this work. Either method will effectively serve to saturate most of the venous signal in the final images, but each has its own inherent advantages and disadvantages.

The disadvantage of using a single adiabatic inversion pulse and simply extending it superiorly in the head to suppress intracranial veins involves the relationship between an adiabatic pulse's total profile width, and the width of the transition between no inversion and inversion. The width between the spatial extent of the inversion and the area where the pulse has no effect is called the transition width. The thickness of the adiabatic pulse, also called the bandwidth, is usually measured between the midpoints of the two transition widths on either end. The problem lies in the fact that, if the bandwidth is increased, the transition width is increased as well. This means that increased saturation of inflowing arterial blood will take place. It is true that the adiabatic pulse can be

redesigned so that the transition width is smaller, given a larger bandwidth. The cost, however, is an increase in power requirement, and hence SAR. It was deemed that, due to the fact that the adiabatic pulses already involved were somewhat long (on the order of 15ms), and the peak power requirements already quite high (approximately 58 dB), it would be better to separate the venous saturation into a separate pulse.

An adiabatic inversion pulse was used for the main magnetization preparation stage. A 180° sinc pulse was used for the venous saturation, and was placed superior to the adiabatic inversion slab. The advantage of using a separate pulse for venous saturation is that the transition width of the adiabatic inversion pulse can remain thin, without having to redesign the pulse with an exorbitantly large power requirement.

The primary disadvantage of the combination of the two pulses is an increase in SAR, so much so that the use of fat suppression was ruled out. A secondary disadvantage is the fact that the sinc pulse has an uneven inversion profile; this is mainly due to the fact that its slab-selection gradient is so small that it is on the order of background static magnetic field inhomogeneities. The adiabatic pulse itself is less susceptible to such inhomogeneities, even when used with a small slab select gradient, due to its adiabaticity. It should also be noted that the adiabatic pulse slab thickness is usually 1-3 times thinner than the venous saturation slab. Because the thinner slab necessarily requires a larger slab select gradient area, it is not as susceptible to background inhomogeneities as the venous saturation slab.

The background field nonuniformities can cause the venous inversion slab to have a somewhat warped profile, fluctuating on the order of ±1 cm in the transverse direction (assuming axial slab selection). It has to be carefully verified that the venous slab select pulse profile does not overlap with the arterial inversion pulse profile. Otherwise, odd artefacts will result. The way to do this is to orient both inversion slabs perpendicular to the imaging plane, and acquire an image. Signs of overlap and the extent of warping of the venous saturation slab can be scrutinized in this manner. Some leeway is useful to

ensure no overlap; an inter-slab distance of approximately 1cm was deemed sufficient in this regard.

It may be that it is possible to design an adiabatic pulse with a thin transition width on one side, and a wider transition width on the other, in combination with the required large pulse bandwidth. It is theorized that this pulse, would exact a lower power cost than simply having thin transition widths on *both* sides of the pulse, in combination with the large bandwidth. It also could be more convenient and require lower power than adding a separate pulse for the venous saturation. Unfortunately, no references to such an adiabatic pulse design could be found in the literature as of the time of this writing.

4.2.5 Adiabatic Pulse Considerations for High Field MRA

A particular MRA problem is that as transition widths of the adiabatic pulse's longitudinal magnetization excitation profile widen, more inflowing blood is saturated. This can be negated somewhat by designing adiabatic pulses with wider bandwidths and hence thinner transition widths, at the expense of increased SAR. Every reduction in the transition width helps to increase the blood signal, because blood that may be just outside the imaging slab prior to the inversion pulse may end up in distal arteries by the time acquisition occurs. And with a thinner transition width, the pulse saturates less adjacent blood, which can translate to brighter distal lumens. The M_z transition width of an adiabatic inversion pulse can be reduced in exchange for a larger power requirement.

A unique high field consideration for adiabatic pulses is that, in fact, B_1 homogeneity can affect the pulse flip angle. Suppose one determines the power requirement to satisfy the adiabatic condition for a given pulse, at the centre of the brain. This is the point of highest B_1 strength. One must also realize that the sides of the head will have a B_1 strength which is approximately 50% that of the central part of the brain, at 4.7 T. Thus, the adiabatic pulse should use approximately *double* the power determined by looking only at the centre of the brain. If this is not done, one risks the adiabatic condition not

being met at the sides of the head. This could cause the magnetization to not fully rotate to the desired flip angle.

Typically, adiabatic pulses will require between 5-15 ms to complete. Long adiabatic pulses on the order of 100 ms are not recommended due to T_1 recovery effects, which will take place during the pulse duration. Also, when examining pulse length, one must consider that the T_2^* values of tissues are on the order of 25 ms at 4.7 T. 15 ms adiabatic pulses were used for this work.

Several researchers have proposed adiabatic pulses for slice and volume selection with arbitrary flip angles[12,13]. Some interest was generated for using such pulses during the data acquisition for echo trains. Unfortunately, sequence SAR would be prohibitive because of these pulses. Besides the power problem, adiabatic pulses have relatively long duration, and as such they are inappropriate for sequences with short echo spacings that require rapid replay of excitation pulses. Instead, simple soft pulses were used for slice selection.

4.2.6 Improvement of the Image Uniformity

In general, when adiabatic inversion is not used, high field destructive interference[14] is seen to cause noticeable intensity nonuniformities across the background tissues (WM and GM) in the MRA source images.

It may be possible to increase the background signal uniformity using a B_1 compensation scheme involving a preparation pulse type matching the excitation pulse type (ie. hard or soft pulse). However, for maximal background signal uniformity, the timing and flip angle of the preparation pulse will have to be changed, and this may prove to be somewhat detrimental to the blood-to-background contrast.

Adiabatic inversion can produce images with flatter background RF profiles across the brain. The adiabatic inversion pulse itself is B_1-insensitive, so all of the background tissue is inverted equally well, regardless of spatial position. As the inverted magnetization recovers, the WM and GM longitudinal magnetizations may recover at slightly different rates. The key point is that all of the WM throughout the brain recovers at the same rate governed by the WM T_1 value, and all of the GM recovers at a rate governed by the GM T_1 value. (This discussion neglects the fact that there is, in reality, a gradient of T_1 values for each tissue type.) Thus, after the expiration of TI, the WM and GM signal levels will still be constant with respect to spatial position. Hence the background tissue signal profiles will essentially be uniform across the brain. In essence, the B_1-insensitivity of the adiabatic inversion has been carried over in time to the point where data acquisition starts. Because of centric phase encode ordering, wherein the first views acquired control the contrast, most of the background uniformity is preserved. Furthermore, additional inhomogeneity may be observed in the background tissue due to the nonuniform receive sensitivity of the RF volume coil. Postprocessing, or the use of local receive-only surface coils, can significantly reduce receive B_1 inhomogeneity. A phased array has proven utility for MRA[15] and is preferable to simply using postprocessing or surface coils, because it has certain advantages, such as increased SNR[16].

4.2.7 Prospective Gating

Acquisition of k-space data while blood is moving causes artefacts; the mechanism of this is well understood. Gating a sequence so that acquisition occurs during periods of slow blood flow (diastole) results in less blur and reduction of pulsatility artefacts. In turn, magnetization relaxation periods may be timed to coincide with periods of fast flow (systole). A particular problem that was resolved is to determine the correct timing of the sequence with respect to the cardiac cycle, given that there is some delay between the physiological R wave and the corresponding gating trigger. The velocity of blood flowing

through the carotids was examined[17], and using this it was possible to determine the optimal timing.

Due to the time constraints of the human heartbeat, and given the repetition times on the order of 10 ms for typical MP-MRA, acquisition may only occur over a finite number of phase views. Unfortunately, the ideal imaging time window between heartbeats is usually so short that the number of possible views is on the order of 24-50. This explains, in part, the short repetition times (TR's) and echo times (TE's) which are prevalent among MP-MRA sequences.

A Medrad pulse oximeter was set up for cardiac gating. A sensor that measures a human heart pulse is connected to the subject's finger and is connected to the Medrad unit, which in turn converts the heart pulse into an analog pleth pulse signal. This signal is converted by the gating circuit shown in Figure 4.3 to a suitable transistor-transistor logic (TTL) signal that is fed into the "Ext. Trigger" gating signal input on the 4.7 T spectrometer cardcage. With this setup, a trigger is sent to the 4.7 T system with each heartbeat. Note that a sensor on the finger measures the heartrate signal, so there is some delay between the actual R wave of the heart and the corresponding trigger signal sent to the pulse sequence.

One problem involved with the gating process was determining if the oximeter had a viable output signal for gating purposes. An oscilloscope and voltmeter were used to measure the signal output from various circuit boards within the pulse oximeter unit. Finally, a suitable analog pleth pulse signal was located emanating from the 15-hole Medrad digital/analog outputs port on the back panel. Considering the upper left hole 1 and the lower right hole 15, the analog pleth pulse signal is located on hole 12.

The pleth pulse output needed to be converted into a TTL gating signal to accommodate the Varian INOVA receiver gate trigger input. This was done with a simple op-amp comparator circuit. Because the op-amp circuit requires 5 V_{DC} power to operate, the

author searched the pulse oximeter boards and ports for this DC voltage and a ground to connect the op-amp to. A suitable ground was located on hole 5 of the Medrad digital/analog outputs port by first disconnecting the Pulse Oximeter battery and power supply, then using a multimeter to measure signal from each hole of the port, with a second multimeter connector on a known ground for reference. It was found that the pulse oximeter does not emit a suitable 5 V_{DC} source, but a 2 V_{DC} source was located on hole 13 of the Medrad digital/analog outputs port. Thus, an external battery was used to power the op-amp gating circuit.

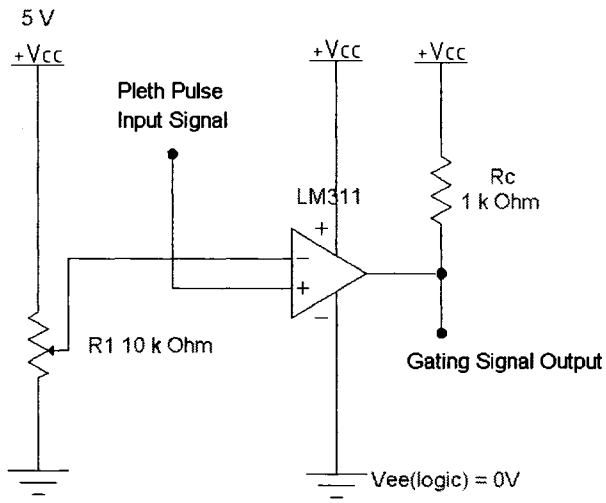

Figure 4.3 Op-amp comparator circuit used for MRA gating on the 4.7 T system. As shown, the negative op-amp input provides an adjustable threshold voltage level, which is compared with the positive input (analog pleth pulse signal). A TTL gating signal is output to the 4.7 T spectrometer for use in triggering the MRA pulse sequence. It was noted that a minimum threshold voltage of approximately 550 mV_{DC} was required to obtain a reasonable triggering from the analog pleth pulse signal.

When the trigger sensor of the pulse oximeter is connected to a subject's finger, it was noted that the finger must be stationary, otherwise the pulse oximeter will not trigger properly. In addition, the DC value of the analog pleth pulse was noted to correlate

somewhat with the subject's breathing, with an increase in DC value corresponding to inspiration, and a decrease with expiration.

4.3 MP-MRA Images at 4.7 T

4.3.1 Effect of the Removal of Magnetization Preparation

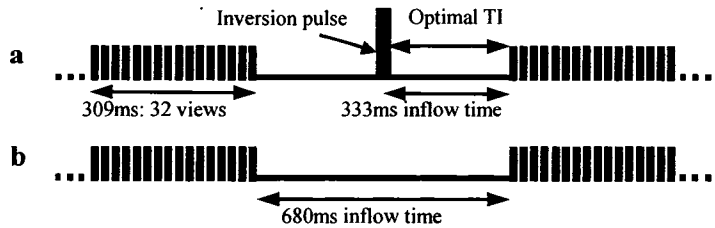

Figure 4.4 a) Typical timing for a segment of a 3D MP-MRA IR sequence. After a slice-selective adiabatic inversion pulse, some blood in-flow time passes, followed by acquisition of 32 views, then by some relaxation time, etc. b) The same sequence without MP allows for a much larger inflow time.

Normal volunteers were imaged on a 4.7 Tesla system (Varian INOVA) with an IR gradient echo pulse sequence (MP-RAGE) (*Figure 4.4*a). Volunteers were also imaged with an identical sequence, excluding the inversion pulse (*Figure 4.4*b). Numerical simulations were performed to determine the optimal sequence timing parameters required to attain maximum background suppression and long inflow time for the IR angiograms. The pulse sequence timing was as follows (ie. for a heart rate of 60 beats per minute): TR = 9.68ms, TE = 3.59 ms, TI = 333 ms, and an intersegment delay of 347 ms for (*Figure 4.4*a), and 680 ms T_{prep} for (*Figure 4.4*b). A matrix size of 384 (readout) × 256 (PE_{inner}) × 64 (PE_{outer}) was used, for a 64 mm thick slab and a total scan time of 8 minutes 26 seconds, and an effective voxel volume of .429 mm × .859 mm × 1 mm. The readout employed an asymmetric echo of 75%. Each 3D partition in the PE_{inner} loop totalled 256 phase encodes, and was divided into segments comprising 32 centrically ordered phase views, for a total of 8 segments per inner loop. The excitation used 2 ms sinc pulses with a flip angle of 20° and RF spoiling with 117° phase increments. Gradient spoiling was

also used, and crusher gradients followed the inversion pulse. A 15 ms 54 dB 3rd order hyperbolic secant adiabatic pulse with a 64 mm thick slab was used. 2 dummy segments and 2 dummy views with RF were also used. SAR was below 3.0 W/kg throughout.

At 4.7 T, the extended T_1 times are such that background signal may be easily saturated even *without* an inversion pulse, but including a delay between echo trains. The outer loop phase encoding was sequential, with the inner loop centric; this may partly explain why the background appears saturated more than the blood. The dummy views provide a partial TOF effect, improving blood-to-background contrast without magnetization preparation. With this novel method, by removing the inversion pulse, it is possible to increase the inflow time between segments, but still achieve sufficient background suppression. Thus, a high-field, segmented 3D MRA pulse sequence does not require magnetization preparation, but instead can rely on the long magnetization recovery times at 4.7T and an extended inflow time to produce blood contrast. This new technique was compared to a standard magnetization-prepared angiography sequence (MP-RAGE).

Images were obtained using a sequence with a delay between echo trains but without magnetization preparation pulses, and compared to MP-RAGE. These preliminary results show approximately the same blood-to-background contrast at the main middle cerebral artery in the source images for both sequences. With a thick slab and an inversion pulse (MP-RAGE), there is less in-flow time due to the requirement of background suppression, and a significant quantity of blood is saturated; thus the blood-to-background contrast is reduced even with the excellent background suppression. The sequence with no inversion or preparation of any kind, on the other hand, allows for higher blood signal because of increased in-flow time, at the cost of less complete background suppression. This explains the similar contrast between the two different sequence types. However, the sequences could be compared with more finely tuned, individually tailored parameters, to attempt to further optimize the blood-to-background contrast intrinsic to each.

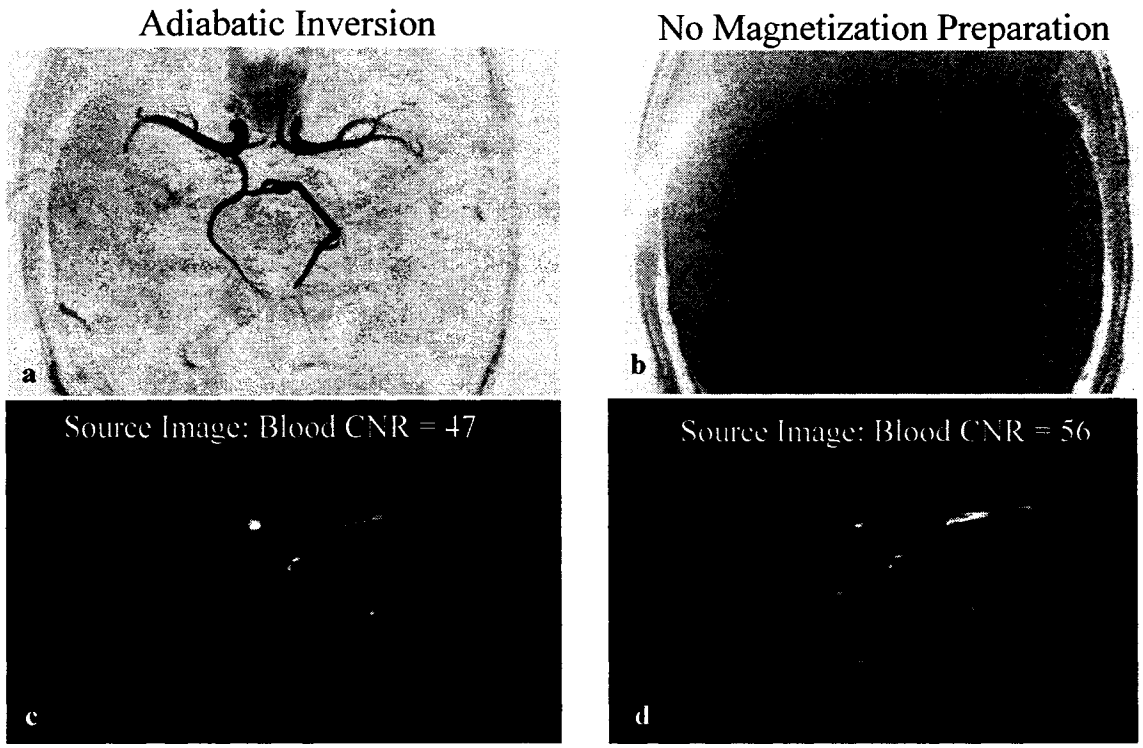

Figure 4.5 4.7T images. a,b): Complete 15 slice MIP images (white/gray inverted) covering 15 mm of the Circle-of-Willis, (a) with inversion pulse, and (b) without inversion pulse. c,d): 1mm thick source images, (c) with inversion pulse, and (d) without inversion pulse. Notice that similar blood-to-background contrast is achieved in both cases.

4.3.2 MP-MRA with a Receive-Only Phased Array

The intracranial circulation of normal volunteers was imaged on a 4.7T system (Varian INOVA) with a triggered IR gradient echo pulse sequence (MP-MRA). A standard volume coil was used for transmission, and volume coil receive was compared to 4 coil phased array[18] receive, as shown in Figure 4.6 to Figure 4.8. The pulse sequence timing was as follows: TR = 9.68 ms, TE = 3.59 ms, and for an example heart rate of 60 beats per minute, inversion time (TI) = 333 ms, intersegment delay = 347 ms, with 6 dummy

segments preceding the start of acquisition. The inner PE loop used 8 segments with 32 views per segment in order to achieve 256 PE steps. 4 dummy views with RF preceded each echo train acquisition in order to attempt to minimize artefacts from the steep blood signal falloff at 4.7 T. A matrix size of 384 (read) × 256 (PE_{inner}) × 32 (PE_{outer}) was used, for a total scan time of about 4 minutes 30 seconds per slab, and an effective voxel volume of .429 mm × .859 mm × 1 mm. Fractional echoes of 80% were used, with a BW_{sam} of 100 kHz and an acquisition time of 3.84 ms. RF spoiling[19,20] with a transmitter phase increment of 117° was used, as well as gradient spoiling with 21 mT/m, 2 ms gradient strength. Two overlapping 32 mm slabs from the same volunteer were combined into a single maximum intensity projection (MIP) image, and acquisition was gated to the subject's heartbeat via the pulse detected by a finger sensor. A 15 ms third order hyperbolic secant adiabatic pulse with a 32 mm thick slab was used for in-plane inversion; its power was limited to 56 dB to reduce SAR. A sinc pulse, with a 140° (reduced from 180°) flip angle also to decrease SAR, with thickness 32 mm and offset 40 mm superiorly from the adiabatic pulse was used for venous saturation. Both the inversion and venous saturation slab were offset superiorly by 20 mm for acquisition of the second slab. The receiver gain was set to 42 dB. 21 mT/m, 16 ms crusher gradients followed both preparation pulses. First order shimming was performed using the PRESS pulse sequence on a 150 mm × 150 mm × 46 mm slab centred on the overlap of the multi-slab acquisition. PRESS was also used for power calibration over the same volume to give an approximate average flip angle, which resulted in a 90° pulse of 56 dB, 4 ms, 3078 fine power. Each 3D partition was divided into segments comprising 32 centrically ordered phase views, each with 2 ms excitation sinc pulses of flip angle 20°. RF power was kept below 7.5 Watts for both short (10 second) and long (5 minute) term averaging throughout the scan, and thus assuming a head mass of 3 kg, the SAR was within the 3 W/kg safety limit. A volunteer was also imaged with a 2D version of the MP-MRA sequence with varying TI (Figure 4.10 and Figure 4.11). Several volunteers were imaged for testing purposes prior to the final scan. Numerical simulations were performed to determine the optimal sequence parameters required to attain complete background suppression and maximal inflow time for the IR angiograms.

Figure 4.6 MRA with a volume coil receiving at 4.7 T: complete 52 slice maximum intensity projection (MIP) covering 52 mm of the intracranial arteries. The birdcage volume coil receive sensitivity falls off towards the sides of the head, resulting in dimmer distal arteries. Notice the excellent suppression of veins, produced by a secondary saturation pulse. Notice also that the fat signal at the sides of the head is significantly smaller than the arterial blood signal, even without fat suppression.

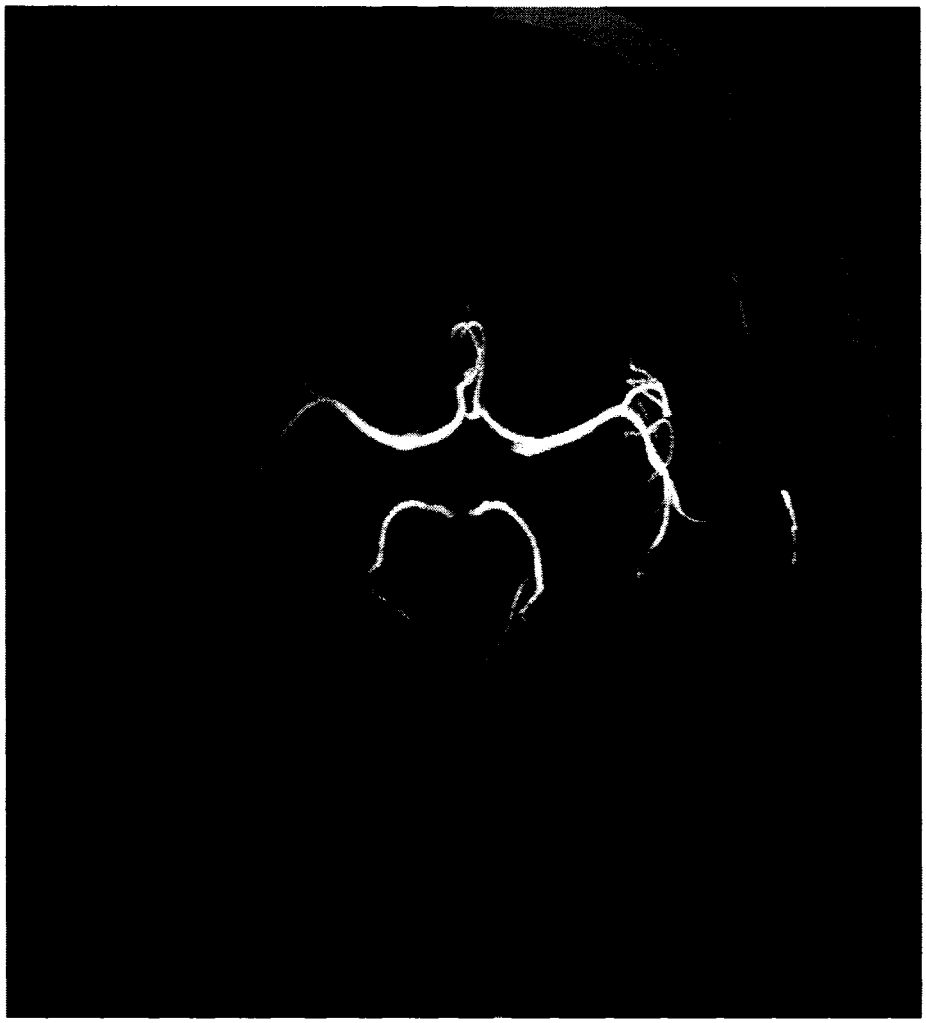

Figure 4.7 MRA with a single surface coil[18] receiving at 4.7 T: complete 32 slice MIP. It is evident that vessels near the sides of the head are much brighter with a surface coil receiving, as compared with a volume coil receiving. This is not the case with vessels positioned further from the surface coil, because sensitivity falls off with distance from the coil. The curved grey segment indicates placement of the surface coil relative to the head.

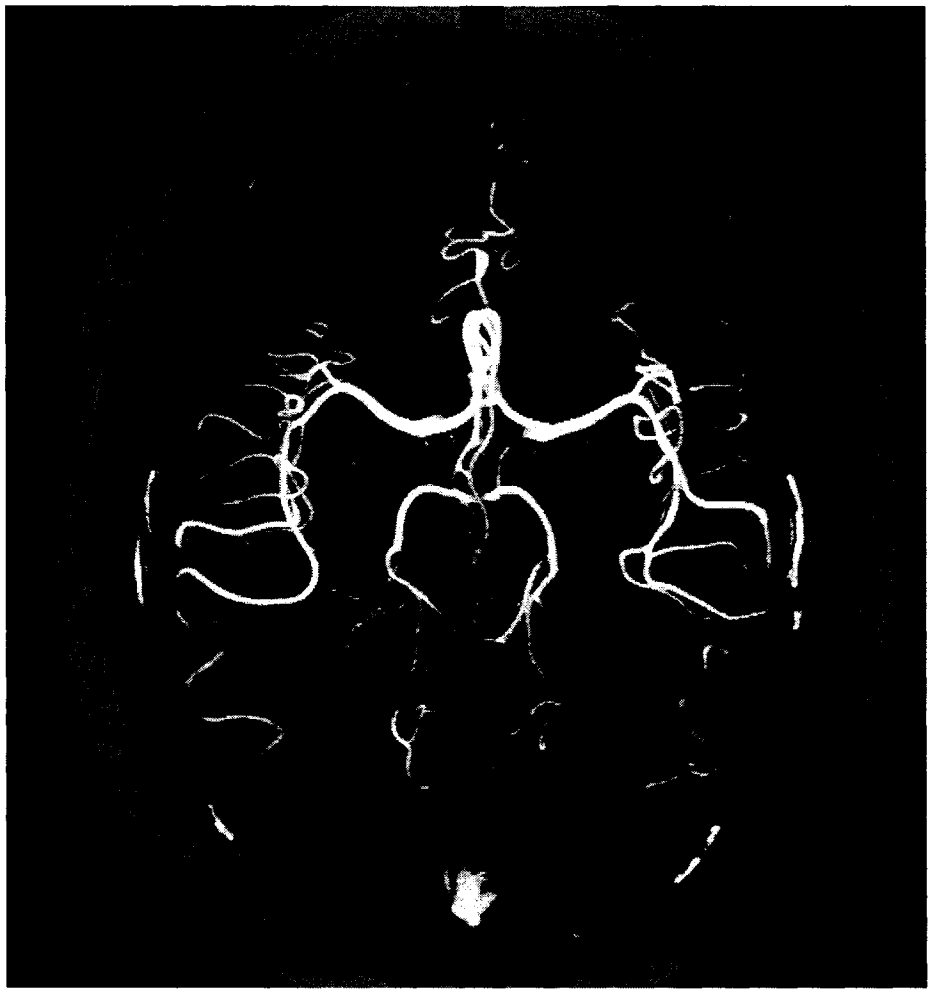

Figure 4.8 MRA with four coils receiving simultaneously at 4.7 T: complete 52 slice MIP. Note the increased signal intensity of peripheral vessels as compared with the case when the birdcage coil is the receiver, as in Figure 4.6. The blood to background CNR has a value of up to 87, with blood signal measured in distal arteries approximately 3 cm from the surface of head, and background signal measured close to the centre of the head. In the main middle cerebral artery (MCA), the blood to background CNR has a value of up to 108. The curved grey segments indicate placement, relative to the head, of each of the four surface coils that make up the phased array.

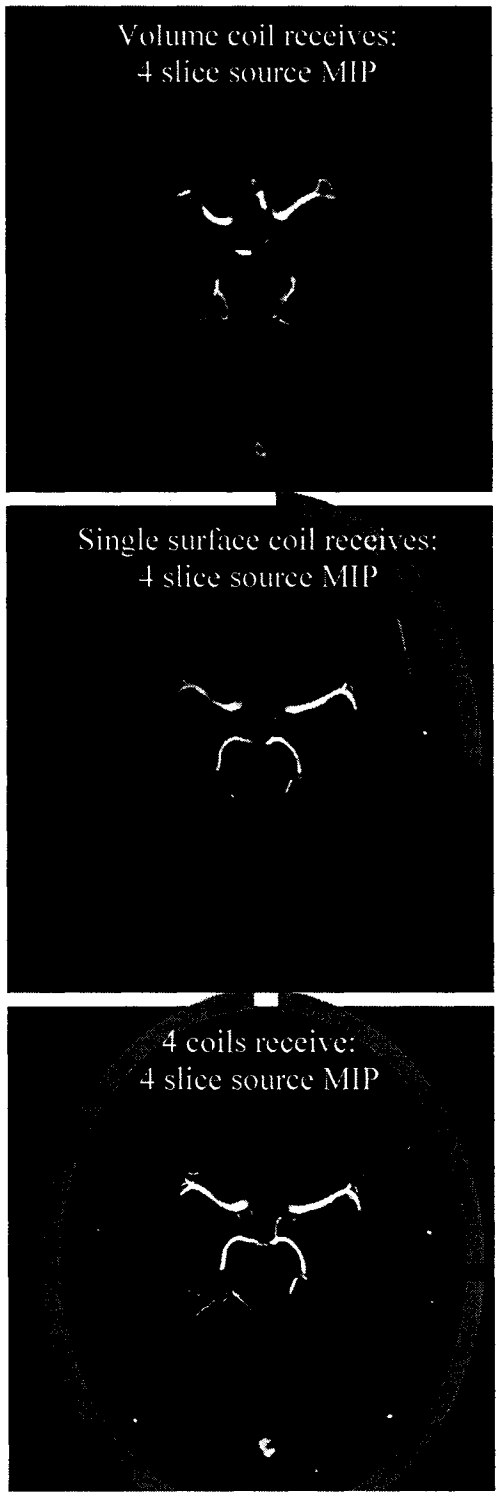

Figure 4.9 4.7 T MIP of each of the three cases examined previously. Here, each MIP consists of only 4 slices.

MIP in-flow angiograms of the circle-of-Willis were acquired as shown in the figures, consisting of many 1 mm thick slices from the imaging volume, combined into one projection. The images show good background tissue suppression and good blood to background contrast. Of note is the fact that the smaller distal arteries at the sides of the head are clearly visible, even with the reduced flip angles in this region due to high field B_1 inhomogeneity. It is also important to notice that the background has been suppressed with a high degree of uniformity.

Fresh blood travels into the slab and outwards from the proximal middle cerebral arteries, eventually flowing through more distal vessels at the sides of the head. Blood travels through proximal vessels at a higher velocity than distal vessels, and has to travel further to fill distal vessels. Distal vessels experience reduced blood in-flow replenishment, and thus reduced signal compared to proximal vessels.

Proximal vessels experience a higher flip angle than distal vessels due to high field destructive interference[21], again leading to reduced signal in distal vessels. Use of a surface coil phased array[18] greatly increases sensitivity near the sides of the head and counteracts the reduced signal intensity of the small distal arteries. Use of this array coil provides compensation for the previously mentioned effects, and results in higher blood-to-background CNR compared to when the volume coil is receiving, consistent across the entire brain (Table 4.1).

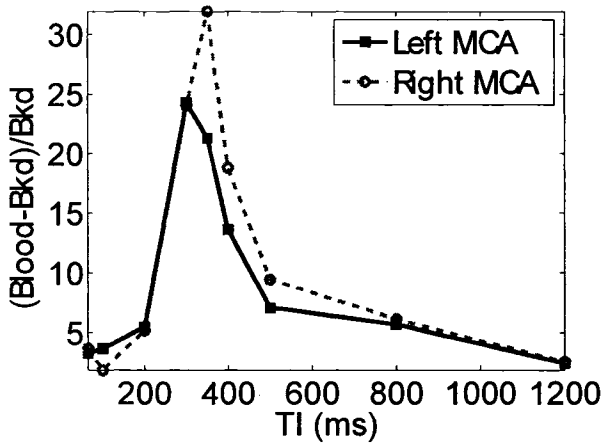

Figure 4.10 4.7 T blood contrast measured with gated 2D MP-MRA in a volunteer's middle cerebral arteries as a function of inversion time. The range of maximum blood contrast occurs when TI is close to optimal for background suppression, approximately 350 ms in this case.

Table 4.1 Example 3D MP-MRA blood - background contrast to noise (CNR) values measured at a main, proximal middle cerebral artery (MCA) and a distal vessel.

	Head Coil Transmits, 4 Array Coils Receive	**Head Coil Transmits and Receives**
Main MCA CNR	108	72
Distal MCA CNR	87	29

Especially evident is the fact that the background is remarkably dark for the MIP images, and does not require specialized software to dissect blood vessels out from the background, as is commonplace at lower field strengths. In addition, it can be seen that excellent venous suppression has been achieved with a second pulse immediately prior to

the inversion. The sagittal sinus is still visible at the posterior of the head, but this does not overlap any of the arteries of interest.

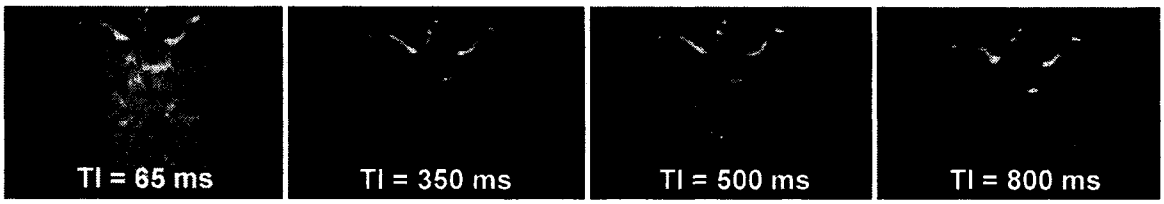

Figure 4.11 Effect of varying TI on gated 2D MP-MRA at 4.7T, 5mm slices. Optimal TI for background suppression for this volunteer's heart rate was calculated with simulations to be approximately 350 ms. Notice the high degree of background suppression for the choice of optimal TI. Each image is windowed and levelled identically for comparison, and the same receiver gain was used throughout.

4.4 Conclusion

An MP-MRA sequence was designed and tested by the author from the ground up, using a simple gradient echo pulse sequence as the basis. The sequence was used to perform in-flow angiography of the intracranial arteries on a 4.7 T Varian system. Pulse sequence parameter values and timing were carefully selected according to simulations with respect to the subject's heartrate. Gating to the human heartbeat was implemented and tested to maximize blood-to-background contrast.

At 4.7T, through the use of IR with appropriate TI times, one can improve both the homogeneity of images, and the blood-to-background contrast of in-flow angiograms. Only a certain range of TI's allow for good blood-to-background contrast at high field strength with this technique. The increased T_1 times at high field can be exploited by allowing more time for in-flow after inversion, while still providing for background suppression. In addition, the use of IR can produce images with flatter RF profiles across

the brain, mitigating the destructive interference effect. Inflow time is limited, however, and SAR is increased due to the presence of high power inversion pulses.

Alternatively, the IR pulse may be eliminated to produce vastly increased inflow times, while still maintaining adequate image contrast owing to the substantially longer T_1 times at 4.7T. The effect of increased time after each acquisition segment is to allow for more inflow of fresh blood into the imaging volume, at the expense of increasing the background signal. Magnetization recovery is slow enough, however, that the background suppression is sufficient. With centric phase-encode ordering, though the drop in magnetization during acquisition views later in each segment may result in some blurring, image contrast is well preserved. The increased SNR available at 4.7T further increases the achievable CNR.

Smaller, distal intracranial arteries at the sides of the head are visible at high field using a single transmit and receive volume coil. However, use of an array coil tailored to fit closely to the human head provides superior blood-to-background CNR for these vessels.

4.5 Bibliography

[1] D Li, M Haacke, JP Mugler III, S Berr, JR Brookeman, MC Hutton, Three-dimensional Time-of-Flight Magnetic Resonance Angiography Using Selective Inversion RAGE with Fat Saturation and ECG Triggering: Application to Renal Arteries. MRM 31:414-422 (1994).

[2] DB Richardson, AEH Bampton, SJ Riederer, JR MacFall, Magnetization-prepared MR Angiography with Fat Suppression and Venous Saturation. JMRI 2:653-664 (1992).

[3] MK Atalay, SB Reeder, EA Zerhouni, JR Forder, Blood Oxygenation Dependence of T_1 and T_2 in the Isolated, Perfused Rabbit Heart at 4.7 T. MRM 34:623-627 (1995).

[4] AH Wilman, SJ Riederer, RC Grimm, PJ Rossman, Y Wang, BF King, RL Ehman, Multiple Breathhold 3D Time-of-Flight MR Angiography of the Renal Arteries. MRM 35:426-434 (1996).

[5] AE Holsinger, SJ Riederer, The Importance of Phase-Encoding Order in Ultra-Short TR Snapshot MR Imaging. MRM 16:481-488 (1990).

[6] AH Wilman, SJ Riederer, Improved Centric Phase Encoding Orders for Three-Dimensional Magnetization-Prepared MR Angiography. MRM 36:384-392 (1996).

[7] AH Wilman, SJ Riederer. Performance of an Elliptical Centric View Order for Signal Enhancement and Motion Artifact Suppression in Breath-hold Three-Dimensional Gradient Echo Imaging. MRM38:793-802 (1997).

[8] DG Nishimura, Principles of Magnetic Resonance Imaging, Chapter 11. Department of Electrical Engineering, Stanford University, (1996).

[9] O Al-Kwifi, DJ Emery, AH Wilman, Vessel Contrast at Three Tesla in Time-of-Flight Magnetic Resonance Angiography of the Intracranial and Carotid Arteries. Magnetic Resonance Imaging 20:181-187 (2002).

[10] DI Hoult, RE Richards. The Signal-to-Noise Ratio of the Nuclear Magnetic Resonance Experiment. JMR 24, 71-85 (1976).

[11] AH Wilman, J Huston III, SJ Riederer, Three-dimensional Magnetization-Prepared Time-of-Flight MR Angiography of the Carotid and Vertebral Arteries. MRM 37:252-259 (1997).

[12] EH Hsu, SB Reeder, JR MacFall, Single-Shot, Variable Flip-Angle Slice-Selective Excitation with Four Gradient-Modulated Adiabatic Half-Passage Segments. MRM 40:334-340 (1998).

[13] RA de Graaf, K Nicolay, M Garwood, Single-Shot, B_1-Insensitive Slice Selection with a Gradient-Modulated Adiabatic Pulse, BISS-8. MRM 35:652-657 (1996).

[14] JG Sled, GB Pike, Standing-Wave and RF Penetration Artifacts Caused by Elliptic Geometry: An Electrodynamic Analysis of MRI. IEEE Transactions on Medical Imaging, Vol. 17, No. 4, August (1997).

[15] JW Monroe, P Schmalbrock, DG Spigos, Phased Array Coils for Upper Extremity MRA. MRM 33:224-229 (1995).

[16] CE Hayes, CM Mathis, C Yuan, Surface Coil Phased Arrays for High-Resolution Imaging of the Carotid Arteries. JMRI Jan./Feb. 109-112 (1996).

[17] HG Bogren, MH Buonocore, Blood Flow Measurements in the Aorta and Major Arteries with MR Velocity Mapping. JMRI 4,119-130 (1994).

[18] PulseTeq, England

[19] AP Crawley, ML Wood, RM Henkelman, Elimination of Transverse Coherences in FLASH MRI. MRM 8:248-260 (1988).

[20] FH Epstein, JP Mugler III, JR Brookeman, Spoiling of Transverse Magnetization in Gradient-Echo Imaging (GRE) During the Approach to Steady State. MRM 35:237-245 (1996).

[21] TS Ibrahim, R Lee, AM Abduljalil, BA Baertlein, PM Robitaille, Dielectric Resonances and B_1 Field Inhomogeneity in UHF MRI: Computational Analysis and Experimental Findings. Magnetic Resonance Imaging 19 (2), 219-226 (2001).

5 General Discussion and Conclusions

Magnetization-prepared 3-D gradient echo pulse sequences for T_1-weighted structural imaging and angiography have been created on a 4.7 T Varian system, including several variations of MP-RAGE and MDEFT. The author, starting with a rudimentary gradient-echo FLASH sequence, designed and fully tested the pulse sequences. In this work a variety of techniques that can be used to compensate for high field destructive interferences while producing high-resolution images at 4.7 T have been investigated. A surface coil phased array was constructed by the author for imaging of the head and neck. In-vivo tests and results were performed with both the constructed, and commercial, receive-only coils.

For structural imaging, optimization of the uniformity of images at 4.7 T, while still maintaining reasonable contrast between white matter and grey matter, was explored. Some attention was given to the proper choice of parameters, such as excitation flip angle, as well as the use of adiabatic versus hard or soft pulses. The effects on contrast and profile uniformity of different combinations of preparation pulses were examined.

Magnetization-prepared angiography at 4.7 T using a gradient echo pulse sequence was performed. Not only were the intracranial arteries clearly defined with high SNR, but also in particular it was found that distal arteries were visible despite high field destructive interference. Using a phased array coil further improved results. Also, a novel technique involving the removal of the magnetization preparation was developed and shown to produce similar blood-to-background contrast as the magnetization-prepared technique.

The magnetization-prepared imaging sequences could be applied in a variety of clinical situations. These types of sequences are excellent for imaging brain haemorrhages associated with strokes. Brain tumours could also be diagnosed and investigated by taking advantage of the T_1-weighted contrast capabilities of these sequences. Because of the precise, high-resolution nature of these sequences (as opposed to, EPI sequences), accurate morphological measurements can be made, with applications in psychology. The

basal ganglia are located in the centre of the brain and consist of grey matter bundles intermixed with white matter. This area is a region of high B_1 transmit and receive sensitivity at 4.7 T and can be imaged with high signal intensity using magnetization-prepared sequences. Structural changes in the basal ganglia are linked to Parkinson's disease.

Applications of the MRA pulse sequences that were developed include imaging of the intracranial circulation and the carotid arteries of the neck. The images could be used for diagnosis of atherosclerosis by examination of arterial stenoses. In addition, arteries elsewhere in the body could be imaged with the same sequences, if appropriate transmission and receive coil hardware is available, such as renal imaging with a body coil.

In summary, the high field transmit and receive inhomogeneities, though displayed quite strongly at 4.7T, are not so strong as to prevent the implementation of magnetization-prepared imaging. It has been shown that in-flow angiography and magnetization-prepared gradient echo imaging are viable techniques at 4.7T, and receive-only array coil should be used for best results.

5.1 Future Directions

All of the techniques that have been investigated can be applied at other field strengths. Sequence optimization and design would have to be individualized, given the differing characteristics at each magnetic field strength, such as T_1 recovery times and extent of B_1 inhomogeneity.

Advanced, specialized high field coils have been constructed by other groups, which greatly reduce B_1 transmit field inhomogeneity[1]. The inherent uniformity of such coils could be used in combination with the sequence design described in this thesis. With the

B_1 uniformity requirement relaxed, it may be possible to improve contrast and signal even further at 4.7 T. However, such specialized coils have mainly been examined thus far in a transceiver configuration, that is, with the volume coil both transmitting and receiving. It may be useful to attempt to use these coils for transmit only, in combination with the receive-only coils described in Chapter 2. Furthermore, it may be possible to reduce high field destructive interference effects which shift and distort the receive sensitivity profiles of the receive-only coils, using the centimetre-band RF techniques as described by Vaughan, et al[1].

It is possible that a better result can be obtained by changing the flip angles of the excitation pulses during the magnetization evolution that occurs during acquisition of an echo train in the pulse sequences. This could be investigated as a means of further increasing the contrast, uniformity, and sharpness of images.

Improvements to MP-RAGE could be implemented[2], which offer shorter overall sequence times while maintaining a similar resolution and SNR. Parallel imaging such as SENSE[3] could be used in conjunction with the phased array in order to further accelerate imaging, or alternatively, increase resolution. Also, besides MP-RAGE and MDEFT, the magnetization preparation techniques that were explored can be applied to other types of pulse sequences. In particular, the T_1-weighted 3D gradient echo acquisition can be swapped out for another sequence type such as steady-state free precession, while keeping the magnetization preparation stage intact. If this were done, the preparation pulses would have to be specialized to optimize the contrast and uniformity given the contrast mechanism of a different pulse sequence.

5.2 Bibliography

[1] PF Van de Moortele, C Akgun, G Adriany, S Moeller, J Ritter, CM Collins, MB Smith, JT Vaughan, K Ugurbil, B_1 Destructive Interferences and Spatial Phase Patterns at 7 T with a Head Transceiver Array Coil. MRM 54:1503-1518 (2005).

[2] C Lin, MA Bernstein, J Huston III, Integration of Scan Time Reduction Techniques with Rearranged Elliptical Centric k-Space Acquisition for 3DTOF MRA at 3.0T, p. 809, Proceedings of the ISMRM 14 (2006).

[3] M Weiger, KP Pruessmann, C Leussler, P Roschmann, P Boesiger, Specific Coil Design for SENSE: A Six-Element Cardiac Array. MRM 45 (3) 495-504 (2001).

Appendix A

A.1 Derivations and Component Values for Chapter 2

A.1.1 Derivation of Equation 2.6

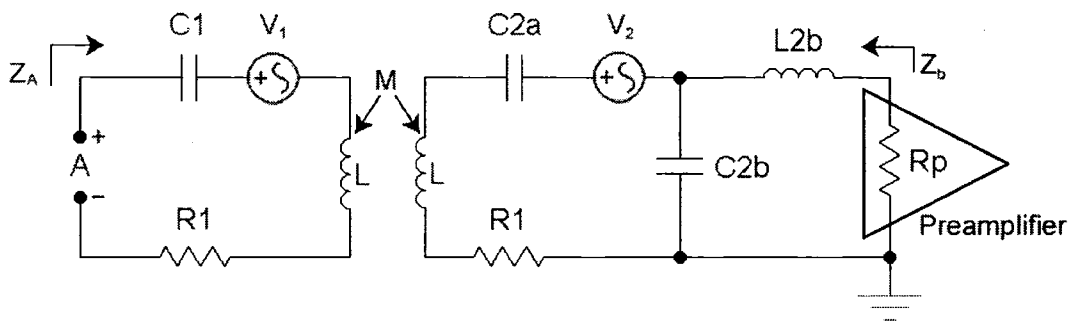

Figure 2.7 Transformer model of two coils in a phased array, which illustrates how tuning and matching a phased array and inter-coil coupling can be examined with conventional lumped-element circuit analysis techniques. Coil 1 is identical to coil 2 and also has a capacitor, C_{1b}, inductor, L_{1b}, and preamplifier (not shown). Coil 1 on the left couples with coil 2 on the right, and they may share a mutual inductance between them, M. The induced MR voltage is represented in each coil as V_1 and V_2. R_p is the preamplifier input impedance as seen by each coil. Coaxial cables may connect each coil to its corresponding preamp.

If the coils are tuned to resonate at the 4.7 T Larmor frequency then $X_L - X_{C1} = 0$ and $X_L - (X_{C2a} + X_{C2b}) = 0$ thus the total impedance seen looking at the coils from the preamplifier input impedance is:

$$Z_b = \frac{(jX_{C2b} + R_1)(-jX_{C2b})}{R_1 + jX_{C2b} - jX_{C2b}} + jX_{L2b}$$

$$= \frac{X_{C2b}{}^2 - jR_1X_{C2b}}{R_1} + jX_{L2b}$$

$$= \frac{X_{C2b}{}^2}{R_1} + j(X_{L2b} - X_{C2b})$$

A.1.2 Derivation of Equation 2.7

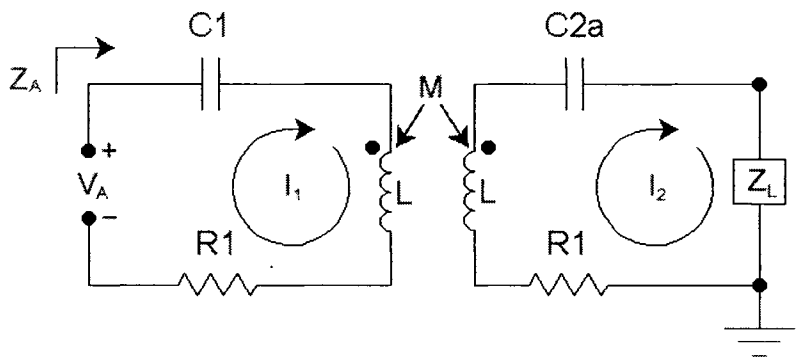

Figure 2.8 Transformer model of two coils in a phased array, with induced MR voltages removed for calculation of the input impedance at terminal A, Z_A. This terminal has an associated open circuit voltage V_A. Coil 2 drives a load Z_L, which consists of L_{2b}, C_{2b}, and the preamp input impedance R_p. Coil 1 is identical to coil 2 and also drives a load Z_L (not shown). Coil 1 on the left couples with coil 2 on the right, and they share a mutual inductance between them, M, which needs to be significantly reduced in order to improve coil isolation.

If $X_{L2b} = X_{C2b} = X_2$, then with reference to Figure 2.7:

$$Z_L = -jX_2 \,//\, (jX_2 + R_p)$$

$$= \frac{-jX_2(jX_2 + R_p)}{-jX_2 + jX_2 + R_p}$$

$$= \frac{X_2^2 - jX_2R_p}{R_p} \approx \frac{X_2^2}{R_p}$$

where the fact that $R_p << X_2$ has been noted for the approximation.

Using mesh analysis with reference to Figure 2.8, realizing at resonance $X_L - X_{C1} = 0$ and $X_L - (X_{C2a} + X_{C2b}) = 0$:

$$V_A = I_1R_1 - j\omega MI_2$$
$$0 = I_2R_1 + j\omega MI_1 + I_2Z_L$$

Solving for I_2 using the previous equation:

$$I_2 = \frac{-j\omega MI_1}{R_1 + Z_L}$$

Thus:

$$V_A = I_1R_1 - j\omega M\frac{-j\omega MI_1}{R_1 + Z_L} = \left(R_1 + \frac{\omega^2M^2}{R_1 + Z_L}\right)I_1$$
$$Z_A = \frac{V_A}{I_1} = R_1 + \frac{\omega^2k^2L^2}{R_1 + Z_L} = R_1 + \frac{\omega^2k^2L^2}{R_1 + \frac{X_2^2}{R_p}}$$

A.1.3 Component Values for the 4.7 T Four Coil Phased Array

The wavelength of electrical signals at the 4.7 T ^{1}H Larmor frequency in coaxial cable is:

$$\lambda = v/f = 0.66 \cdot (3 \times 10^8 \text{ m/s})/(200.4 \text{ MHz}) \approx 0.99 \text{ m}$$

where v is the velocity, f is the Larmor frequency, and 0.66 is the velocity propagation constant of the RG-58/U cable. Cables should be cut so that they appear to be open circuits on the network analyzer; that is, their reactance is eliminated. Thus, cables were cut to be of length $n\lambda/2$, where n is a positive integer.

Coils were constructed using 1 cm wide copper tape. Coil diameter was approximately 10 cm, with an inductance of 76.5 nH before being cut for insertion of the distributed capacitance. Coil overlap was approximately 3 cm for optimal reduction of mutual coupling between pairs.

JANTX 1N6638U *nonmagnetic* diodes (Uni-Semi) were used. Nonmagnetic ceramic round capacitors were used. Inductors were created by coiling metal wire. Inductor values were not measured individually but were tuned empirically using the network analyzer to resonate with their associated capacitors, in parallel circuits.

Table A.1 Phased array coil capacitor values used. The '+' symbol is used to indicate series capacitors, while the '-' symbol is used to indicate the range of capacitance for variable capacitors. Each value given is in units of pF. Note that each coil uses slightly different values due to the limited component supply available. Also, capacitor C_{2b} was distributed into two separate capacitances separated by copper tape, C_{2b1} and C_{2b2}. The variable capacitor in parallel with C_{2a} was placed in a tune box that was separated from the coil by a coaxial cable. This variable capacitor is labelled $Ct_{variable}$ in the table. Also in the tune box were Cm and its associated variable capacitor $Cm_{variable}$.

Coil #	C_{2b1}	C3	C_{2b2}	C_{2a}	$Ct_{variable}$	$Cm_{variable}$	Cm
1	15+15	15+15+15	15+15	68+12	3-13	6-26	12
2	12+18	15+15+12	12+18	68+12	3-13	6-26	12
3	12+22	22+18+22	12+22	68+12	3-13	6-26	68
4	12+22	22+18+22	12+22	68+12	3-13	6-26	68